Variable-Structure Cable-Driven Parallel Robots

by

Mitchell Rushton

A thesis
presented to the University of Waterloo
in fulfillment of the
thesis requirement for the degree of
Doctor of Philosophy
in
Mechanical and Mechatronics Engineering

Waterloo, Ontario, Canada, 2022

Examining Committee Membership

The following served on the Examining Committee for this thesis. The decision of the Examining Committee is by majority vote.

External Examiner	PHILIPPE CARDOU Professor
Supervisor	AMIR KHAJEPOUR Professor
Internal Member	JAMES TUNG Associate Professor
Internal Member	ARASH ARAMI Assistant Professor
Internal-external Member	JENNIFER BOGER Adjunct Assistant Professor

Author's Declaration

I hereby declare that I am the sole author of this thesis. This is a true copy of the thesis, including any required final revisions, as accepted by my examiners. I understand that my thesis may be made electronically available to the public.

Abstract

Cable-driven parallel robots (CDPR) are a special class of robotic manipulators consisting of a rigid end effector suspended, constrained, and actuated by a number of length-varying cables. Since cable mass is typically negligible, it allows CDPRs to be built with extremely low-inertia, enabling high-accelerations and the ability to span distances that would otherwise be impossible using rigid structures. Where CDPRs suffer is their inability to perform in cluttered installation spaces due to the need to avoid collisions between cables and the environment. This thesis proposes a design alternative defined as 'variable-structure CDPRs' (VSCR) to address the inherent limitations CDPRs have regarding their limited usable workspaces in cluttered environments. What makes VSCRs unique is their ability to instantaneously alter their dynamic structure through collisions between cables and objects fixed in the environment. It is shown that, unlike traditional CDPRs, VSCRs are able to produce non-convex reachable workspaces: a property that is especially useful for circumventing obstacles and has implications for a wide range of applications such as rehabilitation, agriculture, and warehousing. An extended cable model for representing collidable cables is developed along with a corresponding inverse kinematics method as a foundation for initiating the study of VSCRs. Next, an atlas-based approach for representing VSCR configuration spaces is introduced, along with a method for its computation. The proposed representation, referred to as the 'structure atlas,' is shown to be a powerful tool for performing VSCR workspace analysis and inverse kinematics. Finally, an experimental testbed is constructed and used for conducting several experimental studies to validate the previously mentioned theoretical contributions and observe the real-world capabilities of VSCRs. Mathematically and experimentally, it is shown that VSCRs dramatically improve the reachability and accessible workspaces CDPRs can achieve in cluttered or irregular environments.

Acknowledgments

I would like to acknowledge Dr. Hamed Jamshidifar for his assistance in helping to move the experimental setup from my apartment to the university and Lab technicians Jeff Graansma and Adrian Neill for providing me with some of the wire I needed and helping me cut it to the correct lengths.

I would like to thank the Natural Sciences and Engineering Research Council of Canada (NSERC) for their financial support in completing this research, my parents and family for their love and support, Aidi and Lana for the joy they have brought to my life, and my Examining Committee members for their time and effort in reviewing this material.

Above all, I would like to thank my supervisor, Professor Amir Khajepour. I am truly fortunate to have met him and very grateful for the opportunities he has given me over the years. Without his thoughtful guidance and endless support, this thesis would not exist.

Table of Contents

List of Figures

List of Tables

List of Algorithms

List of Abbreviations

C-space configuration space. 24, 59

CCW counter clockwise. 66

CDPR cable-driven parallel robot. 1

CRA cable-reachable area. 62

CST cable-state tree. 40

CW clockwise. 66

DOF degrees of freedom. 8

EE end effector. 87

NAE nearest active edge. 67

PM point mass. 10, 29

PNE previous nearest edge. 68

PRA platform-reachable area. 72

SA structure atlas. 69

SRA structure-reachable area. 62

VSCR variable-structure cable-driven parallel robot. 5

WCW wrench-closure workspace. 13

WFW wrench-feasible workspace. 14

Nomenclature

General Formatting

a	scalar
$\boldsymbol{a}$	vector
$\boldsymbol{A}$	matrix
A	set
$\overline{\boldsymbol{ab}}$	line segment with end points $\boldsymbol{a}$ and $\boldsymbol{b}$
$\widehat{\boldsymbol{abc}}$	arc with end points $\boldsymbol{a}$ and $\boldsymbol{c}$ and center point $\boldsymbol{b}$
iff	if and only if

Special Sets

$\emptyset$	empty set
$\mathbb{R}$	set of real numbers
S^n	n-dimensional sphere
T^n	n-dimensional torus
$\mathcal{I}$	installation space
$\mathcal{T}$	task space
$\mathcal{C}$	configuration space
$\boldsymbol{q}$	used for denoting a point in $\mathcal{C}$

Operators

$\|\cdot\|$	Euclidean norm
$\cap$	set interception
$\cup$	set union
$\setminus$	set minus
$\oplus$	Minkowski sum

CDPR Modelling

$\boldsymbol{a}_i$	cable fixed-frame anchor point; defined in the ground frame
$\boldsymbol{a}_{ij}$	winch facing endpoint for the jth segment along cable i
$\boldsymbol{b}_i$	cable platform-fixed anchor point, defined in the ground frame
$\boldsymbol{b}_{ij}$	platform facing endpoint for the jth segment along cable i
$\hat{\boldsymbol{c}}_i$	unit vector pointing from the platform toward the fixed frame
$\boldsymbol{g}$	gravitational acceleration vector
k	number of collidable objects
l_i	total length of cable i
l_{ij}	length of the jth line segment along cable i
m	mobile platform degrees of freedom
m_i	number of segments that make up cable i
n	number of cables
$\boldsymbol{p}$	end effector position
$\mathcal{Q}$	chart domain
$\boldsymbol{r}_i$	cable platform-fixed anchor point, defined in the body frame
$\boldsymbol{R}$	rotation matrix used for defining the mobile platform orientation

$\boldsymbol{w}_i$	wrench applied to mobile by form by the ith cable
$\boldsymbol{w}_{\text{ext}}$	general term used to represented any externally applied wrench
$\boldsymbol{W}$	CDPR Wrench Matrix
β	angle at point of entry to a collided object
θ	end effector orientation angle
ν_{ij}	wrapping segment length for the jth segment along cable i
τ_i	tension force magnitude for the ith cable
$\boldsymbol{\tau}$	vector of cable tensions
ϕ	denotes a cable wrap angle

Chapter 1

Introduction

1.1 Motivation

Cable-driven parallel robots (CDPRs), also referred to as 'cable robots' or 'wire-driven parallel robots', are a relatively new class of robotic manipulators. In contrast to classical manipulator designs composed entirely of rigid links, CDPRs consist of a rigid end effector suspended and constrained by a number of actuated cables (see Fig. 1.1). The most common mode of actuation for CDPRs involves the use of length-varying cables driven by winches; however, various alternative actuation strategies have been investigated, such as varying the attachment-point locations for a set of fixed-length cables, Figs. 1.1c and 1.1e.

The motivation behind the research and development of CDPRs is driven by the unique properties of cables and the advantages they provide over rigid links, the first being that cables are extremely light for a given load capacity due to their exceptional tensile-strength-to-weight ratio. This results in CDPRs having very low-inertia with cables generally having negligible weight in comparison with the end effector and payload mass. The significant reduction in robot inertia over their rigid counterparts enables CDPRs to generate high-accelerations, span much larger distances, and require smaller actua-

(a) SkyCam [1]

(b) FAST [2]

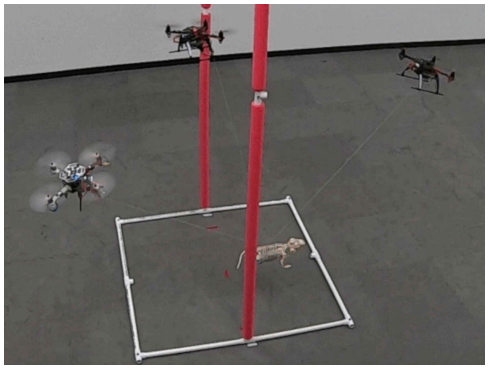

(c) UAV-based CDPR [3]

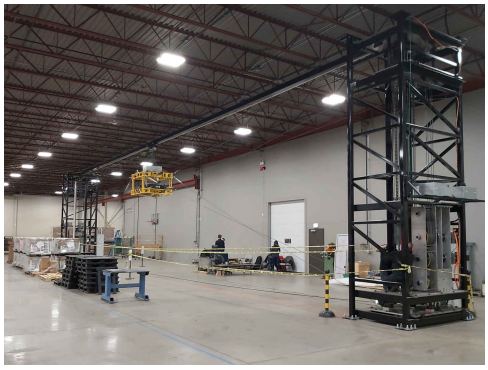

(d) Warehousing CDPR

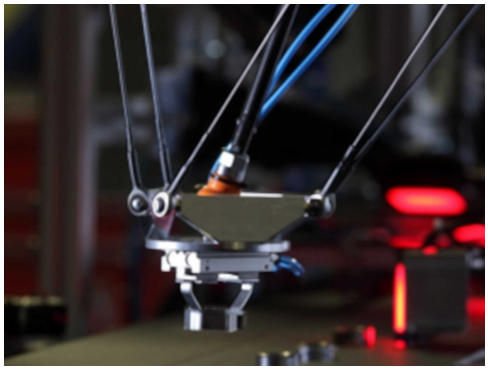

(e) DeltaBot Cable [4]

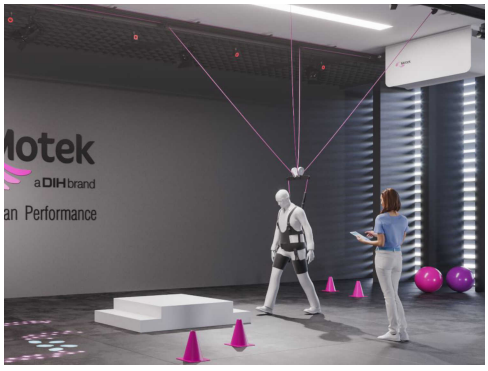

(f) RYSEN [5]

Figure 1.1: Notable examples of existing CDPRs.

tors. A second unique property of cables is that despite their exceptional tensile strength, cables remain highly flexible in non-axial directions, possessing the ability to deform and wrap around contacted surfaces, allowing for enhanced safety and reducing the likelihood of damage or injury in the event of collisions.

Over the past two decades, our knowledge and understanding of CDPRs has grown significantly. Through the use of CDPRs, large-scale robotic systems have become a reality, having been deployed in a number of applications. Cable-suspended camera systems, such as those developed by 'SkyCam' (Fig. 1.1a) and 'Spidercam', are now widely used in stadiums for filming sporting events and concerts. The receiving antenna for the 'Five-hundred-meter Aperture Spherical radio Telescope' (FAST) in Guizhou, China, which became fully operational in January 2020, is driven by a six-cable CDPR (shown in Fig. 1.1b) and easily the largest robotic system ever built [2]. A recent prototype built at the University of Waterloo in collaboration with industrial partner Dematic demonstrates the potential CDPRs have for applications such as high-speed automated warehousing: the 12-cable planar CDPR (shown in Fig. 1.1d) has a 25×5 m workspace and is capable of travelling at speeds in excess of 5 m/s. On a smaller scale, CDPRs have found their way into industrial automation with a cable-driven variation on the classic delta-robot design having been developed by AEMK systems (Fig. 1.1e).

Not only are cables extremely low-inertia, they are also compact, inexpensive, and minimally intrusive. Together with the safety features that cables possess, these properties make CDPRs particularly well suited for medical applications, such as rehabilitation, where robotic manipulators are often directly coupled to patient limbs. The first cable-driven rehabilitation robot to be made commercially available is the 'RYSEN' (Fig. 1.1f), developed by Motek. The RYSEN is a cable-driven bodyweight support system that enables both vertical and horizontal plane mobility for patients over a large area, granting an unprecedented level of freedom of mobility for rehabilita-

tion patients recovering from a stroke or spinal cord injury [6].

The many advantages of cables do not come without their own set of challenges and drawbacks, most of which stem from a third unique property of cables: they can only transmit force while under tension. This uni-directional force constraint leads CDPRs to suffer from an increased susceptibility to end effector vibrations and often requires redundant actuation for the end effector to be fully constrained [7,8]. These challenges complicate things from a controls perspective; however, strategies have been found to mitigate most of these issues, such as optimized cable layout patterns designed to maximize manipulator stiffness [9, 10] and active vibration damping using the cables or additional actuators mounted on the mobile platform [11–13]. Perhaps the most limiting issue for CDPRs is the relatively small workspaces they can achieve for a given installation space and the potential for collisions to occur between cables and the surrounding environment [14,15]. Additionally, since the span of a cable is always radially convex [16], it is impossible for fully-constrained CDPRs to cover non-convex installation spaces.

The potential for cable collisions to occur is a well-known issue with CDPRs. Not surprisingly, it is also a topic that has received a lot of research interest, being studied primarily from the perspectives of collision detection and avoidance. Many papers have been published on topics such as determining the collision-free workspace [14, 17, 18] and the planning of collision-free trajectories [19,20]. While important, there is a limit to what can be achieved with such strategies, and they are helpless to overcome fundamental limitations, such as the restriction to convex installation spaces.

Despite the ability of cables to wrap around collided surfaces being one of the most unique and interesting properties of cables, it is a property that has not been well studied. Very few publications exist that consider the possibility of allowing cable collisions to occur, and no systematic treatment has been given thus far.

1.2 Objective and Contribution

The objective of this thesis is to answer, in part, the question of what happens if collisions are permitted to occur between the cables of a CDPR and fixed objects in the surrounding environment. This objective has been motivated by the belief that the additional design freedom afforded by allowing collisions may help to address some of the current limitations of CDPRs. In following this objective, this thesis makes the following contributions:

- Introduction of a classification system for CDPRs based on the number and type of generalized coordinates required for representing the mechanism's configuration.
- Identification of two previously unidentified classes of CDPRs, one of which is defined as 'variable-structure cable-driven parallel robots' (VSCR) and shown to be able to cover non-convex installation spaces through the use of collisions between cables and objects fixed in the environment.
- An extended cable model that considers collisions between cables and rigid objects fixed in the environment. Included with this model is an online method for cable-state tracking and solving the inverse kinematics problem for collidable cables.
- An atlas-based approach to representing VSCR configuration spaces and identifying all reachable structures. This representation is denoted as the 'structure atlas' and is shown to be a powerful tool for analyzing VSCRs with specific applications to workspace analysis and inverse kinematics being demonstrated.
- Experimental studies, performed on a purpose-built VSCR testbed, serving to validate the theoretical results and observe practical issues that arise when allowing collisions between cables and the environment to occur.

1.3 Outline

Each chapter builds upon the work of the previous; therefore, it is recommended that the chapters be read sequentially. The outline of the remaining chapters is as follows: Chapter 2 provides a review of the relevant background knowledge regarding CDPRs and the current state of the literature; Chapter 3 Introduces a new classification system for CDPRs through which two new classes of CDPRs are identified, one of which is defined as 'variable-structure cable-driven parallel robots' (VSCR) and its study becomes the focus of the remaining chapters; Chapter 4 introduces an extended cable model for handling collisions between cables and the environment; Chapter 5 proposes an atlas-based representation for the VSCR workspace and provides a method for its computation; Chapter 6 presents the results from a number of experimental studies conducted using a purpose-built VSCR testbed to validate the previous chapters' results; Chapter 7 concludes the thesis and provides some recommendations for future research.

Chapter 2

Background Knowledge and Literature Review

This chapter reviews some of the background knowledge required for understanding the remaining chapters and provides context for evaluating the significance of this thesis's overall contribution by reviewing the current state of the CDPR literature. Section 2.1 provides a concise review on the technical details of CDPRs. It is intended primarily to introduce the uninitiated reader to the fundamentals of CDPRs and the standard terminology used throughout the CDPR literature; however, it may also serve as a helpful review and practical reference for current researchers and practitioners. Section 2.2 reviews the state of the current research literature on the impact of collisions on CDPR performance and strategies for overcoming their limitations.

2.1 Cable-Driven Parallel Robots

This section provides a broad overview of CDPRs, focusing on topics relevant to the material presented in the later chapters. For a more comprehensive treatment, the interested reader is referred to "Cable-Driven Parallel Robots: Theory and Application" by Andreas Pott [21].

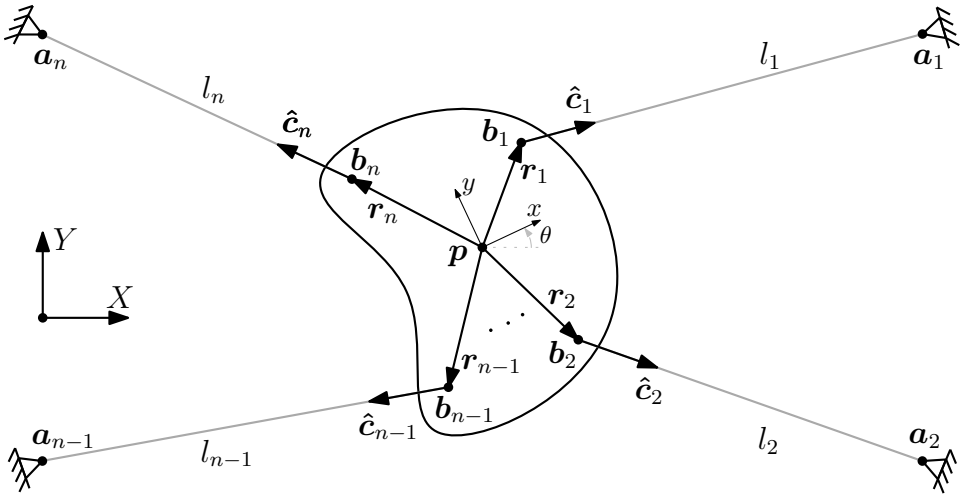

Figure 2.1: General planar CDPR with relevant parameters labeled.

2.1.1 Geometric Model and Wrench Analysis

The standard geometric CDPR model presented here introduces the common notation and answers the following questions: what are the cable lengths required to hold the platform in a given pose, and what is the net effect of cable tensions on the end effector? Cables are assumed to be massless, inelastic, straight-line segments: the so-called 'ideal' cable model. These assumptions are commonly made as they greatly simplify analysis and work well in practice for many applications where the weight and elastic deformation of the cables are often negligible. Alternative cable modelling approaches and when they are appropriate will be discussed in Section 2.1.6.

Mobile-Platform End Effector

Consider the general CDPR shown in Fig. 2.1 consisting of a rigid mobile-platform end effector, n cables, a fixed ground frame $\{X, Y\}$, and a body-fixed frame $\{x, y\}$ attached at the platform centerpoint $\boldsymbol{p}$. The configuration of the platform is defined by its position, $\boldsymbol{p}$, and orientation, θ, for a total of $m = 3$ degrees of freedom (DOF) (for a spatial CDPR, $m = 6$). Each cable

has two end points: one in the fixed frame, and one attached to the mobile platform, labeled $\boldsymbol{a}_i$ and $\boldsymbol{b}_i$ respectively for the ith cable where $i = 1, \cdots, n$. $\boldsymbol{a}_i$ and $\boldsymbol{b}_i$ are commonly referred to as the 'anchor points' of a cable and will be referred to as such throughout this thesis. Both $\boldsymbol{a}_i$ and $\boldsymbol{b}_i$ are defined in the ground frame; the location of the platform-fixed anchor point in the body-fixed frame for the ith cable is referred to as $\boldsymbol{r}_i$. The relationship between $\boldsymbol{r}_i$ and $\boldsymbol{b}_i$ is as follows:

$$\boldsymbol{b}_i = \boldsymbol{p} + \boldsymbol{R}\boldsymbol{r}_i \tag{2.1}$$

where $\boldsymbol{R}$ is the rotation matrix from the body frame to the ground frame. For a planar CDPR, $\boldsymbol{R}$ as a function of θ is defined as

$$\boldsymbol{R} = \begin{bmatrix} \cos\theta & -\sin\theta \\ \sin\theta & \cos\theta \end{bmatrix} \tag{2.2}$$

For a given platform pose $(\boldsymbol{p}, \theta)$, the required cable lengths can be found for each cable as the Euclidean distance between the cable end points $\boldsymbol{a}_i$ and $\boldsymbol{b}_i$:

$$l_i = \|\boldsymbol{a}_i - \boldsymbol{b}_i\| \tag{2.3}$$

where l_i is the length of the ith cable. For determining the net effect of cable tensions on the platform, the unit vector pointing along each cable from the platform towards the fixed frame, $\hat{\boldsymbol{c}}_i$, is first obtained as

$$\hat{\boldsymbol{c}}_i = \frac{\boldsymbol{a}_i - \boldsymbol{b}_i}{l_i} \tag{2.4}$$

The wrench (combined force-moment vector) produced by the ith cable and applied to the mobile platform, denoted as $\boldsymbol{w}_i$, is then found to be

$$\boldsymbol{w}_i = \begin{bmatrix} \hat{\boldsymbol{c}}_i \\ \boldsymbol{R}\boldsymbol{r}_i \times \hat{\boldsymbol{c}}_i \end{bmatrix} \tau_i \tag{2.5}$$

where τ_i represents the cable tension force magnitude. The net effect of cable tensions on the platform is obtained as the summation of the individual wrenches generated by each cable. This can be organized into a matrix representation as follows:

$$\boldsymbol{W}\boldsymbol{\tau} = \sum_{i=1}^{n} \boldsymbol{w}_i \tau_i \tag{2.6}$$

where $\boldsymbol{\tau}$ is a column vector of cable tensions, defined as

$$\boldsymbol{\tau} = \begin{bmatrix} \tau_1 & \tau_2 & \cdots & \tau_n \end{bmatrix}^T \tag{2.7}$$

$\boldsymbol{W}$ is referred to as the 'wrench matrix' (sometimes also referred to as the 'structure matrix' and denoted by $\boldsymbol{A}$) and is defined as follows:

$$\boldsymbol{W} = \begin{bmatrix} \hat{\boldsymbol{c}}_1 & \hat{\boldsymbol{c}}_2 & \cdots & \hat{\boldsymbol{c}}_n \\ \boldsymbol{R}\boldsymbol{r}_1 \times \hat{\boldsymbol{c}}_1 & \boldsymbol{R}\boldsymbol{r}_2 \times \hat{\boldsymbol{c}}_2 & \cdots & \boldsymbol{R}\boldsymbol{r}_n \times \hat{\boldsymbol{c}}_n \end{bmatrix} \tag{2.8}$$

$\boldsymbol{W}$ plays an important and recurring role in the study of CDPRs, as will be seen in later sections.

Point-Mass End Effector

A common CDPR variant involves replacing the mobile platform with a point-mass (PM) end effector, as shown in Fig. 2.2. The overall modelling procedure is the same; however, there are a number of reductions that must be made. Since the end effector exists as a single point, it has no orientation and its configuration is defined completely by the position of point $\boldsymbol{p}$, resulting in $m = 2$ DOF ($m = 3$ in the spatial case). For a PM CDPR, all of the platform-fixed anchor points are located at a common point, $\boldsymbol{p}$, requiring that $\boldsymbol{r}_i = \boldsymbol{0}$ for all cables; thus, Eq. (2.1) simplifies to

$$\boldsymbol{b}_i = \boldsymbol{p} \tag{2.9}$$

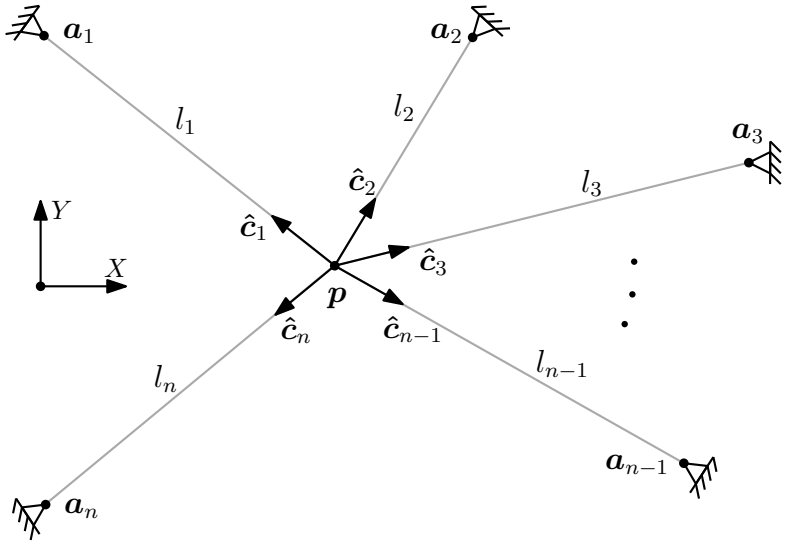

Figure 2.2: General point-mass CDPR with relevant parameters labeled.

Since cable tensions no longer produce any moment, $\boldsymbol{W}$ in Eq. (2.5) reduces to

$$\boldsymbol{W} = \begin{bmatrix} \hat{\boldsymbol{c}}_1 & \hat{\boldsymbol{c}}_2 & \cdots & \hat{\boldsymbol{c}}_n \end{bmatrix} \tag{2.10}$$

2.1.2 Tension Distribution

A problem integral to the study and practical application of CDPRs is how to determine the distribution of cable tensions required to stabilize the mobile platform or balance any arbitrary externally applied wrench. In order for the cable tensions to balance a given externally applied wrench, $\boldsymbol{w}_{\text{ext}}$, the following relation must hold:

$$\boldsymbol{W}\boldsymbol{\tau} = -\boldsymbol{w}_{\text{ext}} \tag{2.11}$$

If $n = m$, the required cable tensions can be solved for directly by taking the inverse of $\boldsymbol{W}$:

$$\boldsymbol{\tau} = \boldsymbol{W}^{-1}\boldsymbol{w}_{ext} \tag{2.12}$$

However, it is often the case that the number of cables exceeds the platform DOF, leading to a rectangular $\boldsymbol{W}$ and an infinite number of possible tension distributions, not all of which will be valid. Due to the uni-directional force constraint on cables, all cable tensions must always be positive. Additionally, there is always a maximum tension in practice that can be produced in a given cable, either due to mechanical limitations or actuator capacity. Generally, the bounds on cable tensions can be stated as:

$$\tau_{\min} \leq \tau_i \leq \tau_{\max} \tag{2.13}$$

where $i = 1, \cdots, n$ and $\tau_{\min} > 0$.

In order to deal with the control redundancy while ensuring a valid solution, many approaches have been proposed. Since Eq. (2.11) and Eq. (2.13) can both be interpreted as linear constraints, a valid solution for $\boldsymbol{\tau}$ can be found using any standard convex optimization technique, such as linear or quadratic programming [22]. This approach has been applied in various ways across various studies with various optimization objectives. [23] uses quadratic programming to find the distribution that minimizes the Euclidean norm of $\boldsymbol{\tau}$ and reduce the required actuator sizes for a given CDPR. In [24], the authors use the infinity norm to minimize the maximum tension in any one cable. In other studies, such as [25, 26], the optimization has been designed to maximize the manipulator stiffness. In [27], the authors provide a closed-form result for the minimum Euclidean norm solution that was further improved upon in [28], making it suitable for real-time application where complex optimization solvers are typically not an option.

2.1.3 Stabilization of the Mobile Platform

In traditional rigid-link-based robotic manipulators, a number of actuated links equal to the end effector DOF is sufficient to stabilize the end effector and maintain a given pose; however, for CDPRs, an additional constrain-

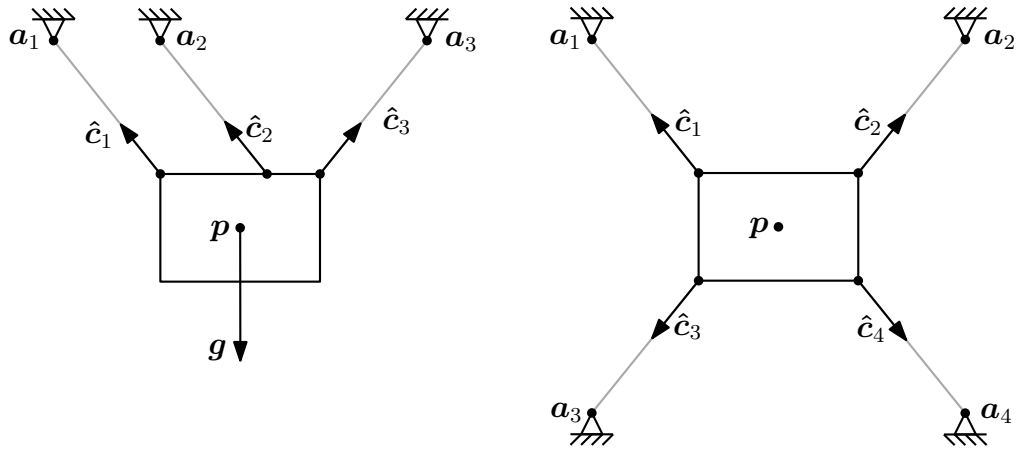

(a) Suspended CDPR (b) Fully-constrained CDPR

Figure 2.3: CDPRs classifications by method of platform stabilization.

ing force is required to maintain positive tensions in the cables: a condition required to ensure platform stability. The required constraining force can either be provided externally (through gravity, for example) or by the inclusion of additional cables, as shown in Fig. 2.3. CDPRs that require an external force in order for positive cable tensions to be maintained are referred to as 'under-constrained' or suspended. If a CDPR is able to maintain positive tensions through the use of internal antagonistic cable tensions alone, it is said to be 'fully constrained'. In general, a minimum of $m + 1$ cables are required in order for a CDPR to be fully constrained [8].

2.1.4 Workspace Analysis

Various CDPR workspace definitions have been proposed that vary based on their inclusion criteria. The first of these is the wrench-closure workspace (WCW), defined as the set of platform poses for which the cables are able to balance any externally applied wrench while maintaining positive tensions [29]. The condition for inclusion in the WCW does not impose any

upper bound on the allowable cable tensions. An alternative definition is the wrench-feasible workspace (WFW), which is defined as the set of poses for which the cables are able to balance all wrenches in a given set of required wrenches while satisfying bounds on the cable tensions [30]. The set of poses for which a state of static equilibrium can be achieved is a special case of the WFW where the required wrench set consists of a single element.

A number of techniques for computing CDPR workspaces have been proposed, the simplest of which is discretizing the installation space into a grid of end effector poses and testing each one for workspace inclusion [30,31]. While discritization is very easy to implement, it is often not very computationally efficient and provides no guarantees on poses that lie in-between adjacent grid points. To resolve some of these issues, more sophisticated numerical methods have been employed, such as interval analysis [32] and ray-based approaches [33]. Geometric approaches have also been developed for determining the WCW for both planar [34] and 6-DOF CDPRs [35]. These methods seek to determine the exact boundaries of the WCW analytically. The drawback of these geometric approaches is that they require a large number of complex equations for representing the workspace boundaries, making them difficult to work with.

2.1.5 Control

For fully-constrained CDPRs, the number of cables exceeds the platform DOF; thus, the platform is kinematically over-constrained. For ideal cables, this leads to a tricky situation where one cannot simply send the required cable lengths to a set of position-controlled winches: any error in the lengths of any cable may lead to cable tension limits being violated and one or more cables becoming slack. Instead, controllers must simultaneously ensure that both desired cable tensions and lengths are maintained. A number of computed torque or feedback linearization based approaches have been applied successfully for this purpose with each winch using force feedback

to ensure cable tension references are followed [36–38]. The drawback of these approaches is that they require an accurate system model in order to be effective. If the cables are highly elastic, good results can be obtained by operating all cables under position control with cable length references adjusted to account for the cable elongation at the desired tensions, based on the known cable stiffness properties [39]. In general, any CDPR can be controlled by operating m cables under position control and the remaining $n - m$ cables under tension control [40].

Cable lengths are usually measured indirectly by encoders mounted to the winch rotors. For ideal cables, this approach is fine; however, it cannot account for any length variations caused by elongation or sagging, leading to position errors that cannot be compensated. As a result, alternative sensing approaches have been proposed, such as lasers pointing along the length of each cable to directly measure cable lengths [41] or vision systems for directly measuring the end-effector pose [42, 43]. Cable tensions are typically measured using load cells, either placed in-line with the cables at the platform-anchor location, or coupled to one of the cable exit pulleys in the fixed frame [44]. In some instances, winch motor torques have been used as a low-cost alternative for estimating cable tensions [45].

2.1.6 Alternative Modelling Approaches

In the standard geometric model, the fixed-frame anchor points are assumed to be fixed; however, for cables exiting from a drive pulley, the true anchor-point location is constantly changing as a function of the cable wrap angle. The deviation is often negligible though it does exist, and as the radius of the exit pulley increases, so does its effect on kinematic errors. To resolve such errors, extended kinematic models that include the effects of exit pulleys on the resulting cable lengths and anchor-point locations have been developed for both inverse and forward kinematics [46, 47].

For CDPRs with highly elastic cables, a common approach is to model

the cables as linear springs with stiffness in the axial direction [39, 48]. In this case, the percentage elongation of a cable, Δl, for a given tension, τ, is found to be

$$\Delta l = \frac{\tau}{EA} \tag{2.14}$$

where E is the Young's modulus and A is the cross-sectional area of the cable. Alternatively stated, the tension within a cable is found as

$$\tau = \frac{EA}{l_0}(l - l_0) \tag{2.15}$$

where l_0 constitutes the cable's unstretched length: the length of the cable when no tension is applied. For synthetic polymer cables, an alternative elastic cable model is presented in [49] which includes hysteresis effects, leading to more accurate results.

When cables are suspended in the presence of gravity, sagging occurs (deformation of a cable due to its own weight). For CDPRs with long, heavy cables, or relatively low tensions, sagging has a major impact on the kinematics and must be considered. In such cases, catenary models have been used which accurately model the profile of a sagging cable [50, 51]. In [52], a simplified parabola based alternative for representing cable sag profiles has also been proposed.

2.2 Literature Review

One of the major current limitations of CDPRs comes from the potential for collisions between cables and obstacles in the environment. Parallel mechanisms, in general, suffer greater limitations in order to avoid collisions than serial manipulators because of their multiple kinematic chains. This limitation is especially problematic for CDPRs due to the uni-directional force constraint on cables: the dependence on antagonistic cable forces for platform stability significantly reduces the potential for areas that can be guaranteed

to be collision-free. The main concerns over collisions include loss of controllability and potential damage to either the cables or the environment. Because collisions are a central concern for CDPRs, researchers have sought ways of detecting and avoiding collisions; however, the result of such efforts at overcoming workspace limitations has been limited.

The use of CDPRs for automated construction is an idea that has been attractive for researchers due to their reconfigurability, relative portability, and achievable scale. In [53], the merits of suspended vs fully-constrained CDPR configurations for building construction are compared. In a suspended configuration, the space below the end effector is unoccupied by cables, which greatly simplifies the problem of collision avoidance at the expense of reduced manipulator stiffness and increased sensitivity to external disturbances, such as wind. Because of the accuracy required for building construction and the presence of environmental disturbances, the need for the end effector to be fully constrained was found to be an important requirement for guaranteeing adequate performance. In [54], the concept of a 'buildable workspace' is introduced for a fully-constrained brick-placing CDPR. As defined in [54], the buildable workspace represents the region where a structure can be built without violating any actuator limitations and without resulting in any collisions between the cables and the structure being built. It was found that the buildable workspace is a small percentage of the entire frame area, with the most significant limitation coming from potential collisions between the lower cables and the structure being built.

In [15] a reconfigurable CDPR is presented for sandblasting and painting large structures. The problem of collisions between cables and the structure to be painted is identified in [55] as an inherent challenge with the use of CDPRs in such applications. The solution proposed in [55] is to use a different cable anchor configuration for each exterior side of the structure, ensuring that each configuration is collision-free. While such an approach does eliminate the problem of collisions, it comes at the cost of requiring

manual intervention to disconnect and reconnect the cables each time a configuration change is required.

Another area where CDPRs have shown promise is in rehabilitation [56, 57]. [58] demonstrates a CDPR design for upper extremity rehabilitation. The design has exciting potential as a low-cost low-inertia alternative to similar designs based on rigid mechanisms; however, because of the constraints imposed by having to avoid collisions between patients and the driving cables, the resulting achievable workspace is small relative to the range of motion of the human arm. In other studies such as [59] and [60], CDPRs have been presented for gait training where motion difficulties persist in one side of the body. In both studies, cables are attached directly to a patient's affected limb to provide assistive forces for completing prescribed repetitive motion exercises; however, one problem that has not been addressed is the potential of collisions between cables and the patients. In certain gait abnormalities (such as "scissor gait"), there is a tendency for the legs to cross over each other [61]. In such cases, collisions between cables and the patient's limbs are an unavoidable concern for patient safety and the controllability of the mechanism.

Several studies have produced methods for detecting cable collisions with both environmental obstacles and other cables [62–65]. In studies such as [14, 17,18], the idea of a 'collision-free workspace' is discussed along with methods for its computation. In [19] and [20], collision avoidance is addressed as a path planing problem: both studies present methods for computing collision-free trajectories for CDPRs in cluttered environments; however, there is a limitation as to what can be achieved with a path planning approach: such methods can only obtain a solution for a collision-free path if one exists. The existence of a solution cannot be guaranteed in general, and depending on the application and robot configuration, this can be a very limiting constraint.

There has been very little discussion in the literature about the possibility of allowing collisions to occur. Two studies have previously considered

permitting collisions to occur between cables: [66, 67]. In [66], an inverse kinematics method is presented for CDPRs where simple collisions between cables are permitted. It was found that by allowing rather than avoiding collisions between cables, the workspace can be expanded. One limitation of the method proposed in [66] however (which is acknowledged) is that it is based on the assumption of frictionless cables. In experimental tests, such an assumption was found to produce errors in the estimated cable lengths and location of the collision point. The presence of friction also poses a concern for wear or damage to the cables during interference. In [67], a collision management strategy was developed for a system of two 6-DOF CDPRs present in the same instalation space. The strategy involved making one of the two colliding cables passive: effectively eliminating the passive cable as an actuator. It was found in [67] that the control and management of cable-cable collisions poses a significant challenge due in part to the risk of large discontinuities in cable tensions at the time of collision. Two studies have considered dynamic interaction between cables and fixed objects in the work environment: [68, 69]. In [68], an alternative CDPR architecture is proposed that allows for cables to collide with two inactive pulleys as a way of extending the dynamic workspace. [69] uses a topological approach to investigate CDPR workspace design and path planning in the presence of polygonal obstacles.

The remainder of this thesis is devoted to exploring the possibilities created by relaxing the constraint that collisions between cables and the environment are something to be universally avoided. This pursuit is guided by the belief that allowing collisions under certain circumstances has the potential to address some of the limitations that CDPRs currently face and extend the set of applications for which CDPRs, with all their advantages, may be considered as a feasible option.

Chapter 3

A Classification of CDPRs

In this chapter, the nature of CDPRs and the potential forms they can take is analyzed in search of alternative design strategies that transcend current limitations. By investigating the possible parametrization classes of a CDPR's configuration space, a classification system for CDPRs is developed and introduced in Section 3.1 through which two new classes of CDPRs are identified. These newly identified forms are found to possess several unique features and design considerations that are discussed in Section 3.2 before concluding the chapter in Section 3.3

3.1 System of Classification

In its most basic form, a CDPR consists of a rigid mobile platform connected to a fixed frame by a number of cables, oriented such that each cable has one end terminating on the mobile platform and one end terminating in the fixed frame. Cables are assumed to be massless, always under tension, and collected/released at one of their two ends. In order for a representation of a CDPR's configuration to be complete, it must be able to reproduce the location of all points on the mobile platform and the full path of each cable. Since the mobile platform always takes the form of a suspended rigid body

Table 3.1: Classes of CDPRs based on generalized coordinates.

Class	Generalized Coordinates
Constant-Structure	Platform pose.
Reconfigurable	Platform pose and any number of additional DOF.
Variable-Structure	Platform pose and any number of discrete state parameters.
Reconfigurable Variable-Structure	Platform pose and both additional DOF and discrete state parameters.

(or point mass), its configuration can always be defined as such. Additionally, since the mobile platform serves as the end effector for the mechanism, the task space for any CDPR is simply the set of all platform configurations. How the configurations of the cables can be specified is less clear and not consistent across different CDPR designs. Based on the number and type (continuous or discrete) of generalized coordinates required for representing the cables (and thus, the complete configuration of the mechanism), the set of all CDPRs can be divided into four distinct classes, as defined in Table 3.1. In the proceeding subsections, the existence of each class is illustrated by example, along with a more detailed definition and discussion of each class's unique features.

3.1.1 Class 1: Constant-Structure

Definition 1 (Constant-Structure CDPR)**.** A CDPR where all cable anchor point locations are constant or known given the platform pose and a set of holonomic constraints, resulting in the entire CDPR being specified by the platform pose.

This class is synonymous with CDPRs and is by far the most commonly

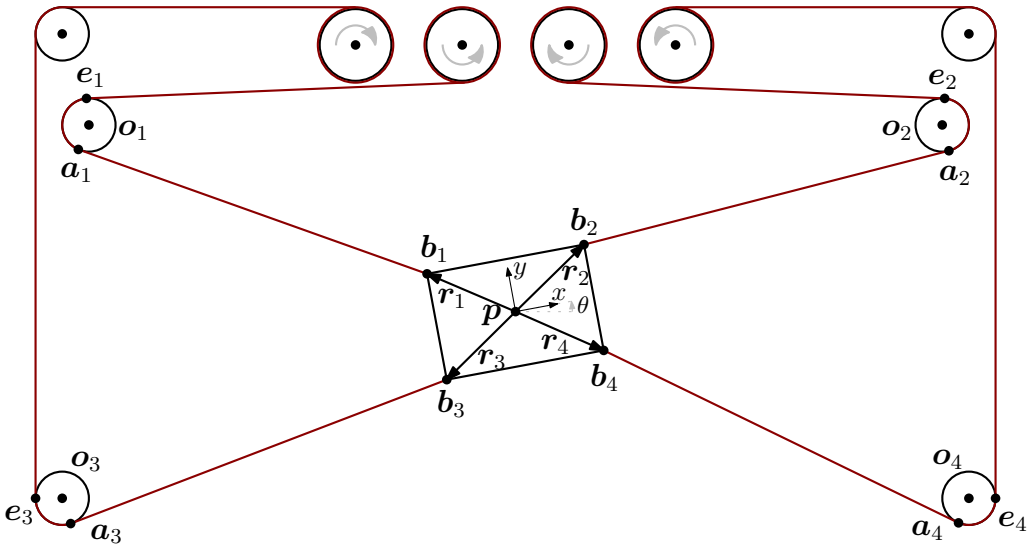

Figure 3.1: A constant-structure CDPR.

studied and used in applications. It is also the simplest of the four classes and is used as starting point for studying the other three. The name 'constant-structure' is chosen as this is the only class where the dynamic structure of the mechanism (being governed by the cable anchor point locations) is fixed.

As an example of a mechanism belonging to this class, consider the planar CDPR shown in Fig. 3.1, designed using several cable routing pulleys such that all winches are located close to one another. As a planar rigid body, the configuration of the mobile-platform end effector can be represented by point $\boldsymbol{p}$ and orientation angle θ giving a task space of $\mathcal{T} \subset \mathbb{R}^2 \times S^1$. By inspection, it can be seen that the only section of each cable that varies with movement of the mobile platform are line segment $\overline{\boldsymbol{a}_i\boldsymbol{b}_i}$ and arc $\widehat{\boldsymbol{e}_i\boldsymbol{o}_i\boldsymbol{a}_i}$; all other segments making up the cable paths are constant due to being fully constrained by fixed objects at both ends. Thus, since points $\boldsymbol{e}_i$ and $\boldsymbol{o}_i$ are constant, the configuration of each cable depends on $\boldsymbol{a}_i$ and $\boldsymbol{b}_i$ alone and can be represented as such.

Combining the platform configuration with the configuration of each cable, the complete robot configuration is specified by the following generalized

coordinates:

$$\boldsymbol{q} = (\boldsymbol{p}, \theta, \boldsymbol{a}_1, \boldsymbol{b}_1, \cdots, \boldsymbol{a}_4, \boldsymbol{b}_4) \tag{3.1}$$

where $\boldsymbol{q}$ is a point in the C-space, resulting in a 19 dimensional C-space of $\mathcal{C} \subset \mathcal{T} \times \mathbb{R}^{16}$; however, the dimensionality of $\mathcal{C}$ can be reduced by introducing a set of 16 holonomic constraints to define each of the cable configuration parameters explicitly in terms of $\boldsymbol{p}$ and θ. From the specified geometry, it can be seen that, for each cable,

$$\boldsymbol{b}_i = \boldsymbol{p} + \boldsymbol{R}(\theta)\boldsymbol{r}_i \tag{3.2}$$

In order for the curvature of each cable's path to be continuous, $\overline{\boldsymbol{a}_i\boldsymbol{b}_i}$ must be tangent to pulley o_i at point $\boldsymbol{a}_i$. Thus, $\boldsymbol{a}_i$ can be found as a function of $\boldsymbol{b}_i$ using the approach outlined in Section A.3 to determine the wrap-direction consistent tangent to pulley o_i that contains $\boldsymbol{b}_i$. Since $\boldsymbol{b}_i$ is itself a function of $\boldsymbol{p}$ and θ, the following constraint can be employed to state $\boldsymbol{a}_i$ in terms of the platform coordinates directly:

$$\boldsymbol{a}_i = \boldsymbol{f}_i(\boldsymbol{b}_i(\boldsymbol{p}, \theta)) \tag{3.3}$$

where $\boldsymbol{f}_i$ is as defined in Section A.3. After applying Eqs. (3.2) and (3.3) for each cable, the C-space dimensionality is reduced to 3 with $\boldsymbol{q}$ becoming

$$\boldsymbol{q} = (\boldsymbol{p}, \theta) \tag{3.4}$$

resulting in a C-space of $\mathcal{C} = \mathcal{T}$ which depends only on the platform pose.

3.1.2 Class 2: Reconfigurable

Definition 2 (Reconfigurable CDPR)**.** A CDPR whose configuration depends on additional DOF beyond the platform pose.

The precise naming comes from its previous use in the literature [70, 71].

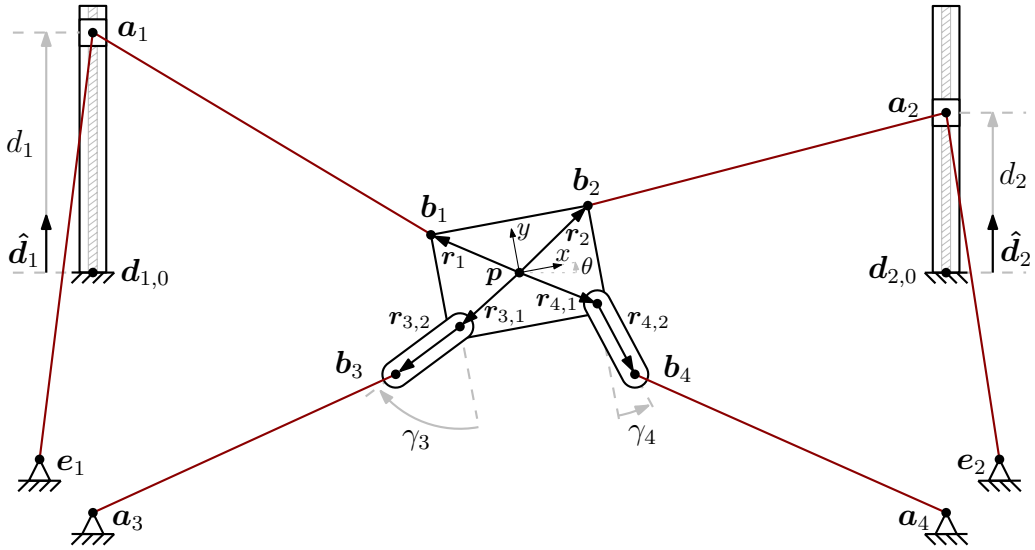

Figure 3.2: A reconfigurable CDPR.

They have also been referred to as 'mobile CDPRs' in instances where the winches are located on a freely movable base [72]. A mechanism of this class is created when additional actuators, in either the fixed frame or on the mobile platform, provide direct control over cable anchor-point locations, enabling them to be actively reconfigured. Consider, for example, the planar CDPR shown in Fig. 3.2: the mobile platform is suspended by four cables ($c_{1\text{–}4}$), each exiting from ground-fixed winches with drive pulleys of negligible radius; two actuated swing arms are connected to the mobile platform by revolute joints located at $\boldsymbol{r}_{3,1}$ and $\boldsymbol{r}_{4,1}$; cables c_1 and c_2 pass through eyelets located at $\boldsymbol{a}_1$ and $\boldsymbol{a}_2$ respectively on their way to the platform; each eyelet is mounted on the sliding table of a linear actuator and able to translate in the directions shown. Once again, the task space is specified by the position and orientation of the end effector: $\boldsymbol{p}$ and θ. By inspection, the path taken by cable c_1 consists of two adjacent line segments: $\overline{\boldsymbol{e}_1\boldsymbol{a}_1}$ and $\overline{\boldsymbol{a}_1\boldsymbol{b}_1}$. As $\boldsymbol{e}_1$ is a fixed point, the configuration of c_1 is fully specified by points $\boldsymbol{a}_1$ and $\boldsymbol{b}_1$.

From the given geometry, $\boldsymbol{a}_1$ and $\boldsymbol{b}_1$ can be expressed as

$$\boldsymbol{a}_1 = \boldsymbol{d}_{1,0} + d_1\hat{\boldsymbol{d}}_1 \tag{3.5}$$

and

$$\boldsymbol{b}_1 = \boldsymbol{p} + \boldsymbol{R}(\theta)\boldsymbol{r}_1 \tag{3.6}$$

respectively, where $\boldsymbol{d}_{1,0}$ and $\hat{\boldsymbol{d}}_1$ are fixed properties and $d_1 \in \mathbb{R}$ constitutes an independent DOF. Applying Eqs. (3.5) and (3.6) directly, it is found that the configuration of c_1 is specifiable by parameters $\boldsymbol{p}$, θ, and d_1. Taking the same approach for c_2 reveals that its configuration can be specified as $\boldsymbol{p}$, θ, and d_2.

In contrast to $c_{1\text{–}2}$, c_3 consists of a single segment: $\overline{\boldsymbol{a}_3\boldsymbol{b}_3}$. $\boldsymbol{a}_3$ is a fixed point and $\boldsymbol{b}_3$ can be specified as

$$\boldsymbol{b}_3 = \boldsymbol{p} + \boldsymbol{R}(\theta)\left(\boldsymbol{r}_{3,1} + \boldsymbol{R}(\gamma_3)\boldsymbol{r}_{3,2}\right) \tag{3.7}$$

where $\gamma_3 \in S^1$ constitutes an independent DOF corresponding to the rotation angle between the platform and the rigid link specified by $\boldsymbol{r}_{3,2}$. thus, the configuration of c_3 can be represented by parameters $\boldsymbol{p}$, θ, and γ_3. Taking the same approach for c_4, its configuration is determined by $\boldsymbol{p}$, θ, and γ_4.

By combining the obtained representations for the configurations of the end effector and four cables, the complete robot configuration is found to be compactly representable as

$$\boldsymbol{q} = (\boldsymbol{p}, \theta, d_1, d_2, \gamma_3, \gamma_4) \tag{3.8}$$

where $\boldsymbol{q}$ constitutes a point in the C-space, leading to a C-space of

$$\mathcal{C} \subset \mathcal{T} \times \mathbb{R}^2 \times T^2 \tag{3.9}$$

Thus, it is shown that the mechanism in Fig. 3.2 is a member of the recon-

figurable class of CDPRs.

3.1.3 Class 3: Variable-Structure

Definition 3 (Variable-Structure CDPR)**.** A CDPR where the anchor points of at least one cable instantaneously switch from one location to another when triggered by an event condition being satisfied, resulting in the entire CDPR configuration depending on both the platform pose and any number of discrete state parameters.

Being described by both continuous and discrete state variables, variable-structure CDPRs (VSCR) constitute a type of hybrid dynamic system. Thus, the name 'variable-structure' has been chosen in keeping with the naming conventions established in the study of hybrid dynamic systems [73]. Unlike the previous two classes, which have been well documented in the literature, VSCRs constitute a new class of CDPRs that have not been previously identified in the literature.

The only possibility for instantaneous relocation of a cable's anchor points is if the new anchor locations are included in the path occupied by the cable immediately prior to relocation. If this were not the case, the cable's path over time would be discontinuous, requiring infinite velocity. One example of how this type of behaviour can be achieved is through collisions.

Consider the planar PM CDPR shown in Fig. 3.3 where Figs. 3.3a and 3.3b demonstrate two distinct configurations of the same system: the mechanism consists of two cables ($c_{1\text{–}2}$) and a fixed, smooth, cylindrical pin of negligible radius located at point $\boldsymbol{v}$; each cable exits from a winch of negligible radius at points $\boldsymbol{e}_i$ and connect to a common point, $\boldsymbol{p}$, which serves as the end effector, giving the mechanism a task space of $\mathcal{T} \subset \mathbb{R}^2$.

In moving from the configuration shown in Fig. 3.3a to Fig. 3.3b, the end effector crosses $S_{\text{sw},2}$, at which point cable c_2 collides with and begins to wrap around the pin located at point $\boldsymbol{v}$. The cable path prior to collision,

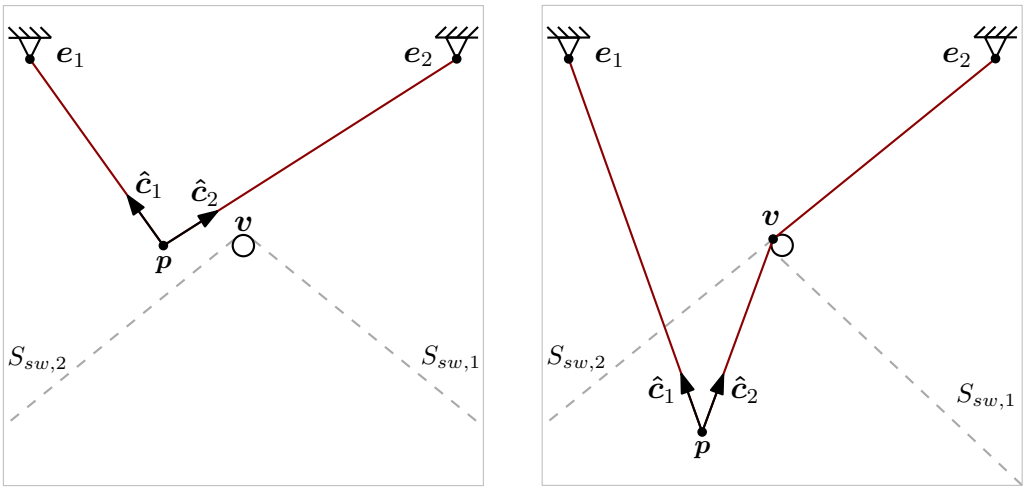

Figure 3.3: A variable-structure CDPR: (a) and (b) demonstrate two distinct configurations of the same system.

denoted as c_2^-, consists of a single line segment: $\overline{\boldsymbol{e}_2\boldsymbol{p}}$. After colliding with the pin, the cable path switches to $c_2^+ = (\overline{\boldsymbol{e}_2\boldsymbol{v}}, \overline{\boldsymbol{v}\boldsymbol{p}})$. The transition between c_2^- and c_2^+ is instantaneous and takes place at the exact moment that $\boldsymbol{p}$ crosses from one side of $S_{\text{sw},2}$ to the other. If the state of c_2 is known (in terms of the sequence of segments that make up its path), then the only additional information required for describing the configuration of c_2 is $\boldsymbol{p}$, since points $\boldsymbol{e}_2$ and $\boldsymbol{v}$ are both constant. In order to represent which state the cable is in, a discrete parameter $h_2 \in H_2$ is introduced where H_2 is the set of all possible states for cable c_2 and is defined as

$$H_2 = \{\overline{\boldsymbol{e}_2\boldsymbol{p}}, (\overline{\boldsymbol{e}_2\boldsymbol{v}}, \overline{\boldsymbol{v}\boldsymbol{p}})\} \tag{3.10}$$

Thus, the configuration of c_2 can be represented by parameters $\boldsymbol{p}$ and h_2. Applying the same analysis to c_1, it is found to be representable by $\boldsymbol{p}$ and $h_1 \in H_1$ where H_1 is the set of all possible states for cable c_1 and is defined

as

$$H_1 = \{\overline{\boldsymbol{e}_1\boldsymbol{p}}, (\overline{\boldsymbol{e}_1\boldsymbol{v}}, \overline{\boldsymbol{v}\boldsymbol{p}})\} \tag{3.11}$$

By combining the configurations of each cable with the configuration of the end effector, the complete robot configuration can be represented as

$$\boldsymbol{q} = (\boldsymbol{p}, h_1, h_2) \tag{3.12}$$

where $\boldsymbol{q}$ is a point in the C-space, resulting in a C-space of

$$\mathcal{C} \subset \mathcal{T} \times H_1 \times H_2 \tag{3.13}$$

Thus, the mechanism in Fig. 3.3 is shown to be a member of the variable-structure class of CDPRs.

3.1.4 Class 4: Reconfigurable Variable-Structure

Definition 4 (Reconfigurable VSCR)**.** A VSCR whose configuration depends on additional DOF beyond the platform pose.

Reconfigurable VSCRs constitute another previously unidentified class of CDPRs that combine the features of classes 2 and 3. An example of a member of this class would be a VSCR with collidable objects that are free to move independently. Another example is the planar point mass (PM) CDPR shown in Fig. 3.4 where Figs. 3.4a and 3.4b demonstrate two distinct configurations of the same system: the mechanism consists of two cables ($c_{1\text{–}2}$) and a fixed, smooth, cylindrical pin of negligible radius located at point $\boldsymbol{v}$; each cable exits from a winch of negligible radius at points $\boldsymbol{e}_i$ and connects to a common point $\boldsymbol{p}$; the winch for cable c_2 is mounted on the sliding table of a linear actuator and able to translate in the direction shown. Point $\boldsymbol{p}$ serves as the end effector, giving the mechanism a task space of $\mathcal{T} \subset \mathbb{R}^2$.

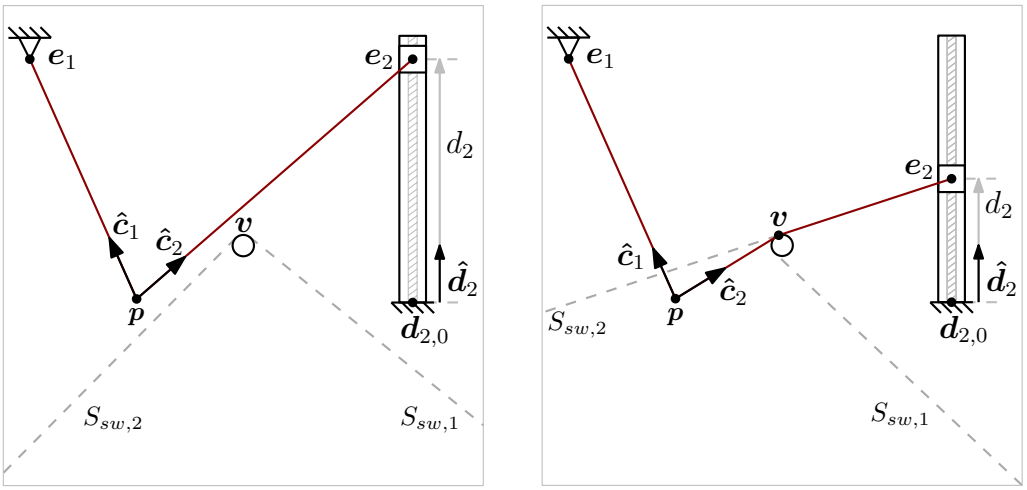

Figure 3.4: A reconfigurable variable-structure CDPR: (a) and (b) demonstrate two distinct configurations of the same system.

The approach to be taken for analysing Fig. 3.4 is identical to that which was taken for analysing the mechanisms shown in Fig. 3.2 and Fig. 3.3. The configuration of c_1 is specified by point $\boldsymbol{p}$ and discrete parameter $h_1 \in H_1$ where H_1 is the set of all possible states for cable c_1 and is defined as

$$H_1 = \{\overline{\boldsymbol{e}_1\boldsymbol{p}}, (\overline{\boldsymbol{e}_1\boldsymbol{v}}, \overline{\boldsymbol{v}\boldsymbol{p}})\} \tag{3.14}$$

Point $\boldsymbol{e_2}$ is variable and defined as

$$\boldsymbol{e}_2 = \boldsymbol{d}_{2,0} + d_2\hat{\boldsymbol{d}}_2 \tag{3.15}$$

where $d_2 \in \mathbb{R}$ is an independent DOF. Thus, the configuration of c_1 depends on $\boldsymbol{p}$, d_2, and discrete parameter $h_2 \in H_2$ where H_2 is the set of all possible states for cable c_2 and is defined as

$$H_2 = \{\overline{\boldsymbol{e}_2\boldsymbol{p}}, (\overline{\boldsymbol{e}_2\boldsymbol{v}}, \overline{\boldsymbol{v}\boldsymbol{p}})\} \tag{3.16}$$

Combining the configurations of each cable with the configuration of the end effector, the complete robot configuration is specifiable as

$$\boldsymbol{q} = (\boldsymbol{p}, d_2, h_1, h_2) \tag{3.17}$$

resulting in a C-space of

$$\mathcal{C} \subset \mathcal{T} \times \mathbb{R}^1 \times H_1 \times H_2 \tag{3.18}$$

It is worth noting that switching surface $S_{\text{sw},2}$ depends on parameter d_2: despite the fact that $\boldsymbol{p}$ does not change between Figs. 3.4a and 3.4b, c_2 undergoes a state change due the movement of $\boldsymbol{e}_2$ induced by changes in parameter d_2. What is shown in Fig. 3.4 are merely intersections of $S_{\text{sw},2}$ with the (x, y) plane for the given values of d_2.

3.2 Properties of VSCRs

The variable-structure nature of VSCRs, as defined in this thesis, is achieved by allowing collisions between cables and rigid objects fixed in the environment: any time a collision occurs along the length of a cable, the effective anchor points change instantaneously, leading to a corresponding change in the dynamic structure of the mechanism. In this thesis, other types of collisions (such as those occurring between cables or between the cables and the mobile platform) are not considered.

It is assumed that cables are always under tension and, therefore, taut. This assumption leads to the expected behaviour that cables wrap around a collided object following the convex contour of the object's surface. An important assumed restriction is that sliding between objects and cables occurs only in the tangential direction. This assumption always holds for planar systems. For spatial systems, the design process for object selection and placement is far more complicated, and surface stability must be considered

to guarantee that no cable slippage occurs in the axial direction. As an example of an unstable surface, consider the contact between a cable and a sphere.

A design consideration unique to VSCRs is the type of collidable objects to be used. As a cable's length changes during actuation, sliding will occur along the regions of contact between the cable and collided objects. This sliding generates concern for the longevity of the cables: friction between the two surfaces and excessive bending may lead to premature wear of the cable. In general, the collidable objects should be as smooth and round as the application allows to minimize friction and bending loads placed on the cables. To this end, idler pulleys may serve as a good candidate object so long as the mouth of the pulley is wide enough to ensure reliable capture of the cable during a collision approach. In certain applications, such as disaster relief, where there is little control over the environment, and short-term adaptability is more important than long-term continuous operation, there may be a higher tolerance for allowable friction and cable wear.

One of the ways that the capabilities of VSCRs differ from traditional CDPRs is in the type of workspaces they can cover. Any collision along the length of a cable where the cable wraps around the collided object will result in the cable being divided into two segments that always have a reflex interior angle between them. Therefore, it can be concluded that the reachable workspace for a VSCR resulting from collisions between cables and a set of fixed objects is non-convex due to the presence of reflex interior angles between adjacent cable segments.

Of the four classifications of CDPRs discussed earlier, VSCRs are the only ones capable of modifying the sequences of cable segments, with segments being added or removed after each collision or separation. It is this unique property that allows VSCRs to cover workspaces impossible for constant-structure or reconfigurable CDPRs. The ability to cover non-convex workspaces significantly enhances the design freedom and range of applications for which

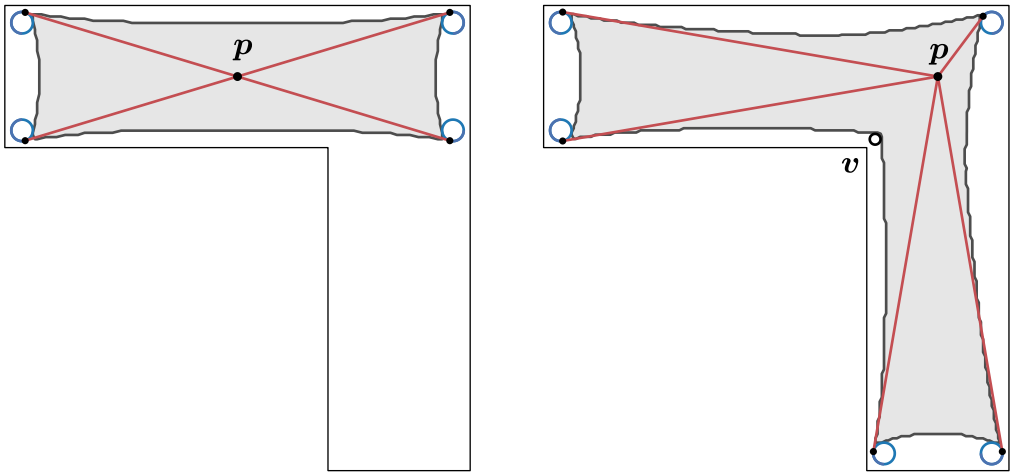

(a) (b)

Figure 3.5: Comparison of CDPR and VSCR capabilities: for a given ⌝-shaped installation space, (a) and (b) show the maximum workspace that can be covered using either a CDPR or VSCR, respectively.

CDPRs can be used. This ability is especially useful for extending the usable workspace in cluttered environments and as a collision avoidance strategy: cables can be made to avoid regions where cable inference would be unsafe by colliding with and bending around a set of permissible objects instead. Consider, for example, the design scenario shown in Fig. 3.5, where it is desired to cover the maximum amount of a ⌝ shaped installation space while avoiding cables from colliding with any walls. With a 4-cable constant-structure CDPR, the maximum workspace that can be covered is shown in Fig. 3.5a; however, by adding an additional cable and placing a collidable idler pulley at the interior corner at point $\boldsymbol{v}$, as shown in Fig. 3.5b, nearly the entire installation space can be covered.

3.3 Summary

In this chapter, a classification system for CDPRs has been introduced that identifies four separate classes: constant-structure, reconfigurable, variable-structure, and reconfigurable variable-structure, the latter two being newly identified forms that have not been previously discussed in the literature. Each of the four classes is then defined, described, and demonstrated.

VSCRs are distinct from traditional CDPRs in that they are a type of hybrid dynamic system, able to instantaneously change their dynamic structure through collisions between cables and objects fixed in the environment. Additionally, It is found that VSCRs possess the unique ability to cover non-convex installation spaces. By allowing cables to collide with a set of permissible objects, cables can be safely prevented from entering forbidden areas or colliding with obstacles: a property that can be used to significantly extend the usable workspaces CDPRs can achieve in cluttered environments.

The remaining chapters investigate specific technical aspects related to the modelling and analysis of VSCRs.

Chapter 4

Collidable Cables

The objective and contribution of this chapter is to provide a solution to the inverse kinematics problem for planar VSCRs: an essential foundation for enabling further VSCR research. To this end, an extended cable model for representing cables that can wrap around collidable objects, such as idler pulleys, is introduced. Additionally, an online method for updating the configuration of collidable cables is presented and used as part of a two-step process for iteratively solving the planar VSCR inverse kinematics problem. The methods discussed in this chapter are general and readily applicable. A set of examples have been included to demonstrate application of the presented inverse kinematics method to VSCR trajectory planning.

The outline of the chapter is as follows: Section 4.1 presents an extended cable model for representing collidable cables; Section 4.2 gives an online algorithm for iteratively updating cable states; Section 4.3 presents a two-step online inverse kinematics method. Section 4.4 provides a detailed example to demonstrate application of the developed inverse kinematics methodology; Section 4.5 summarizes the main results and concludes the chapter.

4.1 Representation of Collidable Cables

This section introduces the concept of a cable state to represent cables once collisions are allowed. A specific method for representing collidable cables is presented, and its merits, as well as its necessity, are discussed. The proceeding analysis is based on the assumption that one end of a cable is connected to a winch and the other end is able to move freely. This assumption is relevant to the situation experienced in CDPRs, where one cable end is usually attached to a fixed winch and the other to the mobile platform. It is also assumed that cables are always held under tension and, therefore, taut. Cable platform and fixed-frame anchors are assumed to be single points as this is a common assumption made in the CDPR literature. Circular objects are the only type of objects analyzed because of their practical value for minimizing cable wear caused by sliding friction and acute bending; however, the method presented is general and can easily be extended to include collisions with any object type, so long as the geometry is well defined. For example, a polygonal structure could be represented by replacing each vertex with either a single point or a circle of small radius and considering the polygon's interior as a disallowed region.

4.1.1 Cable State

In traditional CDPRs, where collisions are not considered, there is nothing to change the path of a cable to be anything other than a straight-line segment connecting its two end points. In some studies, effects such as cable sagging have been considered; however, even in the case of sagging, given the tension in the cable is known, there is only one possible solution for a cable's path if both end points are known. As Fig. 4.1 demonstrates, multiple cable paths become possible for a given pair of end points once collidable objects are introduced, requiring additional information to be tracked to represent a cable's configuration completely.

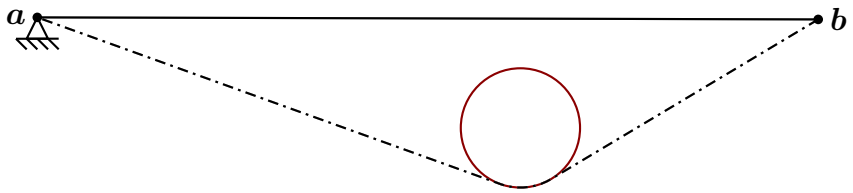

Figure 4.1: Demonstration of cable path ambiguity in the presence of collidable objects. Given cable endpoints $\boldsymbol{a}$ and $\boldsymbol{b}$ and the presence of a single circular object, two cable paths are possible (shown using solid and dashed lines).

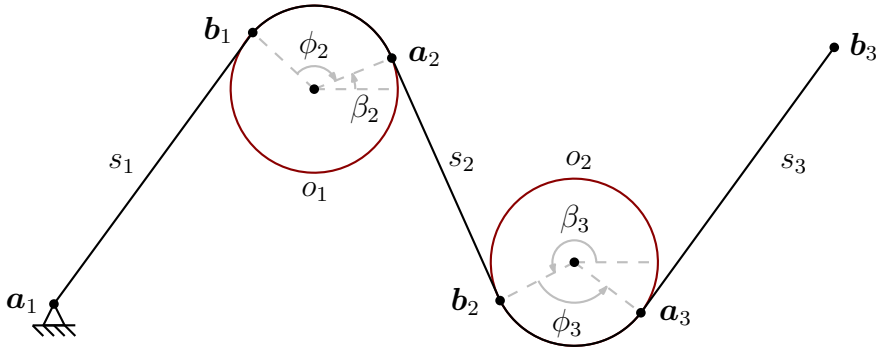

Figure 4.2: Cable with end points $\boldsymbol{a}_1$ and $\boldsymbol{b}_3$, represented as a list of segments: $\{s_1, s_2, s_3\}$. In the given configuration, the cable collides with two circular objects: o_1 and o_2.

In order to address the complexity of a collidable cable's path in a compact yet unambiguous way, the concept of a 'cable state' is introduced and defined as the minimum set of information required to reconstruct a cable's path fully. One way a cable's state can be represented is as a list of line segments, defined in terms of the objects in contact with the cable. As an example, consider the cable shown in Fig. 4.2: in the configuration shown, the cable path consists of three line segments and two wrapping segments due to the collisions with the two circular objects. If the geometry of the collided objects is known, then the wrapping segments and, therefore, the entire cable path can be reconstructed from knowledge of $\{s_1, s_2, s_3\}$ alone.

Each collision can be represented by three pieces of information: the entry

point, exit point, and cable wrap direction. The line segments entering and exiting an object will always be tangent to the surface of that object; thus, by finding the common tangent between the collided object and both ends of the colliding segment, the entry and exit points for the collision can be determined. Methods for computing the common tangents between a point and a circle as well as between two circles are provided in Chapter A.

For implementing the cable state representation discussed above, the data structure provided in Alg. 4.1 may be used, which captures all the required information for a single cable segment. A cable state can be represented as a linked list by connecting individual segment structures together. Segments

Algorithm 4.1: Cable-segment representation.

Struct *segment* **contains**
- previousSegment;
- nextSegment;
- object1;
- object1_θ_{exit};
- object2;
- object2_θ_{entry};
- object2_$wrapDir$;

in Alg. 4.1 have been defined in terms of the object entry and exit angles rather than entry and exit points in order to simplify determining wrap angles (which will become helpful in Section 4.2); however, it is trivial to convert angle information into segment end points and vice-versa if the geometry of the objects is known. Consider for example an object with entry and exit points defined as $\boldsymbol{p}_1$ and $\boldsymbol{p}_2$ respectively. Given the entry and exit angles, $\boldsymbol{p}_1$ and $\boldsymbol{p}_2$ can be obtained as

$$\boldsymbol{p}_1 = r(\theta_{\text{entry}}) \cdot \begin{bmatrix} \cos(\theta_{\text{entry}}) \\ \sin(\theta_{\text{entry}}) \end{bmatrix} \tag{4.1}$$

and

$$\boldsymbol{p}_2 = r(\theta_{\text{exit}}) \cdot \begin{bmatrix} \cos(\theta_{\text{exit}}) \\ \sin(\theta_{\text{exit}}) \end{bmatrix} \tag{4.2}$$

where $r(\theta)$ represents the radius of the object at a given angle θ. For the cable fixed-frame and platform anchors, the entry angle, exit angle, and cable wrap direction members are all undefined since the cable ends are modeled as single points.

4.2 Cable State Tracking

As the mobile platform moves throughout its workspace, the state of all attached cables must be updated accordingly. To this end, there is a need for an online method of computing cable state changes resulting from end effector movement.

Assuming that all collidable objects are fixed, a cable's path is divisible into a set of static segments and a single active segment. The active segment refers to the final segment along a cable's path: the segment attached to the cable's platform end. Since the active segment contains the cable's platform end, any change in the end effector's configuration results in a change in the active segment's configuration as well. The static segments consist of all cable segments between the winch and the active segment. The static segments are named as such because fixed objects on both ends constrain their geometry. The end points for each of the static segments are determined by the common tangents between the two objects adjacent to the respective segment, as discussed in Section 4.1.

There are an infinite number of possible active segment configurations due to one end of the segment being free; however, for any cable in the presence of a finite number of objects, the number of possible static segment configurations is finite since there are always a finite number of common tangents between two objects and a finite number of possible sequences with

which such segments can be combined. Since the set of all possible sets of static segments is finite and dependent only on the fixed geometry of the collidable objects and a cable's winch location, it can be precomputed offline. This potential for precomputation becomes very useful for reducing the online computational demand in iteratively updating a cable's state during platform motions, as will be shown in the proceeding subsections.

4.2.1 Cable-State Tree

Based on the cable state representation proposed in Section 4.1, a cable's state consists of a list of line segments, defined in terms of the objects at the end of each respective segment. If the list of segments making up a cable's state is ordered lengthwise, such that the start point of the first segment is the fixed-frame cable anchor and the final point of the final segment is the platform-fixed cable anchor, the set of all possible sets of static segments takes the form of a tree. This tree structure will be referred to as the 'cable-state tree' (CST) from here onward.

Each node in the CST is associated with and contains information regarding a single static segment; the sole exception is the root node which represents the cable winch. Starting from the cable winch, the CST can be built by adding a new child node for each directly reachable static segment. Repeating this process recursively until all nodes have been expanded, the resulting tree structure will encapsulate all possible paths the static portion of a cable can take. This idea is demonstrated in Fig. 4.3 where a single collidable cable and its corresponding CST are shown.

When constructing the CST, for a potential segment to be considered reachable, the segment must not intersect with any object or previous segments along the cable's path. Additionally, a potential segment must not enter any disallowed regions: regions within the installation space that must be kept free from cable interference by design or circumstance. For disallowed regions defined by a bounding polygon, violations can be determined

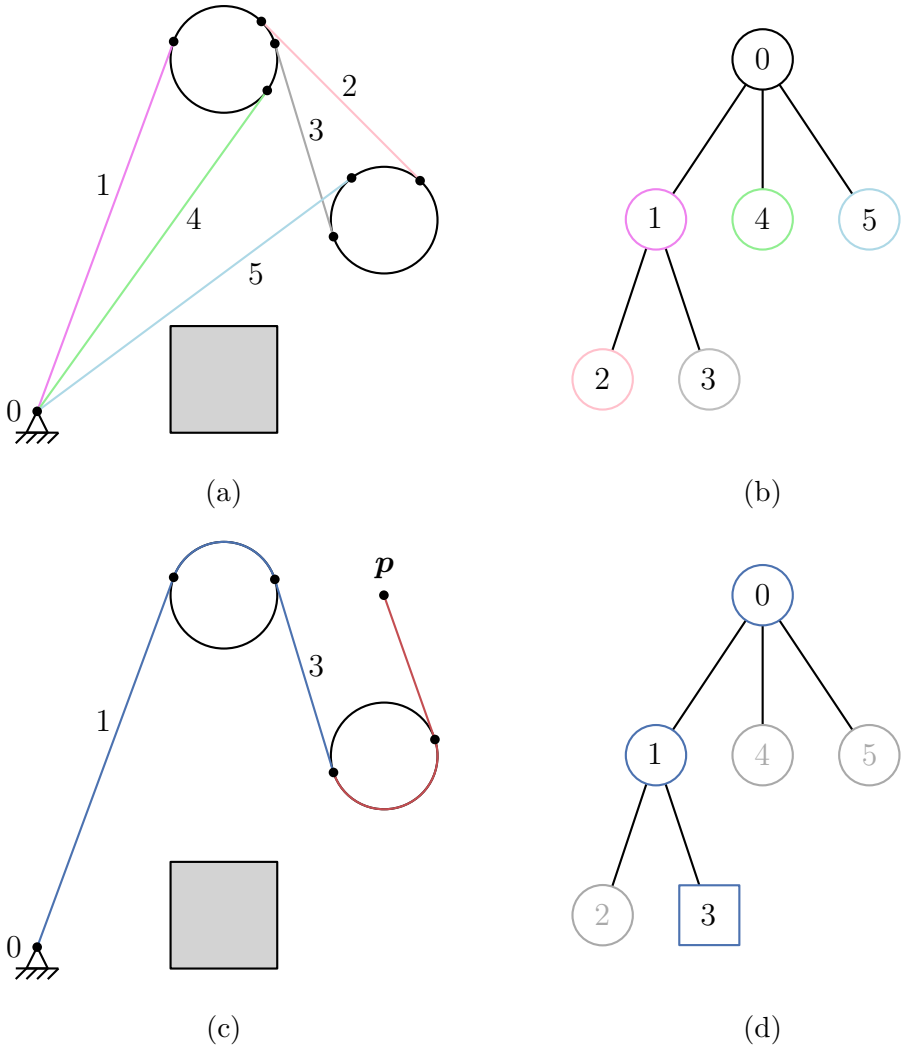

Figure 4.3: CST formation for a cable with two circular objects present: the set of possible static segments is shown in (a) with each segment assigned a unique number; the gray square in (a) represents a disallowed region. The resulting CST is shown in (b) with node numbers matching the segments in (a). (c) provides an example cable configuration with static segments shown in blue and the active segment shown in red; the tracked CST node for the configuration in (c) is marked with a square in (d).

by checking if there is any interception between the potential segment and each edge of the bounding polygon. Methods for detecting if there is any interception between two line segments and between a line segment and a circle are provided in Chapter A.

Once the CST has been built, it is sufficient to track only the node corresponding to the final static segment along the cable's path: the complete list of static segments can be obtained by traversing up the tree and taking the segments at each node. The configuration of a cable, c, can therefore be tracked compactly as

$$C = \{N, B\} \tag{4.3}$$

where N is the tree node associated with the current final static segment. B is a special node used to represent the active segment whose parent is always N and set of children is always empty.

The CST can be built using the function presented in Alg. 4.3, which makes use of the data structure presented in Alg. 4.2 for representation of the CST nodes. Implementation of the 'findCommonTangents' function is dependent on the geometry of the given object. For circular objects, the content of Chapter A can be used as a reference for implementation. In applications where the number of objects is large, and the cost of computing the entire tree would be prohibitive, a functional subtree can be built online with nodes only being expanded as needed.

Algorithm 4.2: CST node data structure.

Struct *node* **contains**
- parent;
- children;
- object1;
- object1_θ_{exit};
- object2;
- object2_θ_{entry};
- object2_$wrapDir$;

Algorithm 4.3: Recursively build CST.

```
Function findAllChildren (node, objects)
    foreach object ∈ objects do
        S ← findCommonTangents(node.object2,object);
        foreach segment ∈ S do
            if segment is unobstructed then
                findAllChildren(segment, objects);
                node.addChild(segment);
            end
        end
    end
end
```

4.2.2 Cable-State Update Algorithm

Given the state of a cable at a particular time, $c(t) = \{N(t), B(t)\}$ and the position of the cable's platform end after a small amount of time has passed, $\boldsymbol{b}(t + dt)$, the goal is to determine the resulting cable state at time $t + dt$. In order to solve for $c(t + dt)$, it must first be determined if the cable has detached from any previously collided objects or if any new collisions have occurred between times t and $t + dt$.

Anytime the wrap angle around an object becomes negative, the cable will separate from the respective object, requiring the final segment along the sequence of static segments to be removed. This process can be performed by repeatedly transitioning the tracked CST node N to its parent until the resulting node possesses a positive wrap angle.

Once all unwrapped segments have been removed from the cable's path, the next step is to add any new collisions that occurred during the motion. Based on the properties of the CST, it is known that any possible state transition resulting from a new collision must be a child of the current CST node. Therefore, only the children of the tracked CST node need to be

checked for possible transition. The active segment at time t (represented as B_{t_1}) is already known and provided. The active segment at time $t + dt$ (represented as B_{t_2}), can be calculated by finding the wrap-direction-consistent common tangent between $\boldsymbol{b}(t + dt)$ and the object at the end point of the tracked CST node. Consider the cable shown in Fig. 4.4a: the angular displacement of the active segment between times t and $t + dt$ can be determined as

$$\Delta\alpha = (\alpha_{t_2} - \alpha_{t_1}) \tag{4.4}$$

where

$$\alpha_{t_i} = \text{atan2}(B_{t_i}.b - B_{t_i}.a) \tag{4.5}$$

The sign of $\Delta\alpha$ gives the prevailing direction of the experienced motion:

$$dir = \text{sign}(\Delta\alpha) \tag{4.6}$$

The angular distance between the ith child of the tracked CST node and the active segment at time t can be found as

$$\theta_i = (\alpha_i - \alpha_{t_1}) \cdot dir \tag{4.7}$$

For a collision to have occurred during the experienced motion, there must exist a child segment where $0 < \theta_i < |\Delta\alpha|$. It is also necessary that the length of the child segment be smaller than the length of B_{t_2}. If multiple child segments satisfy the collision requirements, the child segment with the smallest angular displacement in the direction of $\Delta\alpha$ whose magnitude is less than the magnitude of B_{t_2} corresponds to the actual collision experienced (see Fig. 4.4a). If multiple child segments result in the same minimum angular displacement, the resulting collision will correspond to the child segment with the largest magnitude smaller than B_{t_2}, as demonstrated in Fig. 4.5.

Once the child node corresponding to the actual collision experienced has been identified, the tracked CST node must transition to the corresponding

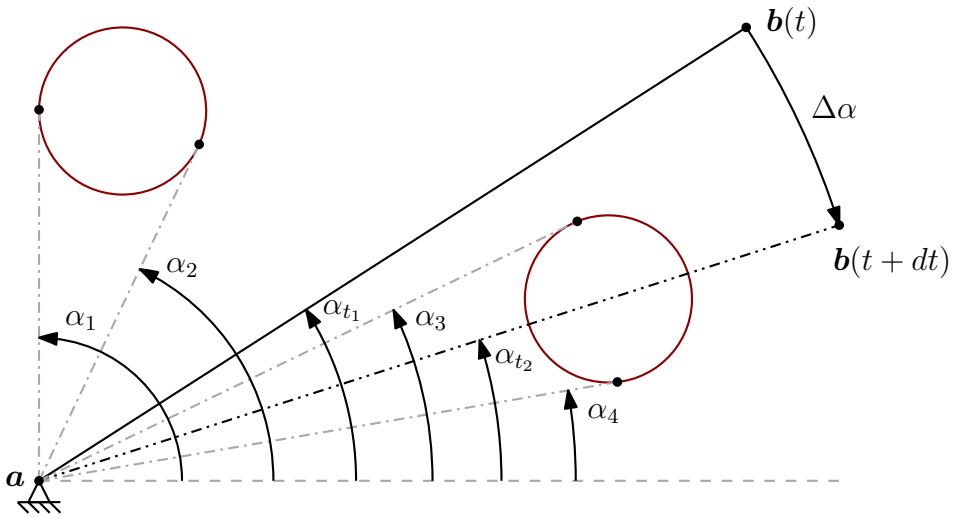

(a) Angular displacement comparison for collision detection.

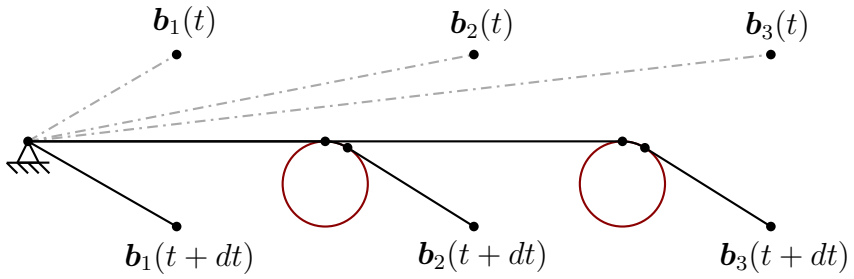

Figure 4.5: Effect of segment magnitude on resulting wrapping.

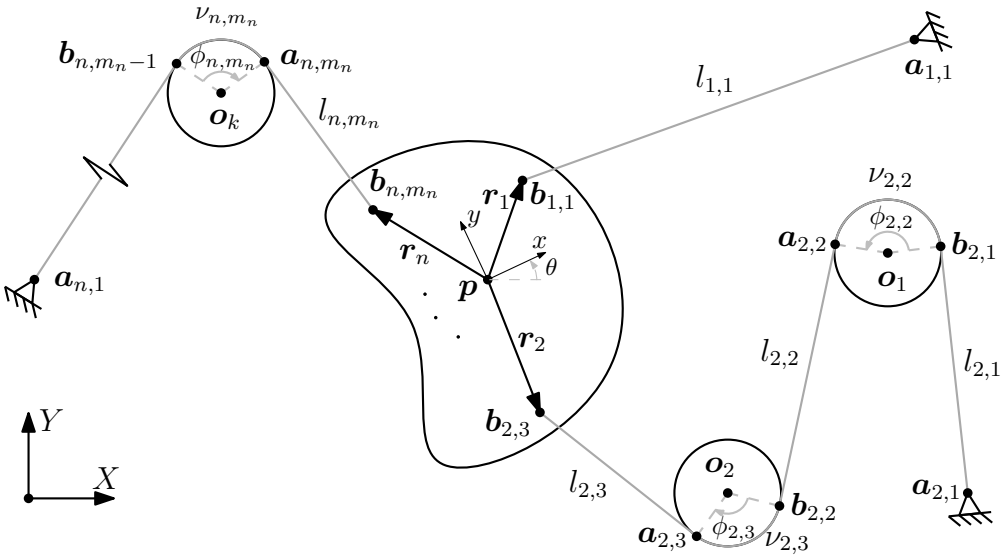

Figure 4.6: Kinematic description of a general planar VSCR.

child and the active segment updated. It is possible that multiple collisions may occur during a single motion. Because of this, the process of identifying potential collisions must be repeated until the resulting CST node contains no children that satisfy the collision requirements. This entire procedure for updating the state of a cable is implemented by the algorithm presented in Alg. 4.4.

4.3 Inverse Kinematics

The problem of interest addressed in this section is to determine the cable lengths required to hold the end effector of a given VSCR at a desired position, $\boldsymbol{p}$, and orientation angle θ. In general, there are multiple possible solutions for each cable leading to there being no direct solution available; however, the inverse kinematics problem can be solved iteratively, given a set of initial cable states and the cable state update algorithm presented in Section 4.2.2.

Consider the general planar VSCR shown in Fig. 4.6 that consists of a rigid platform suspended by n cables in the presence of k fixed collidable objects. For aiding the kinematic analysis, a ground frame $\{X, Y\}$ and a body-fixed frame $\{x, y\}$, fixed at point $\boldsymbol{p}$ on the mobile platform are defined, as shown in Fig. 4.6. Each of the n cables can be represented as a sequence of m_i straight line and wrapping segments, where $1 \leq m_i \leq k+1$. The value of m_i is equal to one plus the number of objects in contact with that cable. Each cable also has two end points: $\boldsymbol{a}_{i,1}$, anchored in the fixed frame, and $\boldsymbol{b}_{i,m_i}$, anchored to the mobile platform.

The platform anchor point for the ith cable is expressed in the ground frame as

$$\boldsymbol{b}_{i,m_i} = \boldsymbol{p} + \boldsymbol{R}(\theta)\, \boldsymbol{r}_i \tag{4.8}$$

where $\boldsymbol{r}_i$ is the position of the platform anchor in the body-fixed frame and $\boldsymbol{R}(\theta)$ is the rotation matrix between the body-fixed and ground frames.

The total length of the ith cable, denoted as l_i, can be expressed as a summation of the m_i straight-line and wrapping segments:

$$l_i = \sum_{j=1}^{m_i} (\nu_{ij} + l_{ij}) \tag{4.9}$$

where ν_{ij} and l_{ij} correspond to the wrapping and straight-line segment lengths respectively for the jth segment of the ith cable. If the exiting body is a single point, $\nu = 0$. If the exiting body is circular, ν can be calculated as

$$\nu_{ij} = \phi_{ij}\, r_{ij} \tag{4.10}$$

where ϕ_{ij} is the wrapping angle and r_{ij} is the radius of the jth object along the length of the ith cable. For other types of objects, the wrapping length can be determined in a similar way from study of the relevant geometry. The

length of line segment l_{ij} is calculated as

$$l_{ij} = \|\boldsymbol{b}_{ij} - \boldsymbol{a}_{ij}\| \tag{4.11}$$

where $\boldsymbol{a}_{ij}$ and $\boldsymbol{b}_{ij}$ are the endpoints of the jth line segment along the ith cable.

Thus the inverse kinematics problem for VSCRs can be solved in two stages: for any change in the end effector pose, the cable states can be updated using Alg. 4.4 on pages 54–55. Once the cable states have been updated, the individual cable lengths can be calculated using Eq. (4.9). The limitation of using this approach is that the displacement of the end effector between each update must be small relative to the size of the collidable objects; however, this limitation can be overcome by adjusting the trajectory step size as needed.

4.4 Examples

This section is intended to demonstrate the application of the inverse kinematics approach presented in Section 4.3 to VSCR trajectory generation. To this end, two case studies are analyzed: the inverse kinematics of a single cable and the inverse kinematics of a 4-cable VSCR. In both cases, the end effector is given a trajectory to follow along with initial cable states. The inverse kinematics methodology of Section 4.3 is then applied to compute the required cable length information within a Matlab simulation. In a real system, the obtained length information could then be sent to the cable winch position controllers to produce the desired end-effector motion. In the proceeding subsections, the specifics for each test case are described in detail, along with the obtained results.

4.4.1 Single Cable

In this example, a single collidable cable is given a trajectory to follow in the presence of three circular objects. The cable's fixed frame anchor is located at a constant point $\boldsymbol{a} = [0, 0]^T$. The cable's free end $\boldsymbol{b}$ follows the trajectory

$$\boldsymbol{b} = \begin{bmatrix} t \\ 1 + \cos(\frac{2\pi}{3}t) \end{bmatrix} \tag{4.12}$$

where t runs from 0 s to 4 s. The initial configuration of the cable at the start of the recorded trajectory is a single line segment between $(0, 0)$ and $(2, 0)$. Three idler pulleys of 0.1 m radius are present within the cable's installation space, with center points provided in Table 4.1 on page 56.

The results obtained from the study are presented in Figs. 4.7 and 4.8. Figure 4.8 provides a snapshot of the cable and its corresponding CST at three different points in time along the trajectory. The resulting cable lengths during the execution of the trajectory are presented in Fig. 4.7 along with a comparison to the cable lengths that would have been obtained if no objects were present. Figure 4.7 also highlights the exact times when CST node transitions occur.

4.4.2 VSCR

For the test case analyzed in this subsection, a four-cable VSCR is given a trajectory to follow in the presence of three obstacles. The end effector for the VSCR in question is a single point mass. Therefore, the free ends of all four cables are located at the same point. The fixed frame anchor locations for the four cables are distinct and provided in Table 4.2. The end effector $\boldsymbol{p}$ follows the trajectory

$$\boldsymbol{p} = \begin{bmatrix} 0 \\ -\frac{1}{2} \end{bmatrix} + 0.75 \begin{bmatrix} \cos(\frac{\pi}{5}t) \\ \sin(\frac{\pi}{5}t) \end{bmatrix} \tag{4.13}$$

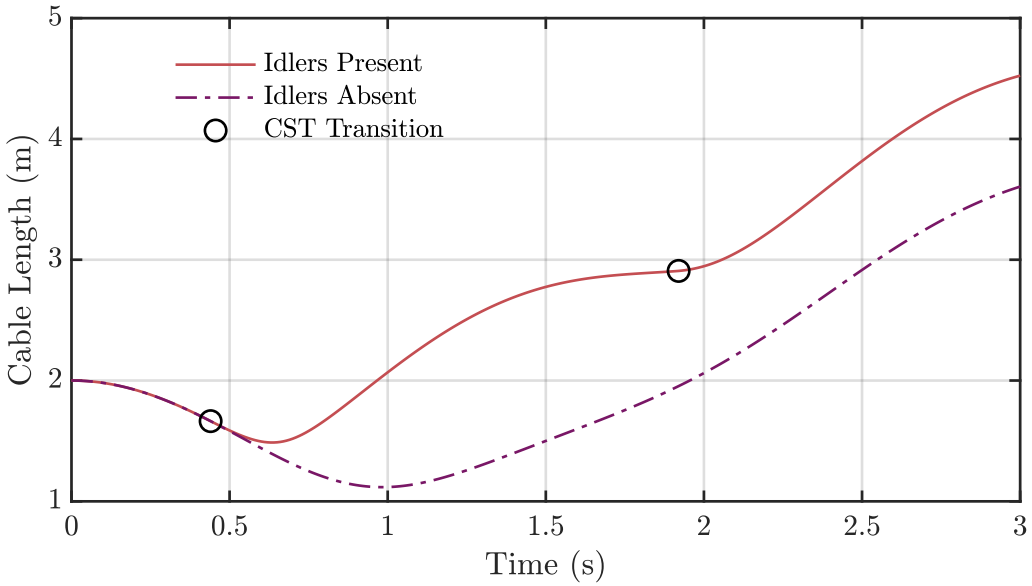

Figure 4.7: Required cable lengths for performing the single cable trajectory described in Section 4.4.1.

where t runs from 0 s to 5 s. The initial configuration of the VSCR at the start of the trajectory is as shown in Fig. 4.9. Three circular objects of 0.15 m radius are present within the VSCR's installation space area with center points provided in Table 4.2. The results obtained from the study are presented in Figs. 4.9 and 4.10. Figure 4.9 provides a snapshot of the VSCR at four different points in time along the trajectory. The resulting cable lengths during the execution of the trajectory are presented in Fig. 4.10 with times corresponding to CST transitions highlighted.

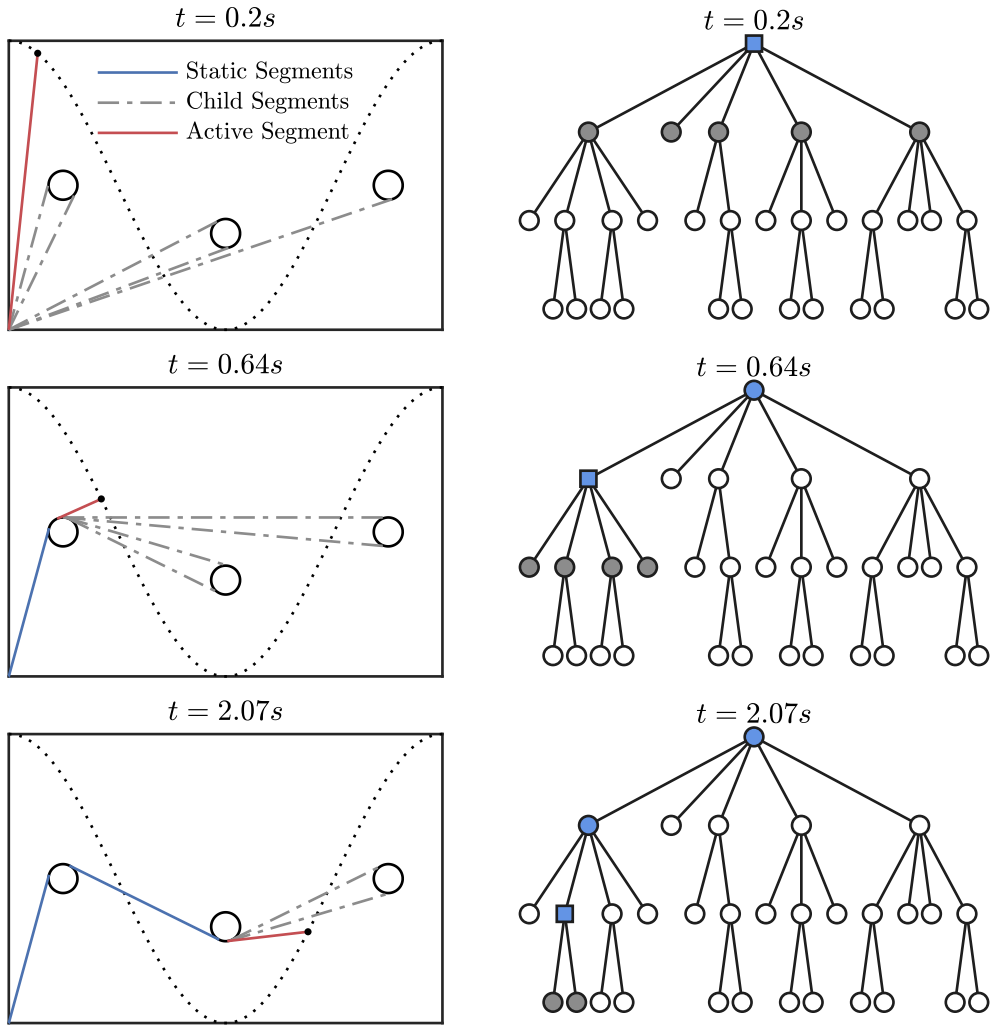

Figure 4.8: Left: visual snapshots of the single-cable trajectory, described in Section 4.4.1, taken at various times with cable segment types highlighted. Right: the corresponding CST over time where the tracked node is shown with a square marker and the nodes that make up the static portion of the cable are shown in blue.

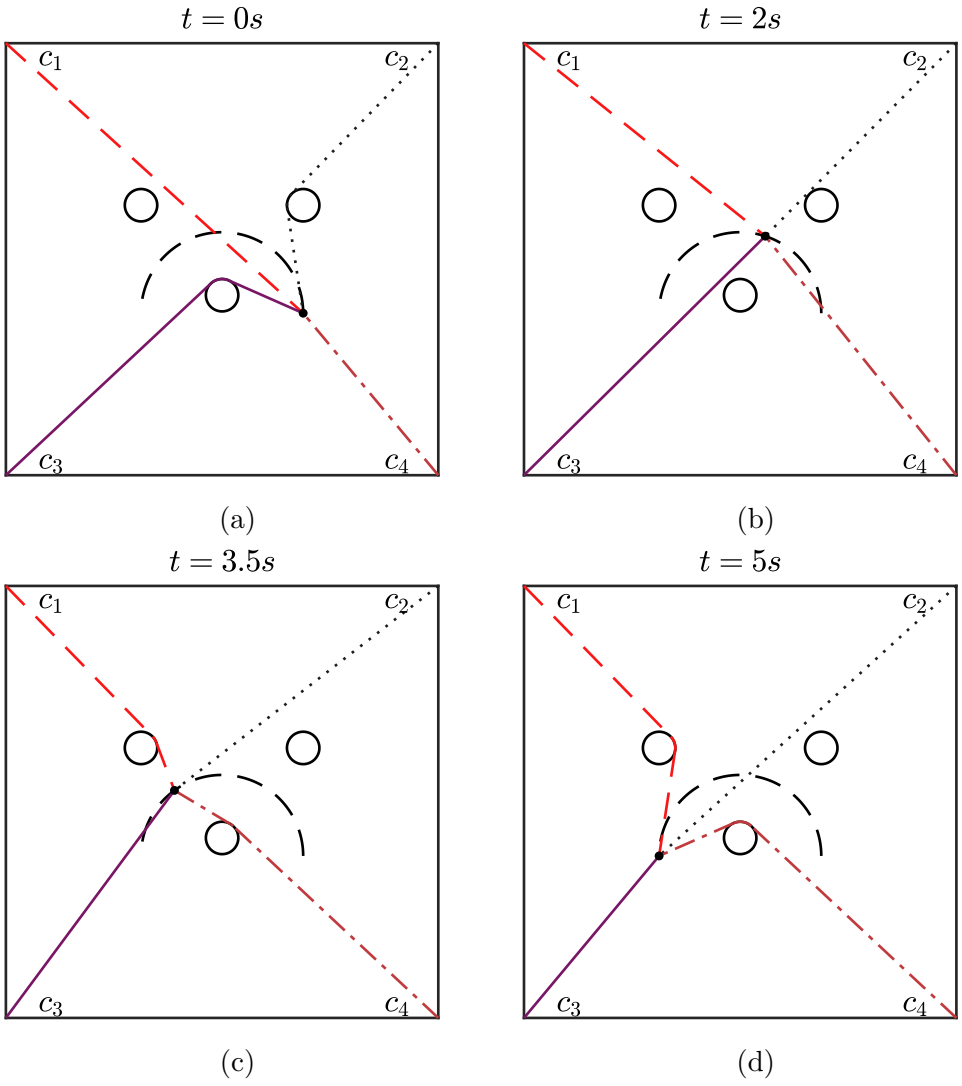

Figure 4.9: Visual snapshots of the four-cable VSCR trajectory described in Section 4.4.2.

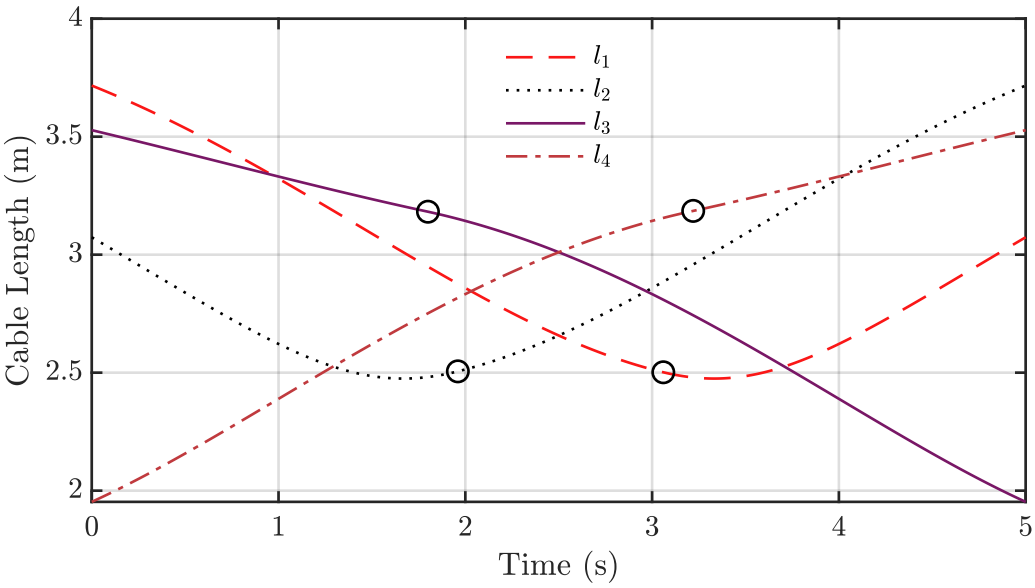

Figure 4.10: Required cable lengths for performing the VSCR trajectory described in Section 4.4.2. Black circles highlight the occurrence of an CST transition for the corresponding cable.

Algorithm 4.4: Update cable state.

input : c(t), b(t+dt)
output: c(t+dt)

```
1  Begin
       /* Initialize                                          */
2      N ← c(t).N;
3      B ← c(t).B;
4      α_{t_1} ← getAlpha(B);
       /* Check for separations.                              */
5      while N.parent ≠ Null do
6          if getWrapAngle(N, b(t+dt)) < 0 then
7              N ← N.parent;
8          else
9              break;
10         end
11     end
       /* Algorithm continued on the next page.              */
```

```
    /* Algorithm continued from the previous page.       */
    /* Check for new collisions.                         */
12  tmp_node ← N;
13  B ← updateB(N, b(t+dt));
14  dir ← sign( getAlpha(B) − α_{t1} );
15  while True do
16      θ_min ← ( getAlpha(B) − α_{t1} ) · dir;
17      m_max ← 0;
18      m_{t2} ← getMag(B);
19      foreach child ∈ N.children do
20          θ ← ( getAlpha(child) − α_{t1} ) · dir ;
21          m ← getMag(child);
22          if 0 < θ < θ_min and m < m_{t2} then
23              θ_min ← θ;
24              m_max ← m;
25              tmp_node ← child;
26          else if θ = θ_min and m_max < m < m_{t2} then
27              m_max ← m;
28              tmp_node ← child;
29      if tmp_node = N then
30          break;
31      else
32          N ← tmp_node;
33          B ← updateB(N, b(t+dt));
    /* Return updated cable state.                       */
34  c(t+dt) ← {N, B};
35  return c(t+dt);
```

Table 4.1: Collidable object locations for the single-cable example discussed in Section 4.4.1.

Object	Center Point (m,m)
1	(3/8, 1)
2	(3/2, 2/3)
3	(21/8, 1)

Table 4.2: Collidable object and cable fixed-frame anchor locations for the VSCR example described in Section 4.4.2.

Cable	Anchor Point (m,m)	Object	Center Point (m,m)
1	(−2, 2)	1	(0, −2/6)
2	(2, 2)	2	(−3/4, 1/2)
3	(−2, −2)	3	(3/4, 1/2)
4	(2, −2)		

4.5 Summary

In this chapter, an extended cable model has been presented for managing the added complexity that arises once cables are permitted to collide with and wrap around fixed objects in the environment. Additionally, the concept of a 'cable state' has been introduced to compactly resolve the cable path ambiguity problem that arises once collisions are permitted. An online method for iteratively updating cable states has been provided and discussed. The method is general and readily applicable. It has been shown that the inverse kinematics problem can be solved iteratively using a two-stage process. First, cable states must be updated after a mobile platform displacement; then, the updated cable states can be converted to cable lengths. The methods described in this chapter have been implemented and validated through a set of experimental studies presented in Chapter 6.

Chapter 5

VSCR Configuration-Space Representation

This chapter presents a general method for determining the set of distinct kinematic structures reachable for a given planar VSCR. Additionally, the concept of a 'structure atlas' is introduced to represent VSCR configuration spaces (C-spaces) and encode the connectivity between structures. The utility of the structure atlas as an important tool for analyzing VSCRs is then demonstrated with its application to workspace analysis and inverse kinematics. The outline of the chapter is as follows: Section 5.1 introduces the concept of the structure atlas and presents a method for its construction for the case of point-mass planar VSCRs; Section 5.2 provides the necessary extensions required to apply the concepts discussed in Section 5.1 for rigid platform based planar VSCRs; Section 5.3 provides structure-atlas-based methods for performing VSCR workspace analysis and inverse kinematics; Section 5.4 summarises and concludes the chapter.

5.1 PM VSCR C-Space Representation

As was shown in Section 2.1.1, if the structure of a CDPR (defined by the set of cable anchor-points) is known, both the change in cable lengths and the effect of cable tensions on the mobile platform can easily be determined as a function of the platform configuration. For traditional CDPRs, the anchor points are constant (or known given a set of holonomic constraints, such as in the case of a cable exiting a pulley). For VSCRs, by definition, this is not the case: every time a cable collides with or separates from a surface during platform motion, the VSCR experiences an instantaneous change in structure, with the anchor point for the affected cable shifting to a new location.

Since collisions between cables and object surfaces only occur at specific locations, there are regions within the configuration space where the structure is constant. In each distinct region of constant structure, the VSCR is locally equivalent to a traditional CDPR. As such, so long as the platform stays within an area where the structure is constant, any methods from the existing CDPR literature can be applied locally. The local equivalence between VSCRs and traditional CDPRs manages much of the added complexity associated with VSCRs (if the local structure is known); however, there has not yet been any proposed approach for how VSCRs can be represented in their entirety. The typical planar CDPR C-space representation as a subset of $\mathbb{R}^2$ (or $\mathbb{R}^3$ for a rigid platform) is insufficient for VSCRs because of the fact that the same platform configuration can potentially be reached under multiple distinct structural configurations (see Fig. 5.1 as an example). Instead, a VSCR C-space can be represented as a collection of overlapping charts, each associated with a distinct region of constant structure that locally map a VSCR's configuration to $\mathbb{R}^2$ and together cover the entire C-space. With this representation, switching charts is synonymous with a change in structure, and within each chart, the local equivalence property holds.

The remainder of this section is devoted to presenting a method for how

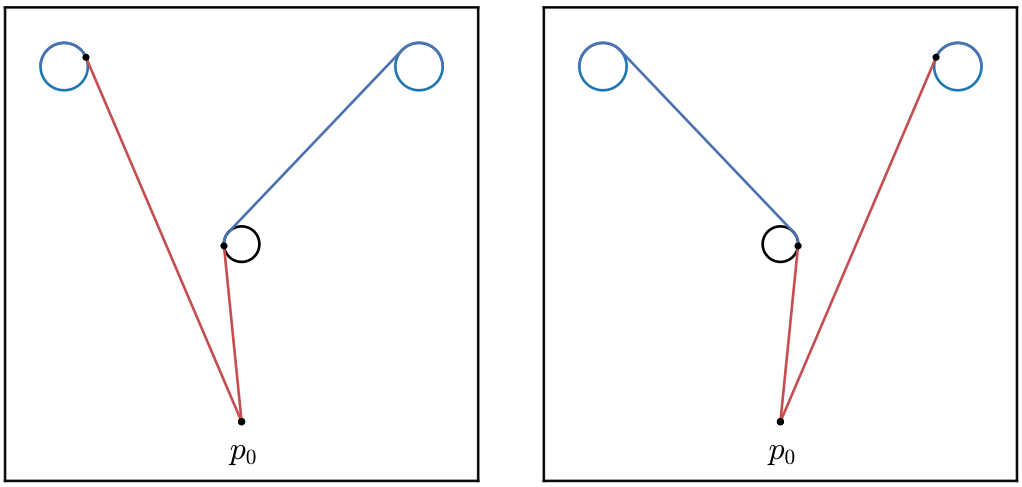

(a) (b)

Figure 5.1: Multiple possible configurations for a given end effector position.

such a collection of charts can be constructed, starting with the case of a point-mass end effector. In Section 5.2 the necessary extensions required for VSCRs based on rigid platforms are provided.

5.1.1 Chart Construction

This section discusses how charts can be represented and systematically constructed from a given VSCR structure. Each structure is represented using the following form:

$$S = \{s_1, s_2, \ldots, s_n\} \tag{5.1}$$

where each element s_i of structure S corresponds to the state of the ith cable and takes the form of a sequence of segments, as described in Chapter 4. Each chart can be represented as a collection of four elements:

$$C = \{\boldsymbol{l}_0,\ \boldsymbol{\nu}(\boldsymbol{p}),\ \boldsymbol{A}(\boldsymbol{p}),\ \mathcal{Q}\} \tag{5.2}$$

where $\boldsymbol{l}_0$ contains the initial cable lengths, as discussed in Section 4.3; $\boldsymbol{\nu}(\boldsymbol{p})$ provides the active wrapping-segment lengths; and $\boldsymbol{A}(\boldsymbol{p})$ produces the fixed-frame anchor point locations. $\boldsymbol{l}_0$, $\boldsymbol{\nu}(\boldsymbol{p})$, and $\boldsymbol{A}(\boldsymbol{p})$ are all generally defined as

$$\boldsymbol{l}_0 = \begin{bmatrix} l_{0,1} & l_{0,2} & \cdots & l_{0,n} \end{bmatrix}^T \tag{5.3}$$

$$\boldsymbol{\nu}(\boldsymbol{p}) = \begin{bmatrix} \nu_1(\boldsymbol{p}) & \nu_2(\boldsymbol{p}) & \cdots & \nu_n(\boldsymbol{p}) \end{bmatrix}^T \tag{5.4}$$

$$\boldsymbol{A}(\boldsymbol{p}) = \begin{bmatrix} \boldsymbol{a}_1(\boldsymbol{p}) & \boldsymbol{a}_2(\boldsymbol{p}) & \cdots & \boldsymbol{a}_n(\boldsymbol{p}) \end{bmatrix} \tag{5.5}$$

$\mathcal{Q}$ is the set of end-effector positions within which chart C is valid. $\boldsymbol{\nu}(\boldsymbol{p})$ and $\boldsymbol{A}(\boldsymbol{p})$ must both be continuous within the domain of $\mathcal{Q}$.

Given a structure S, its corresponding chart, C^S, can be constructed by determining each of its four elements. $\nu_i(\boldsymbol{p})$ and $\boldsymbol{a}_i(\boldsymbol{p})$ are found directly from the final element of s_i using knowledge of the exit pulley geometry; $l_{0,i}$ is found as the summation of the lengths of all static segments contained in s_i. In order to determine $\mathcal{Q}^S$, the area where the end effector can be located under structural configuration S without resulting in any collisions or structural changes (away from S) is first identified. This set of points is referred to as the 'structure-reachable area' (SRA). A change in structure occurs when any of the n cables experiences a collision or separation. With this in mind, the 'cable-reachable area' (CRA) for a given cable is defined as the set of points that can be reached by the platform end of a cable without requiring a change in the cable's state, or resulting in any non-permissible collisions (see Fig. 5.2b and Fig. 5.2c). A point belongs in the SRA iff it is included in the CRA for each of the n cables. Thus, the SRA for a given structure S can be obtained as

$$\mathrm{SRA}^S = \bigcap_{i=1}^{n} \mathrm{CRA}^{s_i} \tag{5.6}$$

By representing the CRAs as polygons, the intersection required for solving

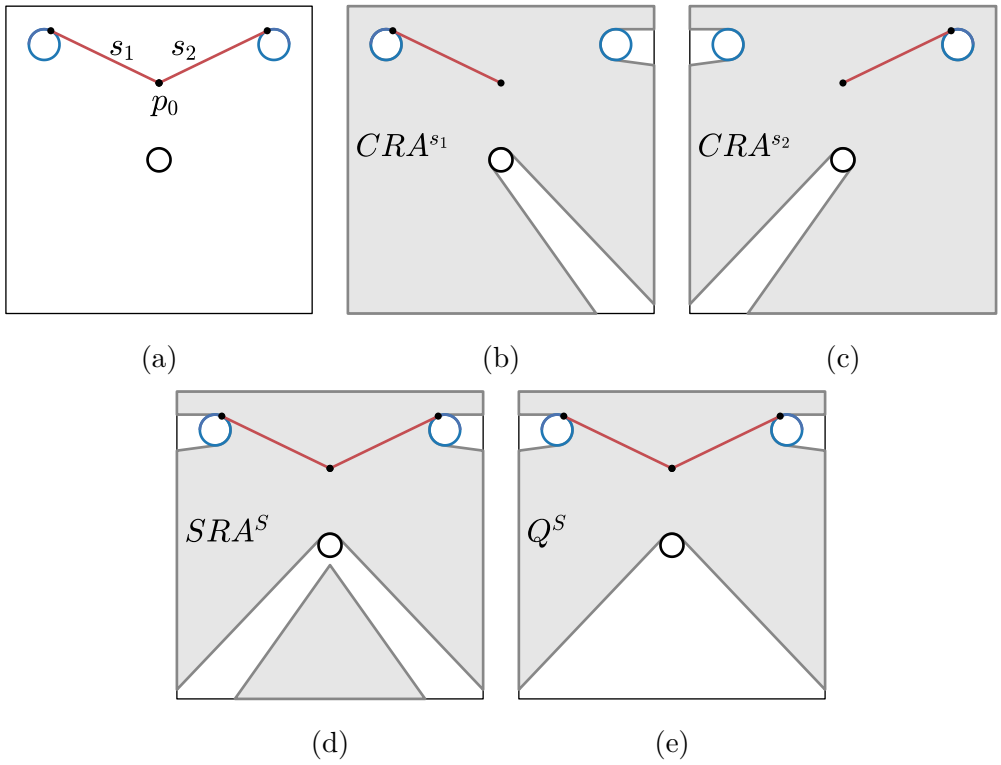

Figure 5.2: Elements involved in chart construction for a PM VSCR: initial condition shown in (a); the areas corresponding to the terms labeled in (b)–(e) are shown in gray.

Eq. (5.6) can be performed using the methods shown in [74] or [75]. How the CRAs can be determined is the subject of Section 5.1.2.

The SRA generally consists of a number of disjoint components (see Fig. 5.2d), only one of which may be included in the C-space: inclusion of multiple components would require cutting and reattaching one or more cables during a motion. If an initial point $\boldsymbol{p}_0$ is given that is known to be within $\mathcal{Q}^S$, then $\mathcal{Q}^S$ can be found as the component of SRA^S that contains $\boldsymbol{p}_0$ (see Fig. 5.2e). The component that contains $\boldsymbol{p}_0$ can be found using any standard 'point-in-polygon' test, such as [76].

5.1.2 CRA Determination

The problem of finding the CRA is analogous to the problem of finding the visiblity polygon from a point: much like a ray of light, the path of a cable segment between its two end points takes the form of a straight line that must be unobstructed for the given end-point location to be reachable. This section introduces an algorithm for computing the CRA for a given cable configuration. The algorithm is based on the algorithm presented in [77] and restated in [78] for determining the visibility polygon from a single point in the presence of holes. The algorithm of [77] has been adapted and extended for some of the specific technical features of cables. In the original algorithm, the visibility polygon is built from a single point; this has been modified to be from the perspective of a cable wrapping around a circle of non-zero radius. Additionally, the handling of circular holes and arcs in the resulting surface has been added. Another extension is the ability to handle multiple collinear vertices.

The algorithm consists of two phases: a setup phase and a scan phase. During the setup phase, the complete set of vertices and edges representing collidable boundaries are identified and converted to a directed-graph-based representation (with vertices becoming nodes). During the second phase, an angular sweep is performed where a scan line, extending from and tangent to the cable exit pulley, steps through the set of vertices based on their required wrap angle, identifying the boundaries of the CRA as it goes. Each phase is described in detail below with the assistance of Fig. 5.3, which shows visually the working of the algorithm.

Initial Setup

Several features restrict a cable's reachability: the installation-space boundary, obstacles, pulleys, and the cable's static segments. The collidable boundaries for each of these features must be included when creating the graph-based representation of the environment. Each feature has its own unique

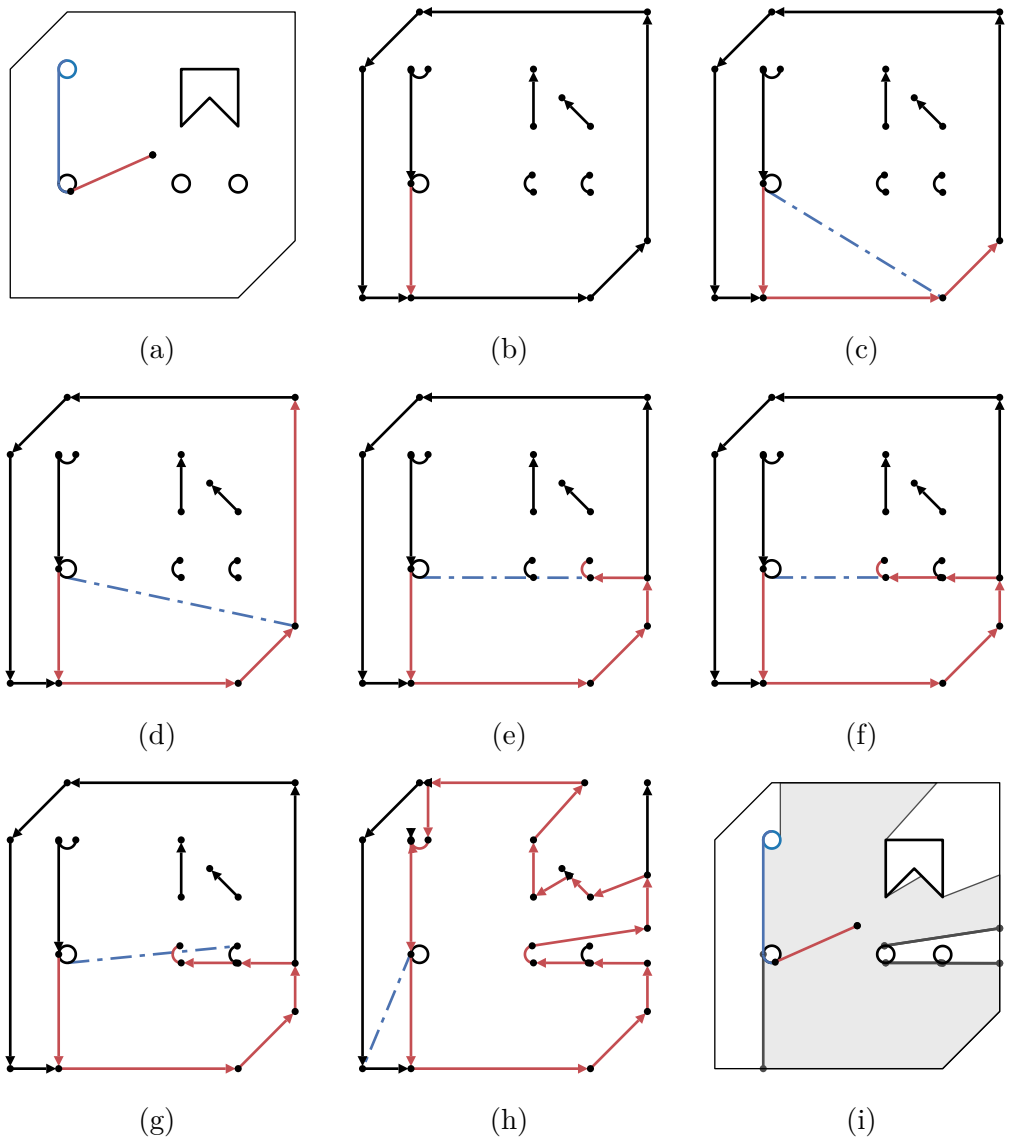

Figure 5.3: Visual demonstration of the CRA determination algorithm for the cable configuration shown in (a): scan line shown in blue; CRA boundary edges shown in red, (b-h); gray region in (i) is the identified CRA; dark gray edges in (i) are traversable.

considerations:

- The installation-space boundary and rigid obstacles are represented as polygons and stored as lists of vertices, ordered such that any two adjacent vertices have an edge between them, as do the first and last vertices in the list. Prior to inclusion, the orientation of the vertices (CW/CCW) should be adjusted to match the wrap direction of the cable around its exit pulley. It is only necessary to include edges where the required wrap angle to reach the destination vertex exceeds the required wrap angle to reach the origin vertex. This condition is met for every edge in a convex polygon. For non-convex polygons, edges that violate the above condition are guaranteed to be unreachable and, therefore, discarded.

- Each pulley can be represented as a single arc-shaped edge (of matching radius) whose end points correspond to the two wrap-direction-consistent common tangents between the cable exit pulley and the pulley in question.

- Each of the cable's static segments, if present, are included based on their known end points. Since the static segments are always tangent to pulleys on both ends, it is often the case that a static-segment edge intersects with one or more pulley arc edges. In such cases, the arc edges should be bisected at the point of intersection.

An example of a given cable configuration (embedded within a known environment) and its corresponding graph can be seen in Fig. 5.3a and Fig. 5.3b respectively.

Once the initial graph has been constructed, the next step is to organize the vertices into a sorted list of lists based on the cable wrap angles (denoted as ϕ) required to reach each vertex (denoted as v). A list containing all vertices of a common angle is created for each unique required wrap angle.

The primary list is denoted as V and defined as

$$V = \{\{\phi_1, \{v_{1,1} \cdots\}\}, \{\phi_2, \{v_{2,1} \cdots\}\}, \cdots, \{\phi_g, \{v_{g,1}, \cdots\}\}\} \tag{5.7}$$

where the elements are sorted such that $\phi_i < \phi_k$ for all $i < k$. g corresponds to the number of distinct required wrap angles. The length of each list of vertices is variable and represented as $h(\phi)$.

After the vertices have been sorted, the next step is to initialize the scan line and create an initial list of active edges (edges that the scan line intersects with). If the list of static segments in the cable configuration is non-empty (i.e. the cable can separate from its current exit pulley), an edge must also be included in the graph that deals with the unwrapping condition. This edge can be created while simultaneously building the initial list of active edges as follows: extend a ray from the exit pulley in the direction of a zero wrap angle; all edges that intersect with this ray are included in the initial list of active edges; the extended ray is then converted to an edge by taking its terminating point as the point of intersection with the nearest active edge (see Fig. 5.3b). If the list of static segments is empty, ϕ_1 in V is chosen as the initial wrap angle, and the extending ray is not included in the graph.

Angular Sweep

At any given wrap angle, the edge nearest to the exit pulley along the scan line is a part of the CRA boundary. Thus, by tracking which edge is nearest while scanning through the list of vertices, in order of increasing wrap angle, the entire CRA boundary can be constructed edge by edge. Between vertices, the nearest active edge (NAE) remains constant; once the scan line crosses a vertex, the list of active edges must be updated as follows:

- If the vertex has no exiting edges, all entering edges are removed.
- If the vertex has no entering edges, all exiting edges are added.

- If the vertex has one entering edge and one exiting edge, the entering edge is replaced with the exiting edge.

If after updating the list of active edges there is a change in the NAE, the previous nearest edge (PNE) should be added to the list of CRA boundary edges, along with a new edge created between the PNE and the new NAE, as shown in Figs. 5.3c to 5.3g. If the PNE is collidable and no longer active or if the new NAE is collidable and just added, the newly created edge induces a cable state transition upon traversal (traversable edges are highlighted in Fig. 5.3i). The information regarding the cable state that would be transitioned to is appended as additional information to the corresponding edge. This information becomes important when chart building for identifying overlapping charts. After scanning through the entire set of vertices (Fig. 5.3h), The accumulated list of CRA boundary edges forms a closed region that is extracted and used as the CRA representation (Fig. 5.3i).

One special case that may occur when completing the scan is when multiple vertices have the same required wrap angle (see Figs. 5.3d to 5.3f). This case results in multiple collinear edges on the CRA boundary that may lead to different cable configurations upon traversal and, thus, must be kept separate. In order to deal with these cases, the collinear vertices are sorted in a particular way, and then the scan process continues as normal. First, the vertices are divided into two groups: the first group consists of vertices nearer than the PNE, and the second group consists of vertices farther than the PNE. The two groups are sorted independently and then recombined with the near vertices followed by the far vertices. Both groups are sorted based on their distance from the start of the scan line, with the near vertices sorted in ascending order and the far vertices sorted in descending order. The vertices are then scanned through one at a time in the order that they appear.

5.1.3 Structure Atlas

As was shown in Section 5.1.1, if a VSCR structure and an initial end-effector position are given, its associated chart can be constructed. What remains is to provide a way to systematically identify the set of all structures reachable for a given VSCR. This task can be achieved while simultaneously building a graph-based representation of the configuration space, referred to as the 'structure atlas' (SA). By organizing the set of charts into the form of a graph, it allows chart adjacency to be encoded (i.e., how charts overlap and which pairs of charts allow uninterrupted end-effector motion). The benefits of the SA will be further explored in Section 5.3.

While constructing the SA, each node is associated with a chart, and edges between nodes are formed based on chart adjacency. For any VSCR, it is generally not the case that all possible structural configurations are reachable; in order for a structure to be reachable, its corresponding chart must overlap with another chart that is also reachable. The sole exception to this rule is the trivial case of a constant-structure CDPR, where only one chart is required.

Adjacent charts overlap only along rays extended from potential points of collision (or separation): where the anchor point for the colliding cable becomes ambiguous. With this in mind, the set of structures adjacent to a given chart can be identified by analyzing the information stored in the edges of the chart boundaries. Continuing this process repeatedly, eventually, the entire SA can be built; however, an initial sample configuration must be provided from which a first node is created. The complete construction process is demonstrated in an implementable way using Algorithm 5.1. Figure 5.4 provides a visual representation of the atlas that can be built for the VSCR shown in Fig. 5.2 based on its demonstrated initial configuration.

Algorithm 5.1: Identify reachable structures and construct the structure atlas from an initial configuration.

Function *BuildSA*(S_0,$\boldsymbol{p}_0$)
- $\mathcal{S} \leftarrow \{S_0\}$
- $C^{S_0} \leftarrow$ new chart built from S_0 and $\boldsymbol{p}_0$
- Add C^{S_0} to new atlas SA
- Push C^{S_0} onto Stack
- **while** *Stack is not empty* **do**
  - Pop C_1 off of Stack
  - **foreach** *edge* $e \in C_1.\mathcal{Q}$ **do**
    - **if** $e.S \notin \mathcal{S}$ **then**
      - $\mathcal{S} \leftarrow \mathcal{S} \cup \{e.S\}$
      - $\boldsymbol{p}_{\text{mid}} \leftarrow (e.\boldsymbol{p}_1 + e.\boldsymbol{p}_2)/2$
      - $C_2 \leftarrow$ new chart from $e.S$ and $\boldsymbol{p}_{\text{mid}}$
      - Add C_2 to SA
      - Push C_2 onto Stack
    - **else**
      - Find chart $C^{e.S}$ in SA and assign to C_2
    - **end**
    - Add edge between C_1 and C_2 in SA
  - **end**
- **end**
- **return** $\mathcal{S}$, SA

end

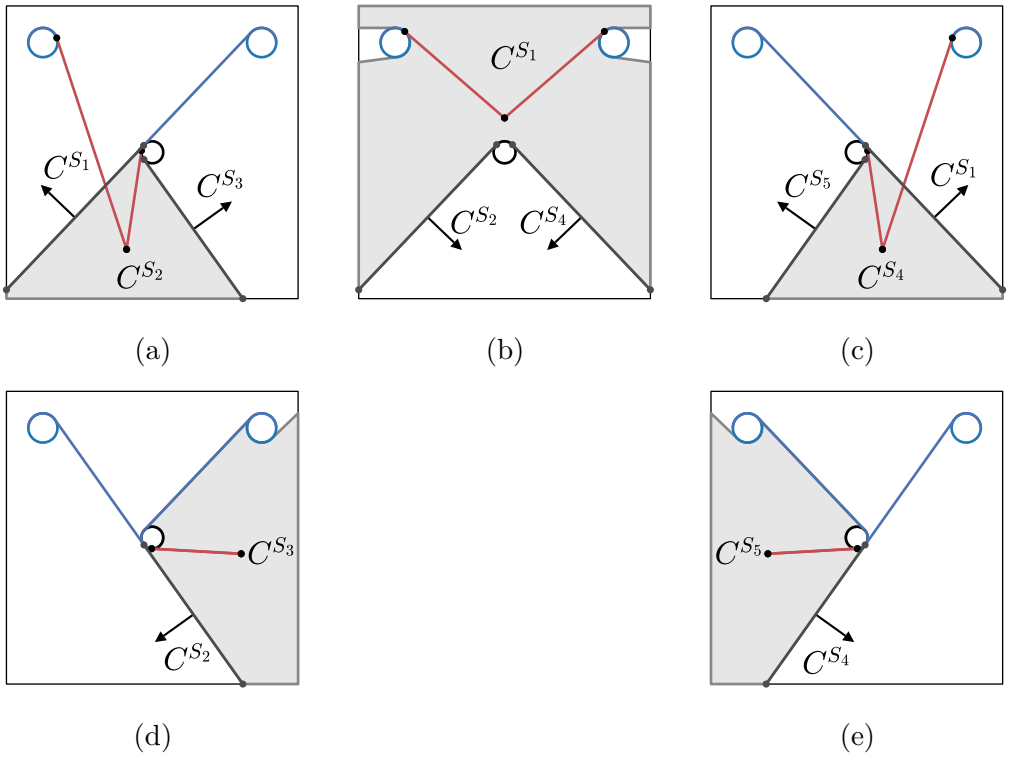

Figure 5.4: Structure Atlas for the VSCR shown in Fig. 5.2. Gray regions correspond to the labeled chart's domain; arrows highlight edges leading to the labeled adjacent chart upon traversal.

5.2 Rigid-Body Extensions

In order to generalize the results of Section 5.1 beyond the assumption of a point-mass end effector, there are certain modifications and extensions that must be considered. The primary change is required during chart construction, where the SRA must be limited to only include points that can be reached without resulting in any collisions between the platform and cables or between the platform and other rigid structures (such as pulleys). For this purpose, the 'platform-reachable area' (PRA) is defined as the set of end-effector positions with a given constant orientation that can be reached without resulting in any platform collisions. A method for how the PRA can be determined will be presented in Section 5.2.1. Further details regarding the necessary changes required during chart construction and extending the SA concept to consider changes in platform orientation will be discussed in Section 5.2.2.

5.2.1 PRA Determination

Before embarking into the PRA determination process, some definitions must first be declared: first, a set M^θ is defined that contains the points occupied by the platform when positioned at the ground-frame origin with an orientation angle θ; second, for each fixed rigid object in the environment (including pulleys), a set P_i is defined that consists of the points occupied by the ith object; finally, $\mathcal{I}$ is defined as a set that contains all points in the installation space.

Several different elements restrict where the platform can be located in the installation space, each of which must be considered separately. The elements considered are collisions between the platform and fixed rigid objects, the installation space boundary, the cables' static segments, and the cables' active segments. for any fixed object, the area where the platform and the object overlap is found as the Minkowski sum between the object's point set

P and $-M^\theta$ where $-M^\theta$ is defined as

$$-M^\theta = \left\{-\boldsymbol{m} \,|\, \boldsymbol{m} \in M^\theta\right\} \tag{5.8}$$

The Minkowski sum operation is defined as follows: given two sets $A, B \subset \mathbb{R}^2$, their Minkowski sum is

$$A \oplus B = \{\boldsymbol{a} + \boldsymbol{b} \,|\, \boldsymbol{a} \in A, \boldsymbol{b} \in B\} \tag{5.9}$$

The boundary of $P \oplus (-M^\theta)$ can be seen as the traced result of dragging the platform around the object's surface. This process is demonstrated in Fig. 5.5 for both a pulley and a line-segment and can be computed algorithmically using the methods provided in [79] and [80]. Applying this process to all collidable objects and taking the union of the individual results, a set H^θ_{obj} can be found, which is defined to be the set of all end-effector positions that result in a collision between the platform and at least one object:

$$H^\theta_{\text{obj}} = \bigcup_{i=1}^{k} \left(P_i \oplus (-M^\theta)\right) \tag{5.10}$$

where k is the total number of objects. Taking a similar approach, the set of end-effector positions that result in a collision between the platform and the installation-space boundary (H^θ_{border}) can be determined as

$$H^\theta_{\text{border}} = \bigcup_{i=1}^{v} \left(\mathcal{I}_i \oplus (-M^\theta)\right) \tag{5.11}$$

where $\mathcal{I}_i$ denotes the ith edge of the installation-space boundary and v is the number of boundary edges. The locations where the platform collides with any of the static segments for all cables ($H^{S,\theta}_{\text{static}}$) can be found by taking the union of the individual buffers formed around the linear portion of each static segment. If m_i is used to denote the number of static segments for

the ith cable and $s_{i,j}$ to denote the jth segment of the ith cable, $H^{S,\theta}_{\text{static}}$ is obtained as

$$H^{S,\theta}_{\text{static}} = \bigcup_{i=1}^{n} \bigcup_{j=1}^{m_i} \left(s_{i,j} \oplus (-M^{\theta}) \right) \tag{5.12}$$

Determining the regions that result in a collision with the active segments requires a different approach since the active segment locations are platform-position dependent. It is first observed that there is a minimum and a maximum wrap angle that can be achieved before the active segment collides with the platform body. In order to determine the region where the platform and the active segment overlap for a given cable, the minimum and maximum allowable wrap angles are determined first, which occur when the active segment is tangent to the platform edges adjacent to the respective platform-fixed anchor-point (see Fig. 5.6b). A ray is then extended outwards at the two wrap angle extremes, parallel to the active segment and shifted to be in terms of the end-effector position by removing the cable-anchor offset. The rays are extended until they intercept with the installation-space boundary. By taking the subsection of the installation-space boundary contained between the two rays and adding an edge between the origins of the two rays, a closed region can be obtained that contains the set of locations where the platform and active segment overlap, denoted as $H^{s_i,\theta}_{\text{active}}$. This process is illustrated in Fig. 5.6. The regions $H^{s_i,\theta}_{\text{active}}$ for all cables are combined into a single term $H^{S,\theta}_{\text{active}}$ by taking the union of the individual results obtained for each of the n cables:

$$H^{S,\theta}_{\text{active}} = \bigcup_{i=1}^{n} H^{s_i,\theta}_{\text{active}} \tag{5.13}$$

Combining the results of Eqs. (5.10) to (5.13) gives the entire set of points that are not platform reachable. The PRA can then be determined by subtracting this area from the installation-space:

$$\text{PRA}^{S,\theta} = \mathcal{I} \setminus \left(H^{\theta}_{\text{obj}} \cup H^{\theta}_{\text{border}} \cup H^{S,\theta}_{\text{static}} \cup H^{S,\theta}_{\text{active}} \right) \tag{5.14}$$

A graphical example of the PRA computation process, including the various components of Eq. (5.14) is provided in Fig. 5.7.

5.2.2 SA and Chart Modifications

In order to account for the effect of the platform-fixed cable anchor offsets on the CRAs, and to integrate the limitations imposed by the PRA, Eq. (5.6) must be revised as follows:

$$\mathrm{SRA}^{S,\theta} = \left(\bigcap_{i=1}^{n} (\mathrm{CRA}^{s_i} - \boldsymbol{R}(\theta)\boldsymbol{b}_i) \right) \cap \mathrm{PRA}^{S,\theta} \tag{5.15}$$

The rest of the approach to chart construction presented in Section 5.1.1 remains the same. An example of the chart construction process for a VSCR with a rigid platform is provided in Fig. 5.8. It is important to note that Eq. (5.15) is orientation dependent. Because of this dependency, the SA as described in Section 5.1.3 must be built under the assumption of constant orientation. The true shape of the complete SRA and domain $\mathcal{Q}$ for a given structure takes the form of a 3-D helical volume (with the axes being the 3-components of the platform pose); however, their geometry is too complex to derive an explicit representation. Instead, the 3-D volume can be discretized into slices of constant orientation. Thus, the complete SA for a 3-DOF VSCR can take the form of a collection of sub-atlases (or 'pages'), where one sub-atlas is built for each slice of constant orientation.

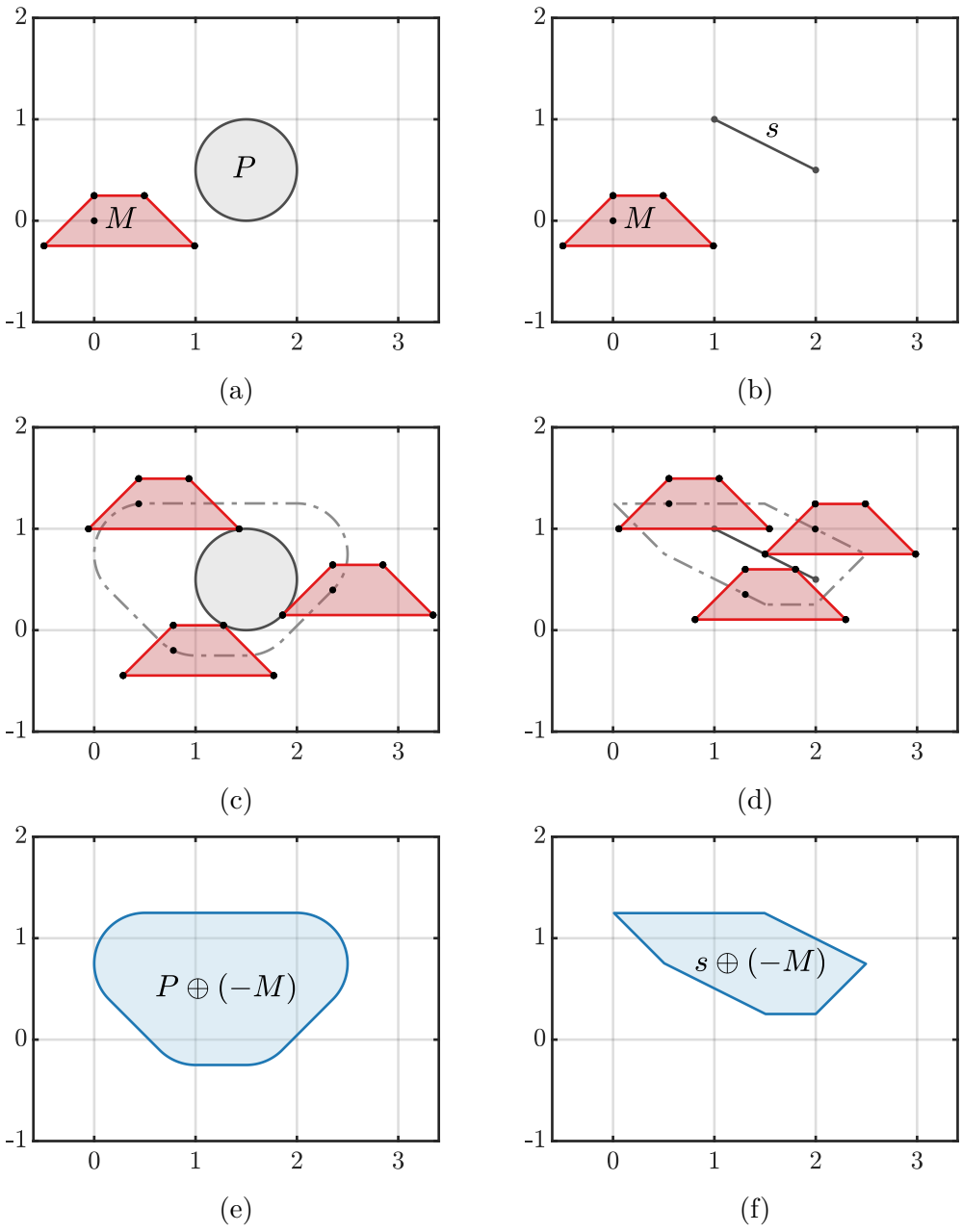

Figure 5.5: Application of the Minkowski sum to collision detection: (e) shows the region where platform M collides with pulley P; (f) shows the region where platform M collides with line-segment s.

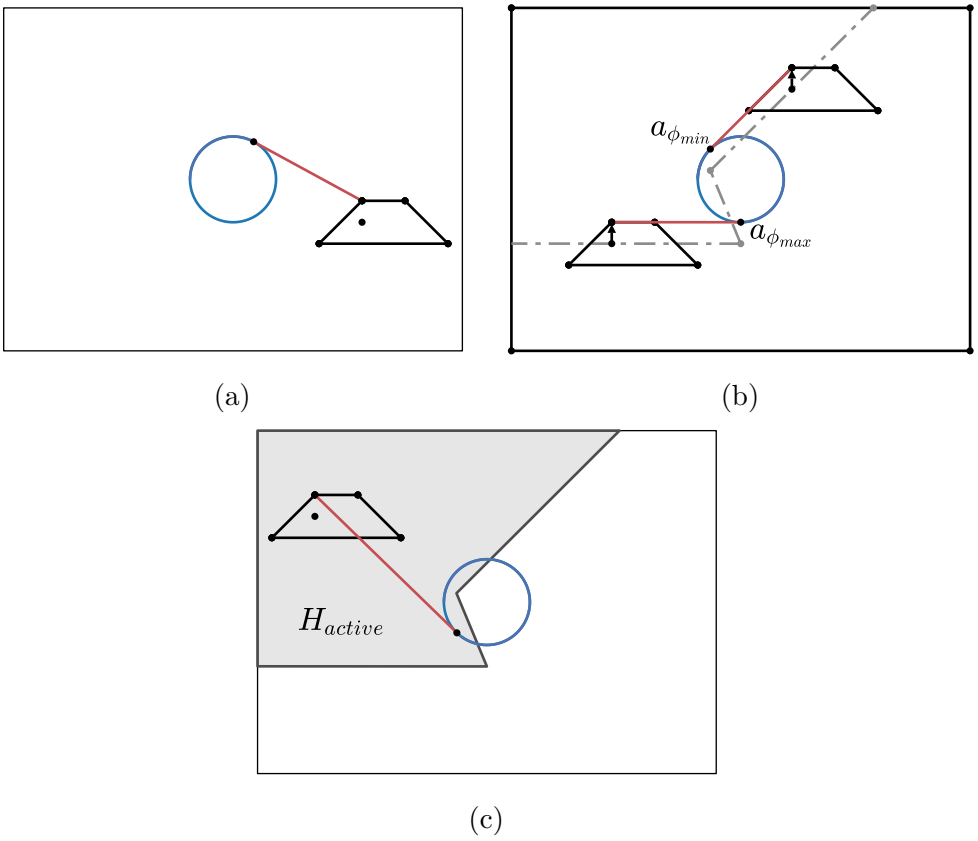

Figure 5.6: Determination of H_{active} for the single cable system shown in (a). Wrap angle limits before collision shown in (b). Locations where platform and cable active segment overlap (H_{active}) shown in gray in (c).

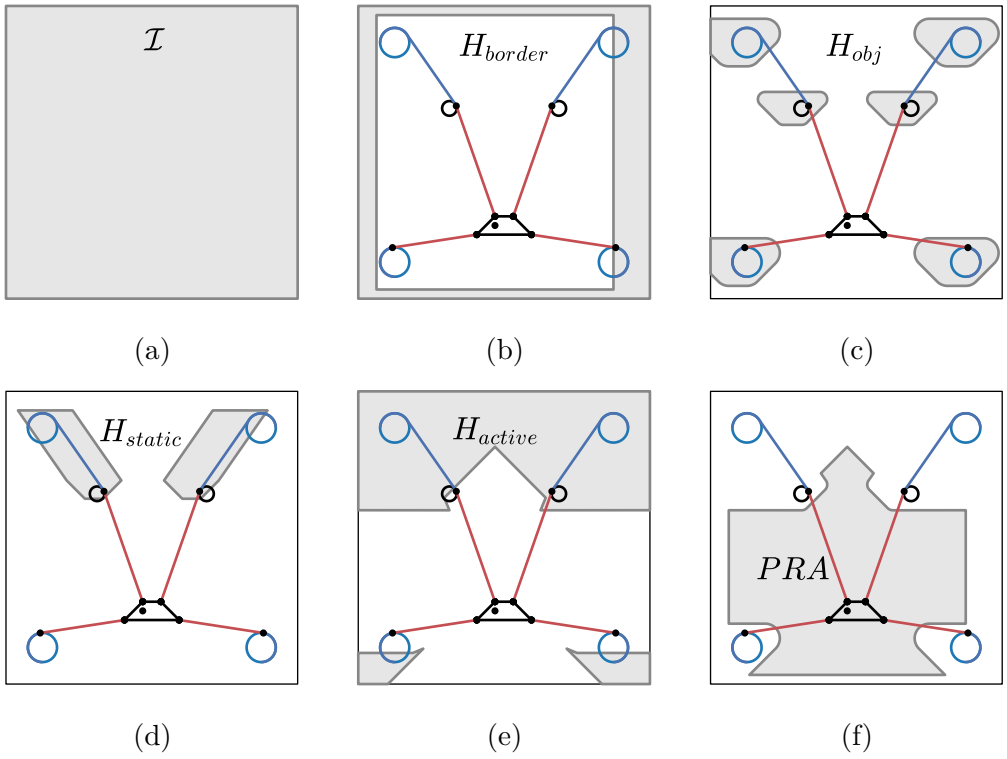

Figure 5.7: Elements involved in PRA computation, as discussed in Section 5.2.1. Areas corresponding to the terms labeled in (b)–(f) for the given VSCR configuration are shown in gray.

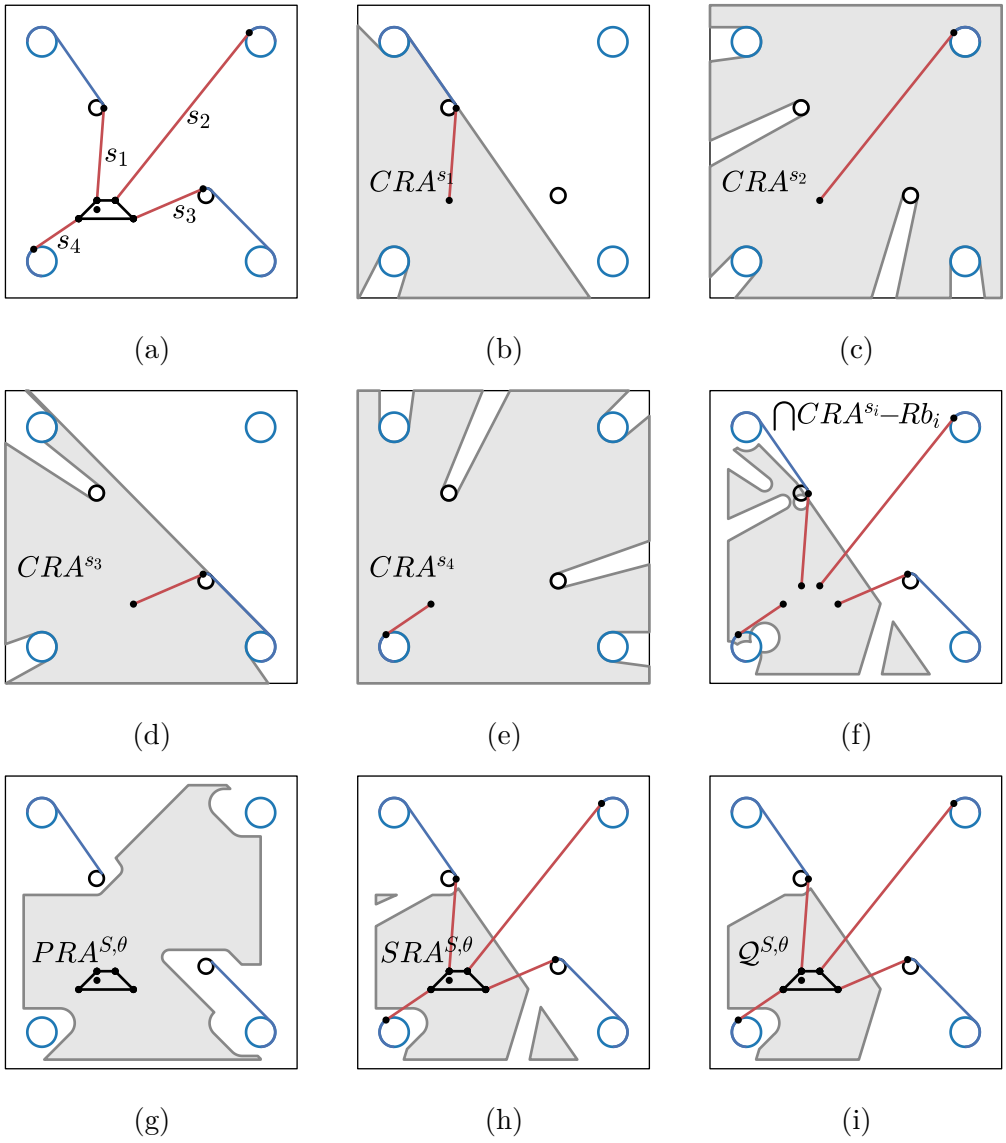

Figure 5.8: Elements involved in chart construction for a rigid-platform-based VSCR: initial condition shown in (a); areas corresponding to the terms labeled in (b)–(i) shown in gray.

5.3 Structure-Atlas Applications

The value of the SA comes not from its ability to be constructed but from its ability to serve as a powerful tool for VSCR analysis. In the proceeding subsections, it is demonstrated how the SA can be applied to both workspace analysis and inverse kinematics.

5.3.1 Workspace Analysis

Here an SA-based method for VSCR workspace determination is presented. The term workspace here refers to a connected set of end-effector poses that are both reachable and feasible. For a VSCR, there may be multiple possible workspaces that can be achieved, depending on the initial cable-routing; however, the end effector can only navigate through a single workspace without requiring one or more cables to be disconnected, and reattached [69]. A point is considered reachable if it is kinematically feasible and if a connected path of reachable points exists between the point in question and a given initial configuration. The determination of point reachability was a part of the focus of Section 5.1: any point in any chart of the SA is reachable.

Point feasibility requires that a set of constraints on the platform dynamics be met, namely in relation to cable tension distribution and ability to maintain a static equilibrium for the following expression:

$$\boldsymbol{W}(\boldsymbol{p},\theta)\boldsymbol{\tau} = \boldsymbol{w}_{ext} \tag{5.16}$$

where $\boldsymbol{w}_{ext}$ represents a given externally applied wrench. $\boldsymbol{W}(\boldsymbol{p},\theta)$ and $\boldsymbol{\tau}$ are the wrench matrix and vector of cable tensions, respectively, as defined in Section 2.1.1. Various conditions exist within the CDPR literature for point feasibility, the most common of which being wrench-closure (cables must be able to balance any externally applied wrench while maintaining positive tensions [34]) and wrench-feasible (cables must be able to balance a

limited set of external wrenches while satisfying bounds on the cable tensions [30]). Regardless of chosen definition for point feasibility, once the SA is constructed, a VSCR's workspace can be represented as a collection of sub-workspaces: one for each reachable chart. Since a VSCR can be treated as an equivalent CDPR within the domain of each chart, standard techniques from the CDPR literature, such as those presented in [32] and [33], can be used for calculating the individual sub-workspaces.

It is not necessarily the case that all charts are dynamically reachable. For a chart to be included in the workspace, it must share at least one feasible point with an adjacent chart that is also reachable; the one exception to this rule is the initial chart which is known to be reachable. Once the entire workspace is determined, any charts that are not reachable can be removed or pruned from the SA if desired. The complete workspace determination process is summarized in Alg. 5.2. As an example, the computation of the wrench-feasible workspace for a T-shaped VSCR is shown in Fig. 5.9. For the sake of simplicity, the chosen method of workspace determination was to discretize each chart area into a grid of points and test the feasibility of each point. A point is considered feasible if a stable distribution of tensions can be found without violating upper or lower bounds on the cable tensions. The point feasibility test was implemented using linear programming.

5.3.2 Inverse Kinematics

If the current chart occupied by a VSCR is known, the cable lengths can be determined using Eq. (4.9). Based on this observation, two new methods for solving the VSCR inverse kinematics problem are presented that will be described in the proceeding subsections.

Algorithm 5.2: Determine Workspace and Prune SA

```
Function DetermineWorkspace (SA, C_0)
    WS ← ∅
    X ← C_0
    while X is not empty do
        C ← X(1)
        if C is unvisited then
            SubWS ← CalculateSubWS(C)
            if SubWS = ∅ then
                Remove C from SA
            else
                WS ← WS ∪ SubWS
                foreach edge e ∈ C.Q do
                    if e ∩ SubWS ≠ ∅ then
                        Add adjacent chart to X
                    end
                end
                Mark C as visited
            end
        end
        Remove C from X
    end
    Remove any unvisited charts from SA
    return SA, WS
end
```

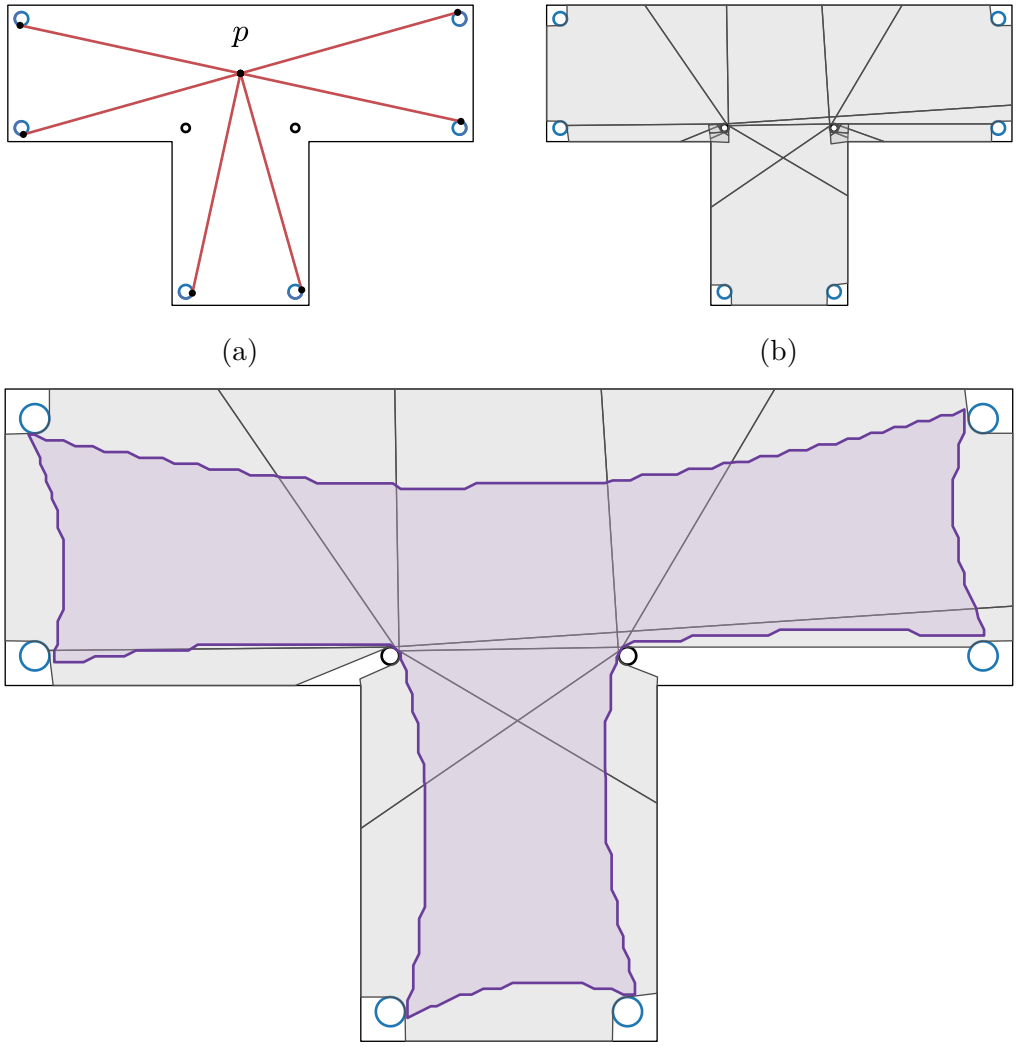

Figure 5.9: Demonstration of SA based workspace determination. Initial configuration shown in (a); complete set of charts in the resulting SA shown in gray in (b) with darker regions occurring where charts overlap; wrench-feasible workspace shown in purple in (c) with the pruned set of charts shown in gray.

Direct Method

Without requiring a known previous configuration, the cable lengths can be solved for directly at any point in the reachable workspace by first finding the list of charts that contain that point in their interior. The task of determining if a point is within the bounds of a given chart can be solved using any standard 'point-in-polygon' test, such as [76]. It is possible in some cases that there may be multiple solutions. Typically though, this approach results in a unique solution, especially if the search is limited to only charts which are a part of the workspace. The approach can be implemented using Alg. 5.3.

Algorithm 5.3: SA-Based Direct Inverse Kinematics

Function *DirectIK (SA, $\boldsymbol{p}$, θ)*
- `/* Find Active Chart */`
- **foreach** *chart* $C \in SA$ **do**
  - **if** $\boldsymbol{p} \in C.\mathcal{Q}$ **then**
    - `/* Active Chart Found */`
    - $\text{AC} \leftarrow C$
    - **break**
  - **end**
- **end**
- `/* Calculate Cable Lengths */`
- **foreach** $i \in \{1, \cdots, n\}$ **do**
  - $\boldsymbol{c}_i \leftarrow \text{AC}.\boldsymbol{a}_i(\boldsymbol{p}) - (\boldsymbol{p} + \boldsymbol{R}(\theta)\boldsymbol{b}_i)$
  - $l_i \leftarrow \text{AC}.l_{0,i} + \text{AC}.\nu_i(\boldsymbol{p}) + \|\boldsymbol{c}_i\|$
- **end**
- $\boldsymbol{l} \leftarrow \begin{bmatrix} l_1 & l_2 & \cdots & l_n \end{bmatrix}^T$
- **return** $\boldsymbol{l}$

end

Simplified Iterative Method

The problem addressed in this section is: given the previous chart, previous position, and current position, what is the current chart? Once the current chart is known, along with the current position, the current cable lengths can be determined by Eq. (4.9). Thus, in this section an iterative method for tracking the chart occupied by the end effector over time is introduced that can be used as a simplified approach for tracking cable lengths.

Given the end effector previous location ($\boldsymbol{p}_{t-1}$), current location ($\boldsymbol{p}_t$), and previous chart C_{t-1}, the current chart, C_t, can be determined using line-segment $\overline{\boldsymbol{p}_{t-1}\boldsymbol{p}_t}$ and the boundary of C_{t-1} as follows:

- If $\overline{\boldsymbol{p}_{t-1}\boldsymbol{p}_t}$ intersects with a transitionable edge of C_{t-1}, C_t is the adjacent chart associated with the intersected edge.
- Else if $\overline{\boldsymbol{p}_{t-1}\boldsymbol{p}_t}$ intersects with an edge of C_{t-1} that is not transitionable, the movement is invalid and $\boldsymbol{p}_t$ is unreachable
- Else $C_t = C_{t-1}$

This process is demonstrated graphically in Fig. 5.10 and summarized in Alg. 5.4.

Because of its relative simplicity for computation and implementation, this iterative approach is likely to be useful in a real-time setting and for structure-dependent control strategies; however, a requirement for this method is that the steps taken between control updates is small relative to the size of each chart.

Algorithm 5.4: SA-Based Iterative Inverse Kinematics: AC is the current active chart; $\boldsymbol{p}_1$ and $\boldsymbol{p}_2$ are the current position and new position respectively.

Function *IterativeIK(AC,* $\boldsymbol{p}_1$*,* $\boldsymbol{p}_2$*)*
  `/* Check for AC Border Crossings */`
  foreach *edge* $e \in AC.\mathcal{Q}$ **do**
    if *e and* $\overline{\boldsymbol{p}_1\boldsymbol{p}_2}$ *intercept* **then**
      AC $\leftarrow$ Adjacent Chart
      break
    end
  end
  `/* Calculate Cable Lengths */`
  foreach $i \in \{1, \cdots, n\}$ **do**
    $\boldsymbol{c}_i \leftarrow \text{AC}.\boldsymbol{a}_i(\boldsymbol{p}) - \boldsymbol{p}_2$
    $l_i \leftarrow \text{AC}.l_{0,i} + \text{AC}.\nu_i(\boldsymbol{p}) + \|\boldsymbol{c}_i\|$
  end
  $\boldsymbol{l} \leftarrow \begin{bmatrix} l_1 & l_2 & \cdots & l_n \end{bmatrix}^T$
  return AC, $\boldsymbol{l}$
end

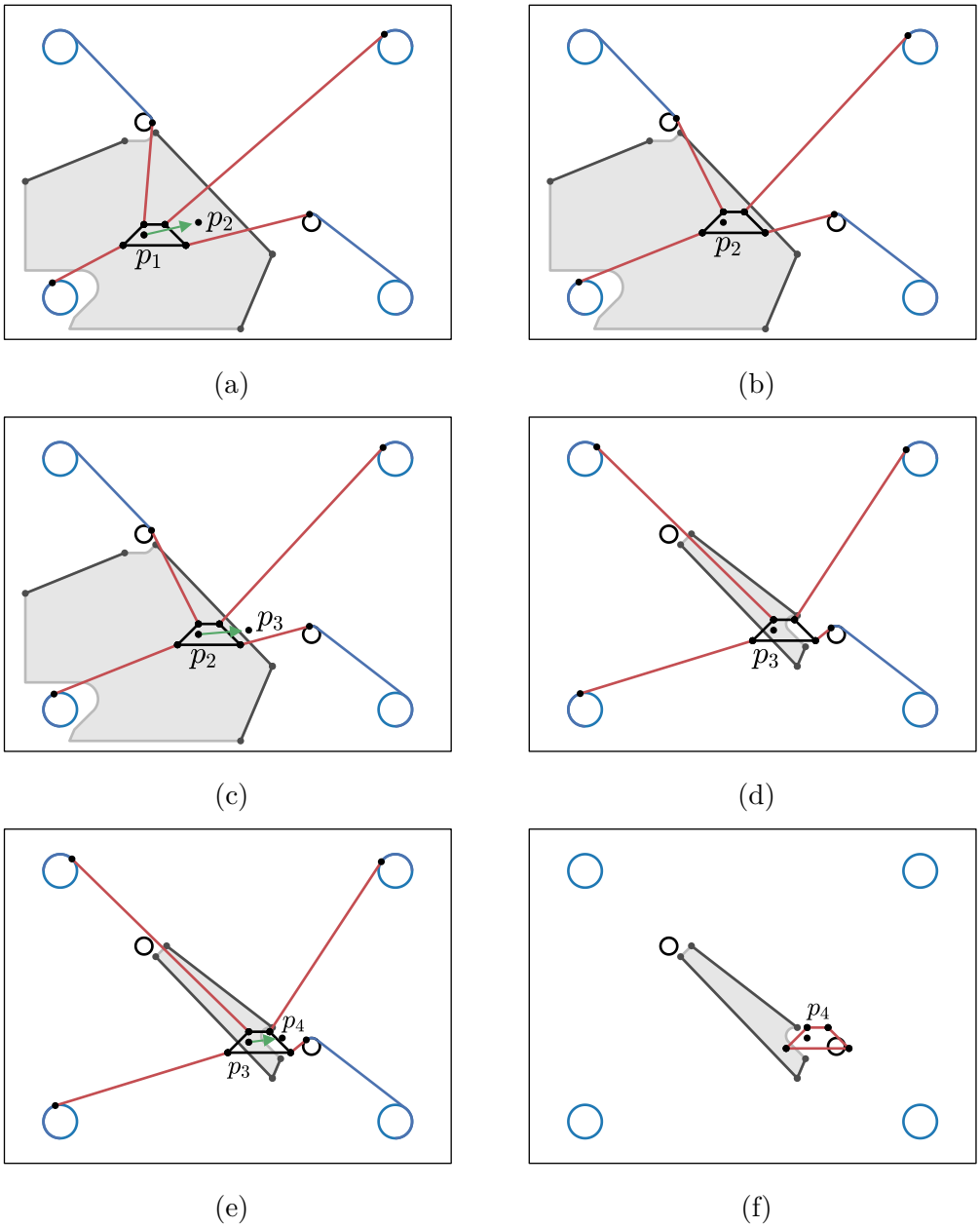

Figure 5.10: SA-based iterative inverse kinematics demonstration. (a)–(f) are sequential. (a), (c), and (e) show present and future EE positions while (b), (d), and (f) show the resulting active chart post movement. Active chart domains are shown in gray with transitionable edges shown in dark gray.

5.4 Summary

In this chapter, the concept of a 'structure atlas' (SA) has been introduced as a means of representing VSCR configuration spaces. A general and complete method has been provided that can be used for constructing the SA for any planar VSCR. Additionally, it has been demonstrated how the SA can be used to perform workspace analysis and directly solve the inverse kinematics problem.

Chapter 6

Implementation and Experimental Studies

In order to validate the results of the previous chapters and demonstrate the real-world feasibility of the proposed VSCR concept, several experimental studies have been performed using a purpose-built experimental testbed. This chapter summarizes and presents the findings from this work. The chapter is divided into the following sections: Section 6.1 describes the experimental testbed that was built for investigating VSCRs; Section 6.2 presents the results from the experimental studies that were performed; Section 6.3 discusses observations made during testing regarding the performance and limitations of the setup; Section 6.4 summarizes and concludes the chapter.

6.1 Experimental Testbed

This section presents the hardware and control details of the experimental testbed that was used for obtaining the results that will later be discussed in Sections 6.2 and 6.3.

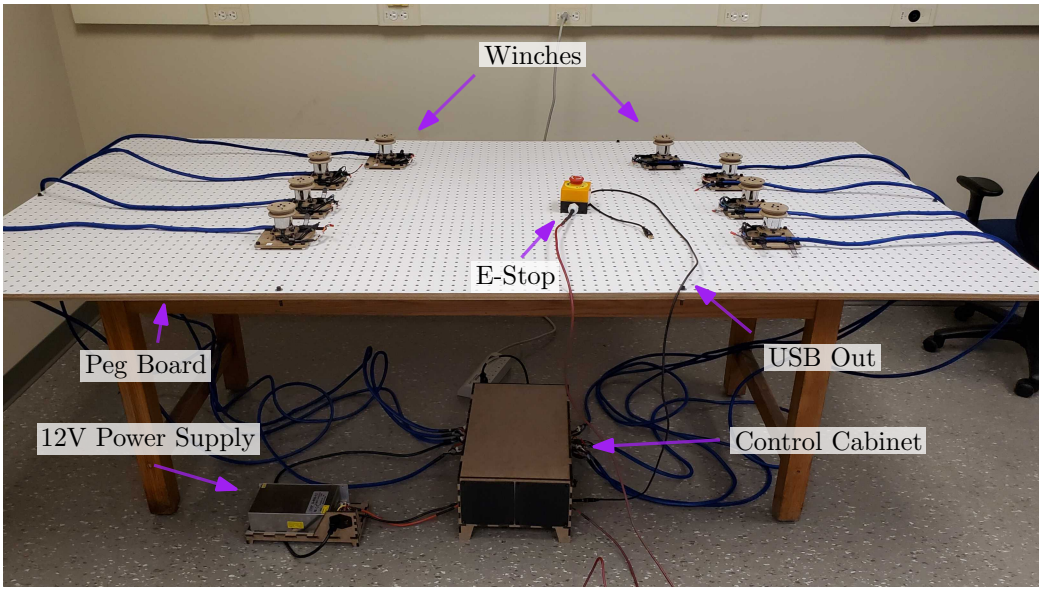

Figure 6.1: Experimental setup with main components labelled.

6.1.1 Hardware

The complete setup is shown in Fig. 6.1. The setup was designed to be highly flexible in order to grant a large amount of freedom in the types of scenarios that could be studied. In total, eight identical winches and three collidable idler pulleys were built with the control capability for all eight winches to be operated simultaneously. The winches and the idler pulleys were designed with a common mounting interface that matches the regular spacing of 1/4 inch pegboard, allowing for easy and rapid reconfiguration. Additional details specific to each of the main components are provided below.

Winches

A closeup view of a single winch with the relevant components labelled is shown in Fig. 6.2. Each winch contains a brushless DC motor (Turnigy 4250-350KV) directly coupled to a drive pulley. The drive pulleys are constructed out of laser-cut MDF and have a 50 mm inner diameter. An incremental en-

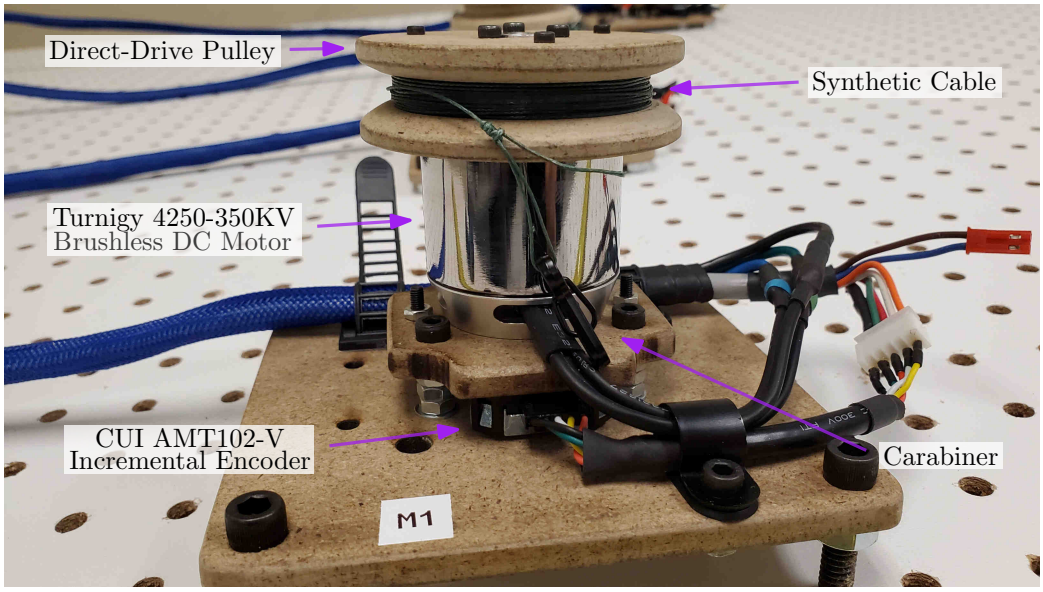

Figure 6.2: Winch closeup with components labelled.

coder (CUI AMT102-V) is attached to the secondary shaft on the backside of the motor for directly measuring the pulley rotation angle. Braided Spectra fishing line was used for the cables due to its high strength-to-weight ratio and low elasticity. The cable diameter is 0.5 mm with a rated load capacity of 89 N which well exceeds the torque capacity of the motors. A carabiner is attached at the end of each cable to allow for quick connection and disconnection, further facilitating rapid reconfiguration. The winches were initially designed to include a brake system for maintaining a fixed rotor position when not in operation; however, during testing, it was found that the internal cogging torque of the motor was sufficient to hold the rotor in place, and thus, the brake system was deemed unnecessary.

Idler Pulleys

In addition to the winches, a set of three collidable idler pulleys (shown in Fig. 6.3) were created. The idlers are identical to each other and have an

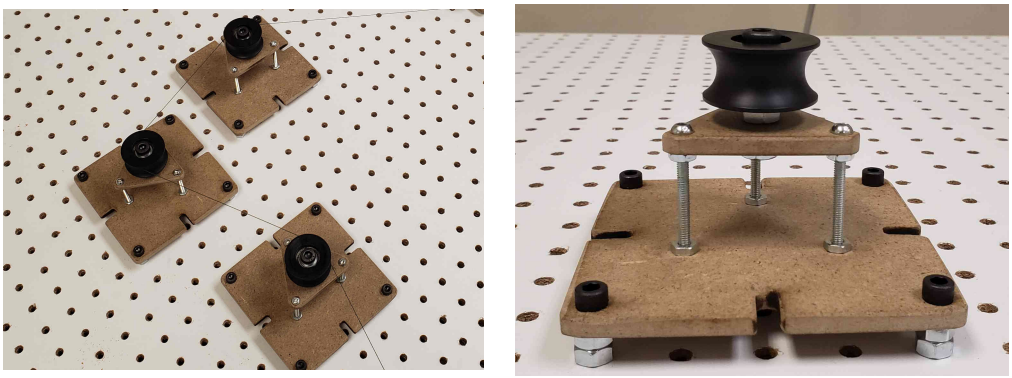

(a) (b)

Figure 6.3: Collidable idlers pulleys.

inner radius of 30 mm. The pulley width was made intentionally large relative to the cable thickness to allow for a greater margin of error in cable position while still ensuring reliable capture during a collision approach. Each idler has an internal bearing to allow free rotation and minimize friction between the pulley and the cables.

Control Cabinet

The interior of the control cabinet with all components labelled is shown in Fig. 6.4. The winches are controlled by four ODrive brushless DC motor controllers (where each is capable of driving two axes). The cabinet was designed to support interfacing with additional sensors or other components as needed. To this end, an Arduino Mega 2560 microcontroller board and a 4-channel MOSFET PWM signal amplifier were included. The four ODrives and Arduino are connected to a common USB hub where a single USB cable exits the cabinet for connection with an external PC. The entire cabinet is powered off of an external 12 V DC power supply with an internal 12 V–5 V DC converter for powering lower voltage components, such as the Arduino and cooling fans. For safety, a high current relay is used for cutting power to the motor controllers when triggered by an external e-stop button. Addition-

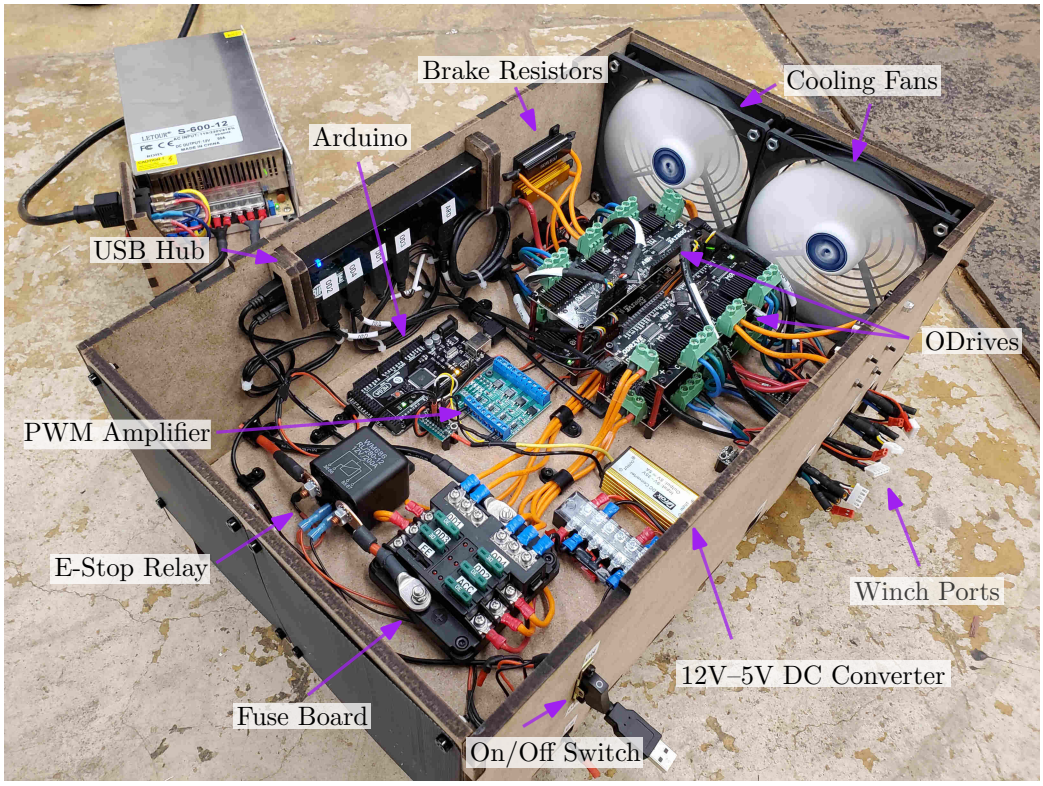

Figure 6.4: Control cabinet interior with components labeled.

ally, separate fuses lie in series between the supply current and the various components to protect against short circuits or excess current draw.

6.1.2 Control

The overall control strategy is based on an existing strategy for controlling traditional CDPRs: for an end effector with m DOF and n cables, where $n \geq m$, operate m cables in length control mode to kinematically constrain the platform, and operate the remaining $n-m$ cables in tension control mode in order to maintain positive tensions in all cables. For CDPRs in general, which cables are best assigned to position control and which are best assigned to tension control is still an open question; however, for VSCRs, there are

some notable restrictions that must be taken into consideration: if multiple cables have the same anchor points, one at most can be length controlled. This scenario can occur if multiple cables collide with the same object and connect to the same point on the end effector. Since there is always some amount of variation between the predicted and true cable lengths, each of the active segments will be slightly different lengths, resulting in all but the shortest cable becoming slack. This issue can be addressed by reassigning cable control modes as needed after a collision; however, for the scenarios tested, reassigning control modes was found to be unnecessary if well-chosen initial control mode selections were used.

Low-level winch control is performed using the ODrive motor controllers, which can be configured to operate in either position control or torque/current control modes. Cable tensions are estimated using the applied motor current in each winch. Since the torque generated in a motor is proportional to its current, and since the pulleys are direct drive (no gearbox), where friction losses should be minimal, it is assumed that the motor current can be used as a reasonable estimate of the corresponding cable tension. Cable lengths are estimated using the winch encoders. Since the encoders are incremental (rather than absolute), they must be calibrated each time the system is reset. The calibration was performed by manually moving the end effector to a known position, usually the start point of a trajectory, and then capturing the encoder offsets. A constant torque was applied to all active winches during the calibration procedure to keep the cables under tension. An external camera was used for tracking a red marker centred on the end effector to estimate the true path taken by the end effector. The camera information was not used for online feedback; it was used only for external validation. Post-processing of the video data was performed using the Computer Vision Toolbox within Matlab/Simulink.

When creating a motion profile, the desired end-effector trajectory was designed first and then converted to required cable lengths over time using

the inverse kinematics methods presented in Section 4.3 and Section 5.3.2. Linear programming was used at each point along the trajectory to find a valid tension distribution amongst the cables. The optimization was set up to minimize cable tensions while ensuring upper and lower tension limits were not violated. The complete trajectory generation process was performed using Matlab.

6.2 Experiments

In order to validate the theoretical results presented in the previous chapters, a number of experiments were performed using three distinct VSCR designs, created using the reconfigurable VSCR testbed described in Section 6.1. The experimental procedure was the same for all test cases and designed to be as follows: a desired end-effector trajectory was generated and then converted to cable length trajectories using the inverse kinematics approaches described in Sections 4.3 and 5.3.2; the winch controllers then tracked the generated cable length trajectories, and the actual path taken by the end effector was observed using the external vision system. The end-effector trajectories were based on a simple waypoint tracking system where the end effector moved through a sequence of locations, moving in a straight line between each point. Additionally, a 1 s dwell time was added between each waypoint where the end effector would sit stationary upon reaching its destination. The results from each scenario are presented in the proceeding subsections.

6.2.1 Agriculture

The VSCR demonstrated in this section is meant to simulate a vertical farming or greenhouse type application with adjacent rows of plants and empty spacing between rows. By adding a collidable idler pulley at the top of each row, the end effector is able to descend into the empty channels and perform tasks such as inspection or spraying without any interface between the

plants and the cables. More generally, this scenario demonstrates the ability of VSCRs to circumvent obstacles and interact with two opposing sides of an object without cable interference: a property that is valuable to a large number of applications and something that cannot be done using traditional CDPRs.

The configuration of the experimental setup is as shown in Fig. 6.5 and consists of two cables (c_1, c_2), operated in position control mode, two collidable idler pulleys (o_1, o_2), and a point-mass end effector $(\boldsymbol{p})$. The specific winch and idler mount locations are provided in Table 6.1. The shaded region in Fig. 6.5 illustrates the approximate workspace: a non-convex area with descending sections on each side of the vegetation. Areas outside the shaded region are protected from cable interference by the idler pulley placement.

Experimental observations were made using the waypoint sequence given in Table 6.2 (shown visually in Fig. 6.6), starting from the initial condition shown in Fig. 6.5. Figure 6.7 shows the robot configuration at various times along the trajectory. A recording of the entire motion can be found through the link provided in the footnotes[1]. Figures 6.8 to 6.11 present the desired and observed end-effector trajectories, end-effector tracking errors, cable lengths, and winch motor torques respectively. In Figs. 6.8, 6.10 and 6.11, black circular markers are used to highlight the occurrence of any CST node transitions experienced during the motion. Black vertical bars are used in Fig. 6.9 for the same purpose.

As the results demonstrate, the end effector was able to follow the desired path with a high degree of accuracy with no appreciable loss of performance observed during structural changes (which coincide with CST node transitions). Additionally, CST node transitions were not observed to cause any significant spikes or variations in the recorded motor torques. The presence of idler pulleys $o_{1\text{–}2}$ was found to be effective at preventing any collisions from occurring between the cables and the vegetation.

[1]Section 6.2.1 media extension: https://youtu.be/7N8DHFy3cDM

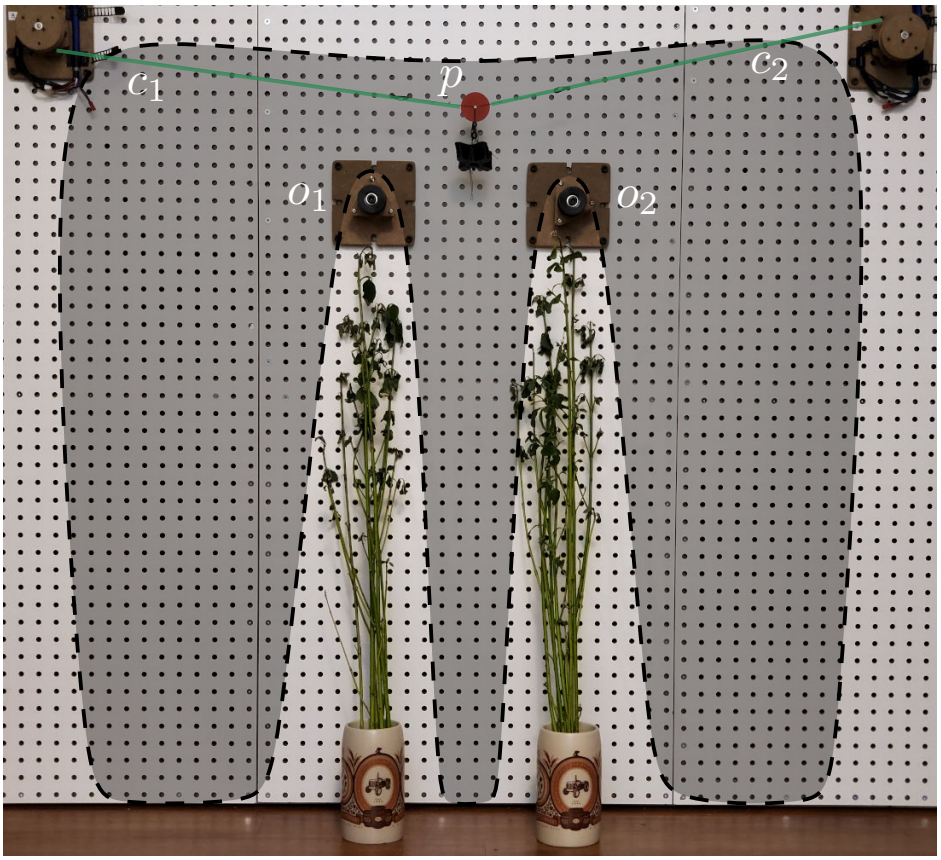

Figure 6.5: Initial condition and approximate workspace for the agricultural VSCR described in Section 6.2.1. Cables are highlighted in green.

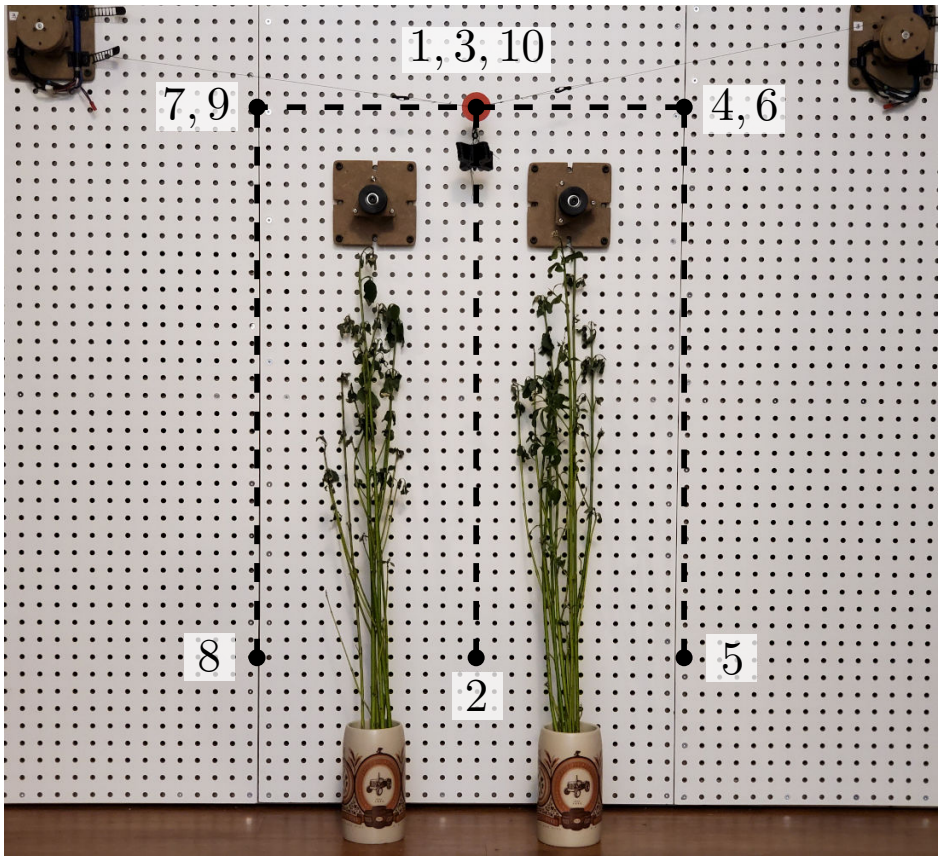

Figure 6.6: Sequence of waypoints followed for the motion studied in Section 6.2.1.

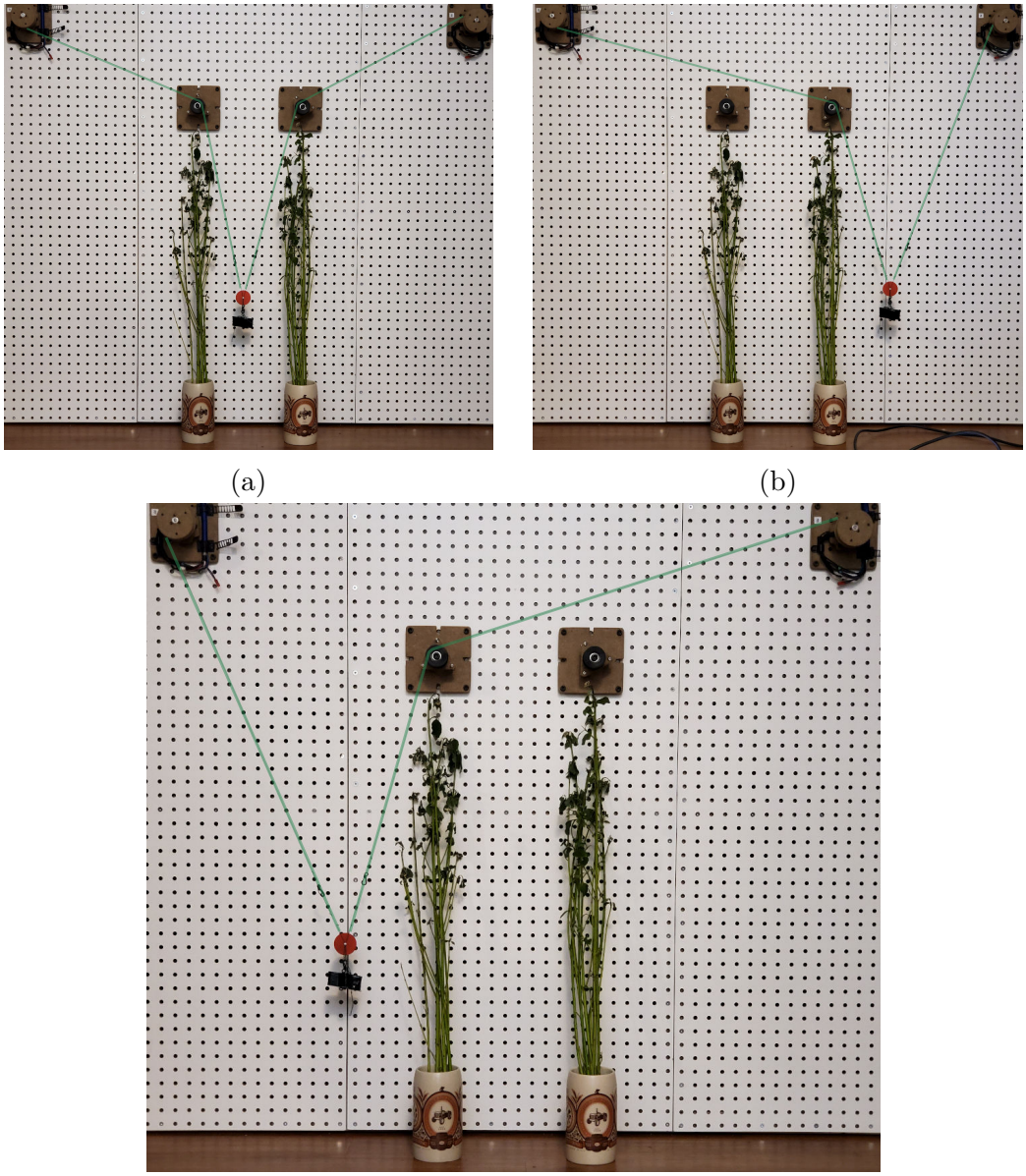

(a) (b)

(c)

Figure 6.7: Various structural configurations observed during the agricultural VSCR trajectory. Cables are highlighted in green.

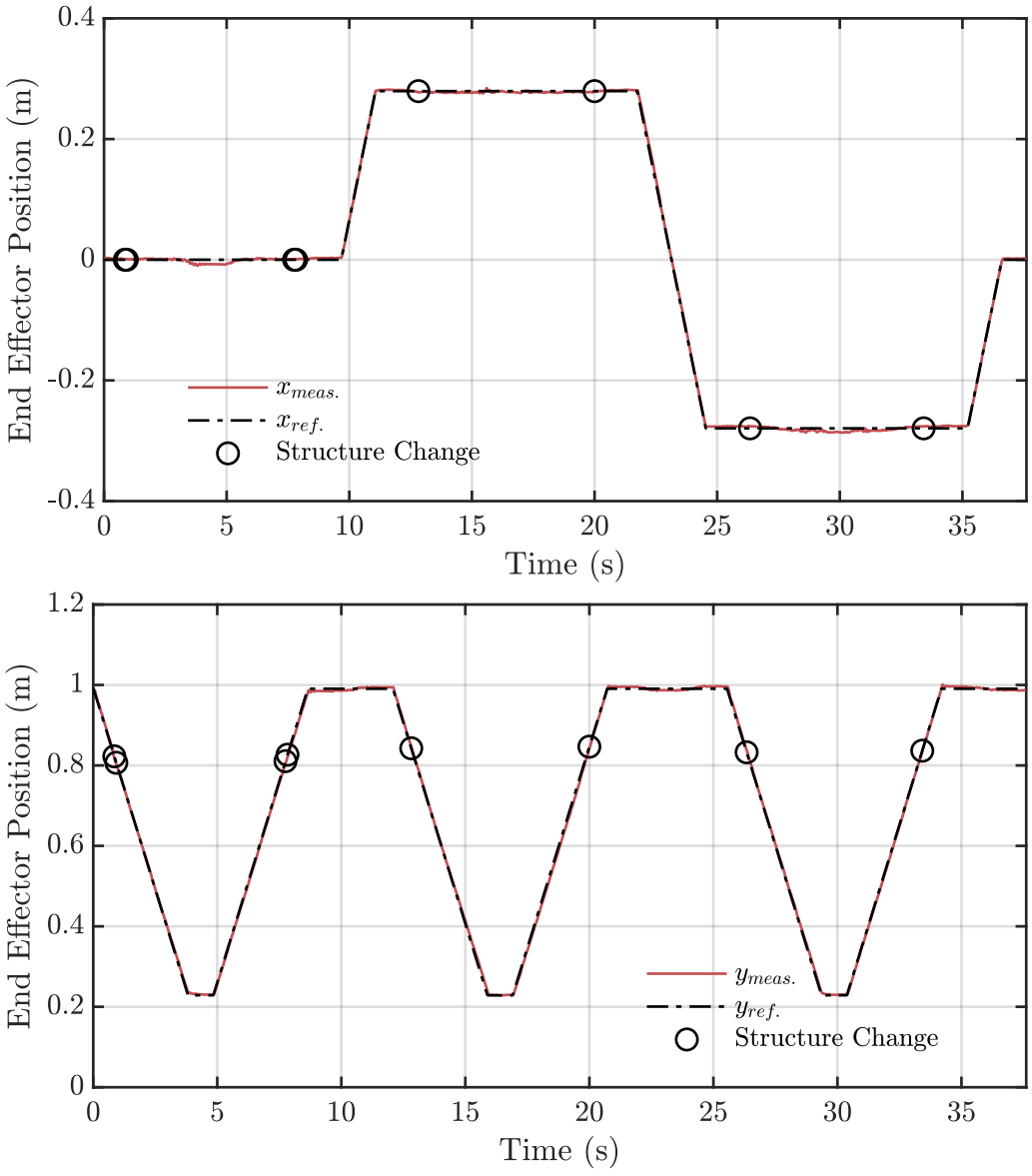

Figure 6.8: Desired and observed end-effector positions during the agricultural VSCR trajectory. x and y correspond to horizontal and vertical positions respectively.

Table 6.1: Winch and idler pulley locations for the agricultural VSCR configuration discussed in Section 6.2.1.

Winch	Center (m,m)	Idler	Center (m,m)
1	$(-0.597,\ 1.092)$	1	$(-0.140,\ 0.864)$
2	$(0.597,\ 1.092)$	2	$(-0.140,\ 0.864)$

Table 6.2: Sequence of end-effector waypoints tracked by the agricultural VSCR during experimental observations.

Waypoint	Location (m,m)
1,3,10	$(0,\ 0.991)$
2	$(0,\ 0.229)$
4,6	$(0.279,\ 0.991)$
5	$(0.279,\ 0.229)$
7,9	$(-0.279,\ 0.991)$
8	$(-0.279,\ 0.229)$

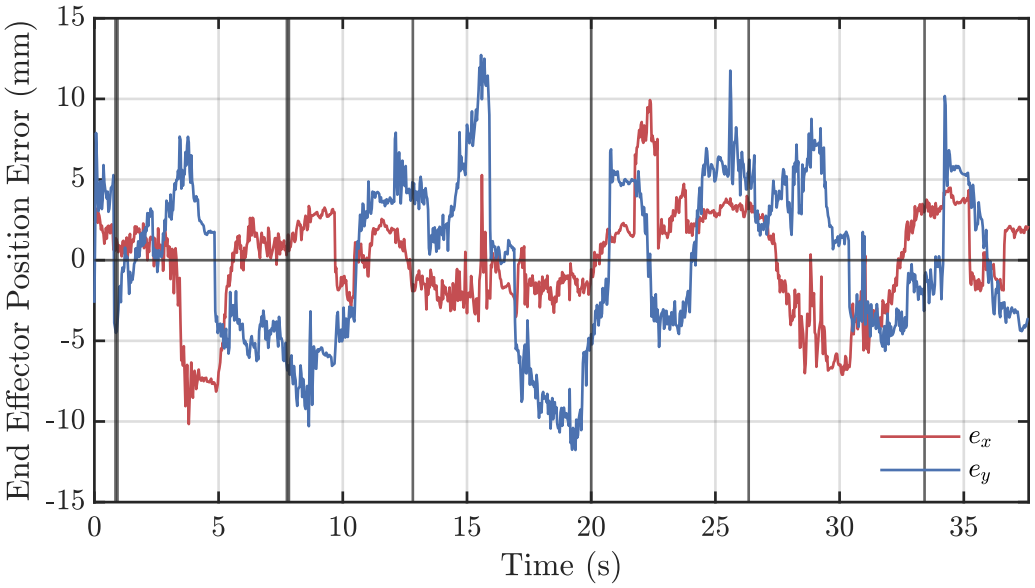

Figure 6.9: End-effector tracking error during the agricultural VSCR trajectory: black vertical bars highlight times when state transitions occur.

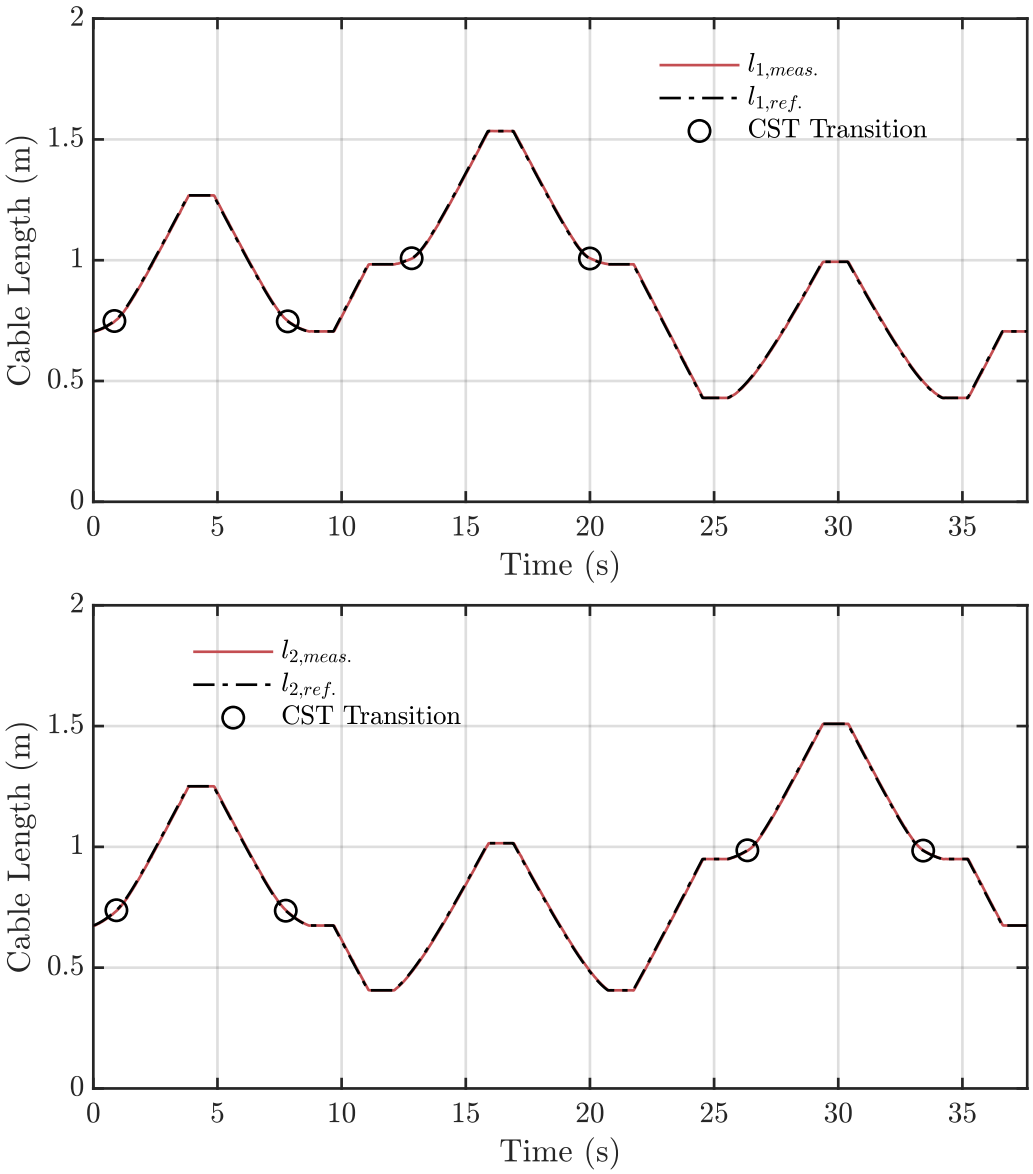

Figure 6.10: Desired and observed cable lengths during the agricultural VSCR trajectory.

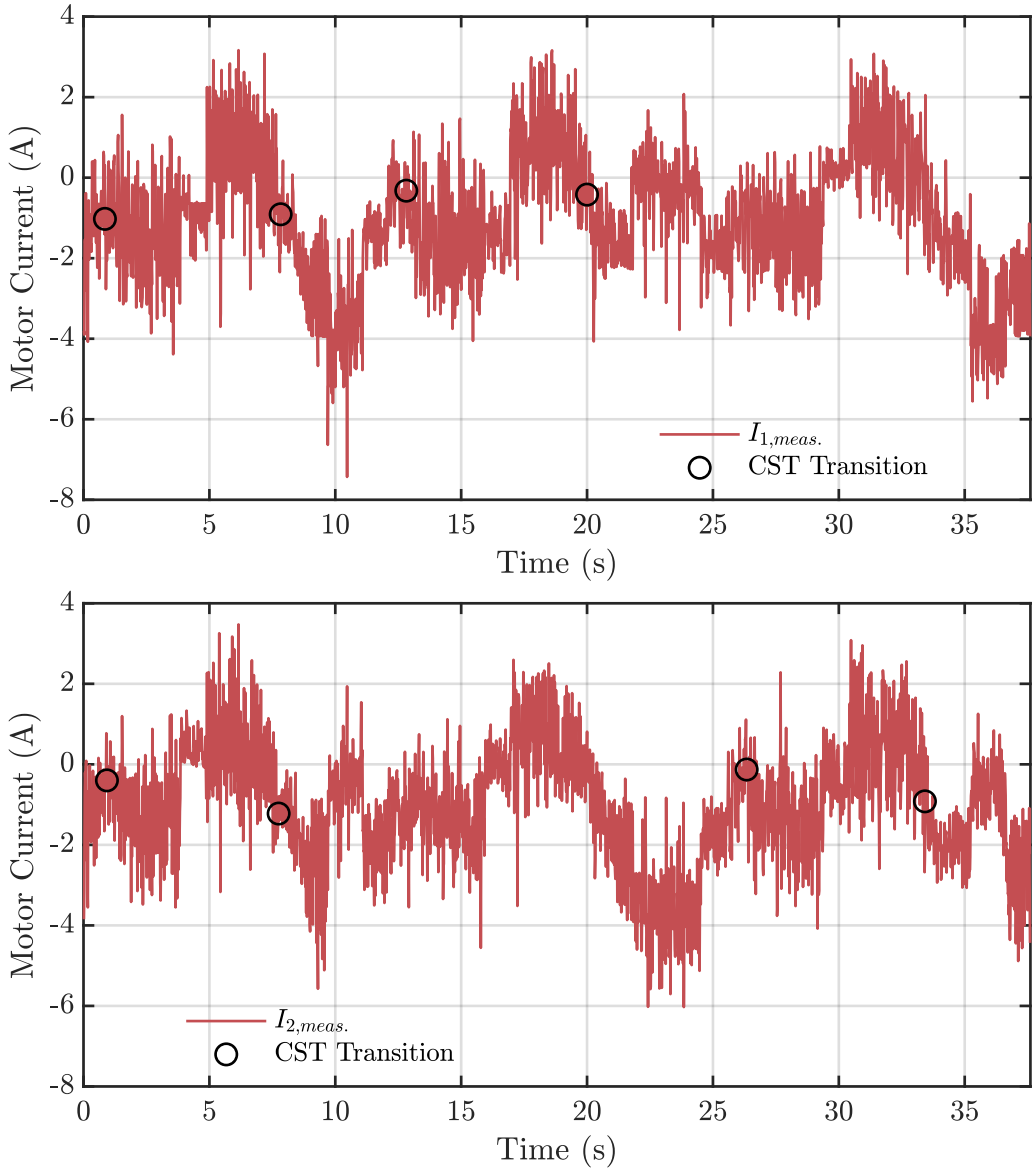

Figure 6.11: Motor currents measured during the agricultural VSCR trajectory for both winches.

6.2.2 Upper Extremity Rehabilitation

This section evaluates a VSCR designed as an end-effector-type upper-extremity rehabilitation robot. This specific target area and rehabilitation type was chosen because it has been studied previously using both rigid [81] and cable-driven [58] robots. For this particular design, the setup was configured as shown in Fig. 6.12 with six cables ($c_{1\text{–}6}$), three collidable idle pulleys ($o_{1\text{–}3}$) and a point mass end effector ($\boldsymbol{p}$). The specific winch and idler anchor locations are provided in Table 6.3. The shaded region in Fig. 6.12 shows the approximate workspace of the robot. By introducing collidable idler pulleys $o_{1\text{–}3}$, collisions between the patient and the cables are avoided. The result is that the reachability of the mechanism can be significantly extended, allowing for the full range of motion of both arms to be covered.

Experimental observations were obtained by following the sequence of waypoints presented in Table 6.4 (shown visually in Fig. 6.13). In order to deal with the control redundancy issue, cables c_1 and c_2 were operated under position control while the remaining cables were operated under torque control. Figure 6.14 highlights some of the distinct structural configurations observed along the trajectory. A recording of the entire motion can be found using the link provided in the footnotes[2]. Figures 6.15 to 6.18 present the desired and observed end-effector trajectories, end-effector tracking errors, cable lengths, and winch currents, respectively with black circular markers and vertical bars being used to highlight the occurrence of any CST node transitions experienced during the motion.

As the results demonstrate, the end effector was able to follow the desired path with a high degree of accuracy with no appreciable loss of performance observed during structural changes. Additionally, CST node transitions were not observed to cause any significant spikes or variations in the recorded motor torques. Through collisions with idler pulleys $o_{1\text{–}3}$, all cables were prevented from entering the patient area.

[2]Section 6.2.2 media extension: https://youtu.be/a8WY_QiS3_0

Table 6.3: Winch and idler locations for the rehabilitation VSCR discussed in Section 6.2.2.

Winch	Center (m,m)	Idler	Center (m,m)
1	$(-0.762,\ 0.483)$	1	$(0,\ 0)$
2	$(0.762,\ 0.483)$	2	$(-0.305,\ -0.102)$
3	$(-0.762,\ -0.508)$	3	$(0.305,\ -0.102)$
4	$(-0.305,\ -0.508)$		
5	$(0.305,\ -0.508)$		
6	$(0.762,\ -0.508)$		

Table 6.4: Sequence of end-effector waypoints tracked by the rehabilitation VSCR during experimental observations.

Waypoint	Location (m,m)
1,8	(0, 0.254)
2,4	(-0.533, 0.254)
3	(-0.533, -0.381)
5,7	(0.533, 0.254)
6	(0.533, -0.381)

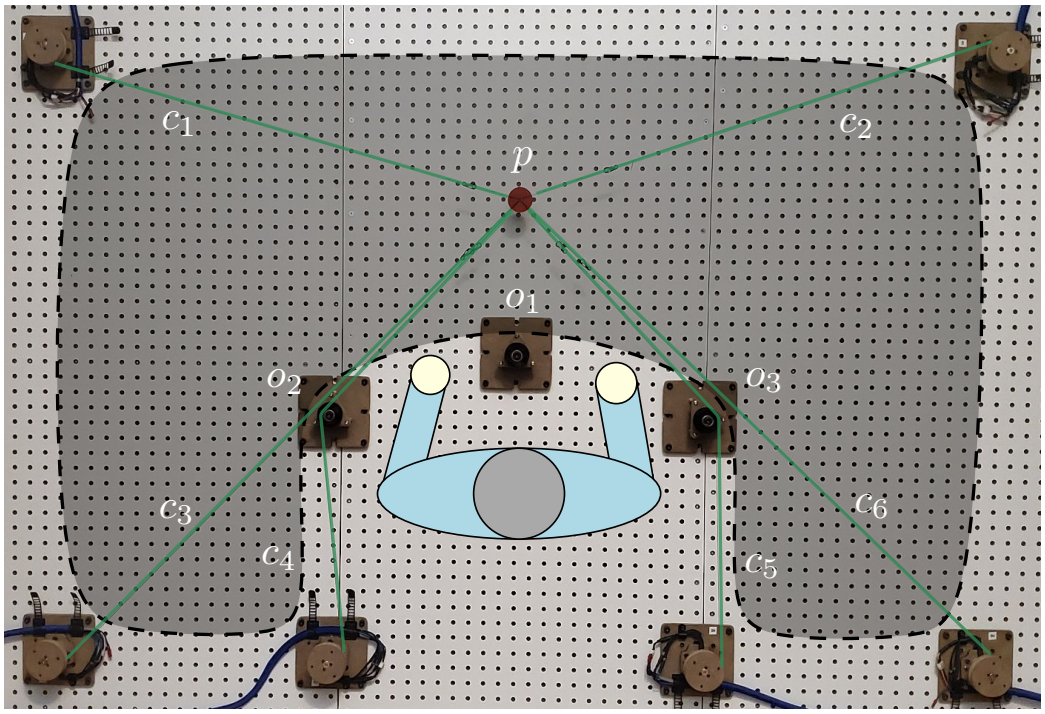

Figure 6.12: Initial condition and approximate workspace for the rehabilitation VSCR discussed in Section 6.2.2. Cables are highlighted in green.

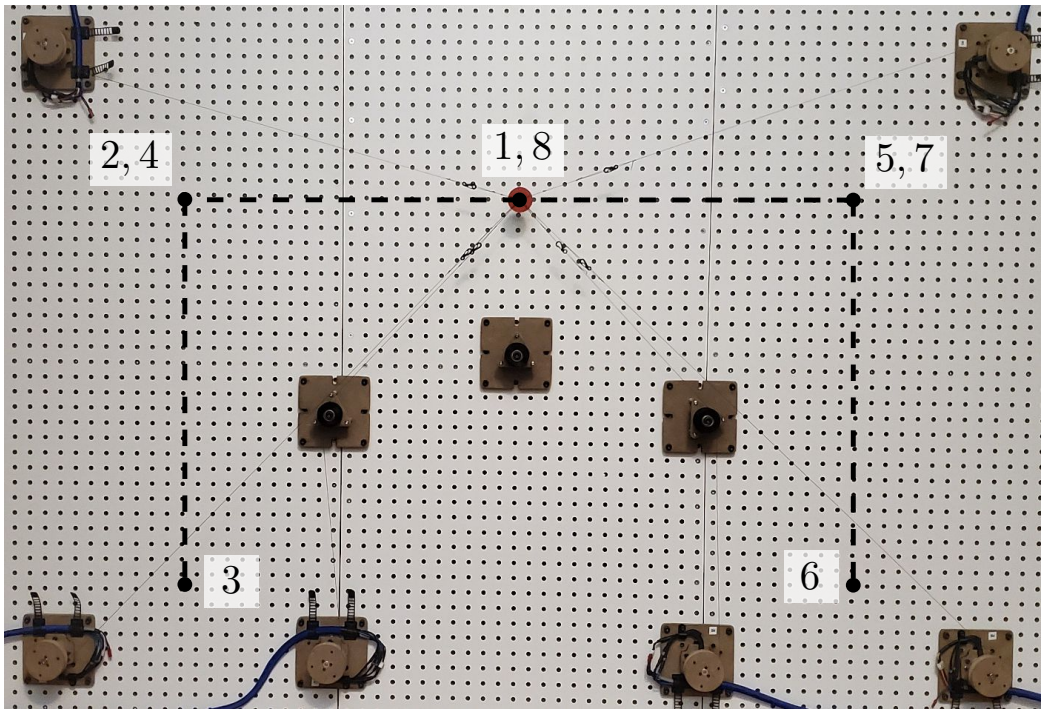

Figure 6.13: Waypoints followed for the rehabilitation VSCR trajectory discussed in Section 6.2.2.

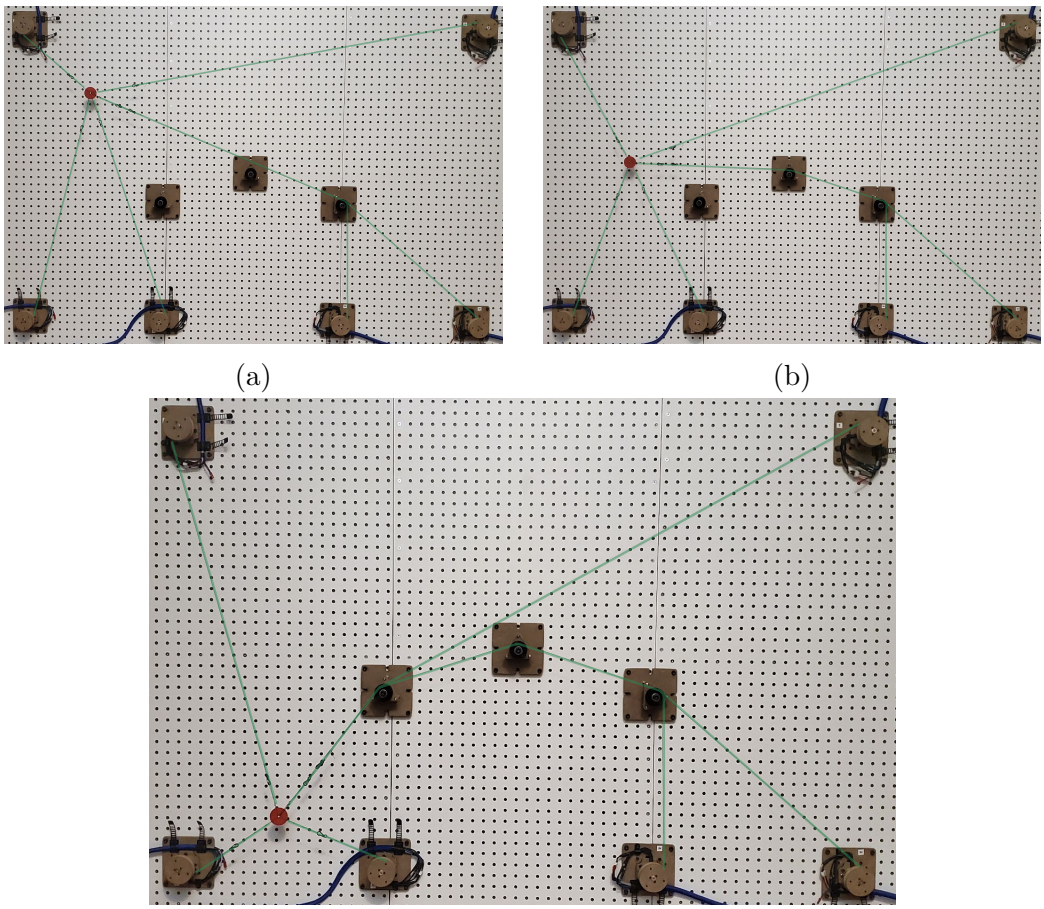

(a) (b)

(c)

Figure 6.14: Various structural configurations observed during the rehabilitation VSCR trajectory. Cables are highlighted in green.

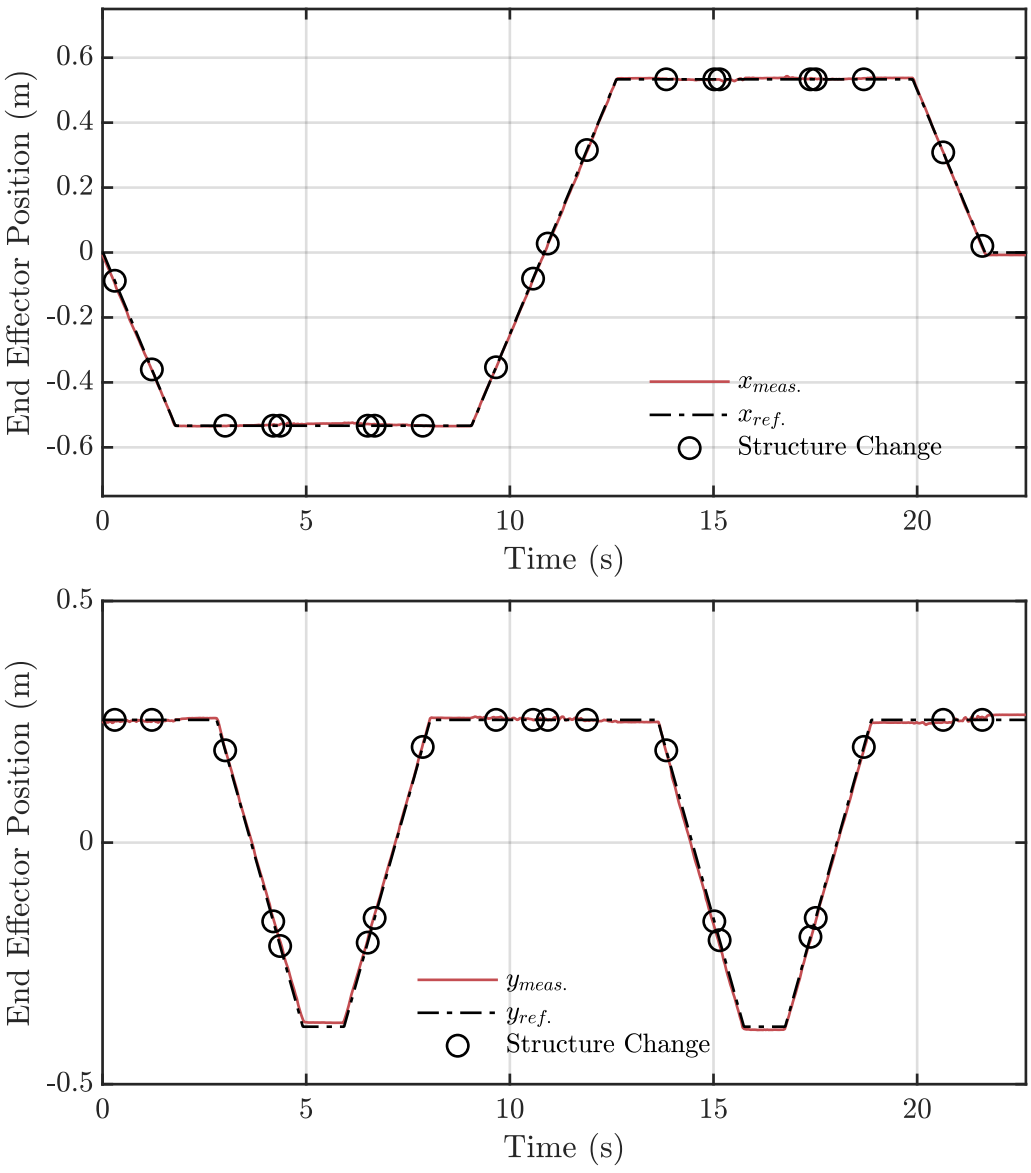

Figure 6.15: Desired and observed end-effector positions for the rehabilitation VSCR trajectory. x and y correspond to horizontal and vertical positions respectively.

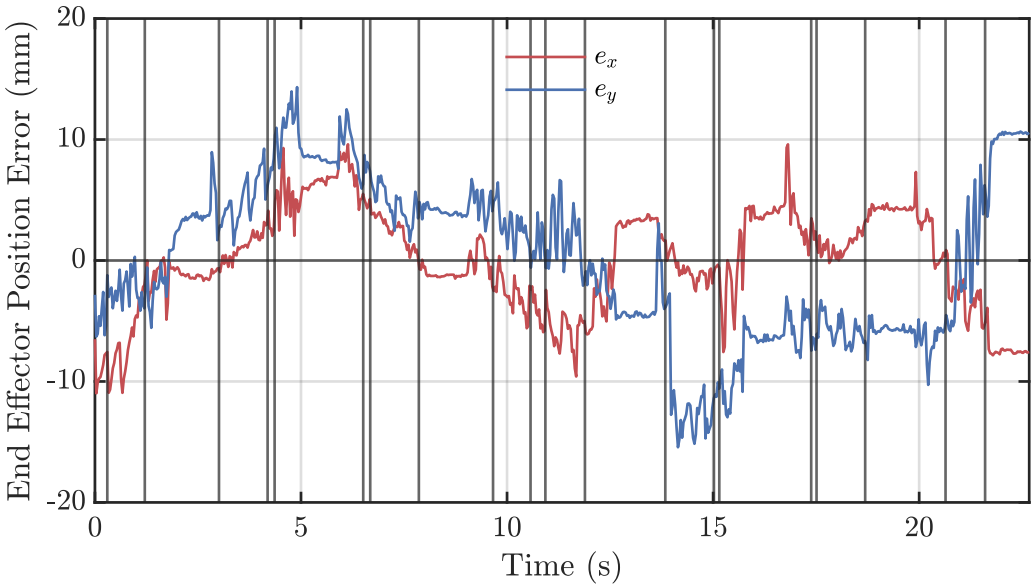

Figure 6.16: End-effector tracking error during the rehabilitation VSCR trajectory: black vertical bars highlight times when state transitions occur.

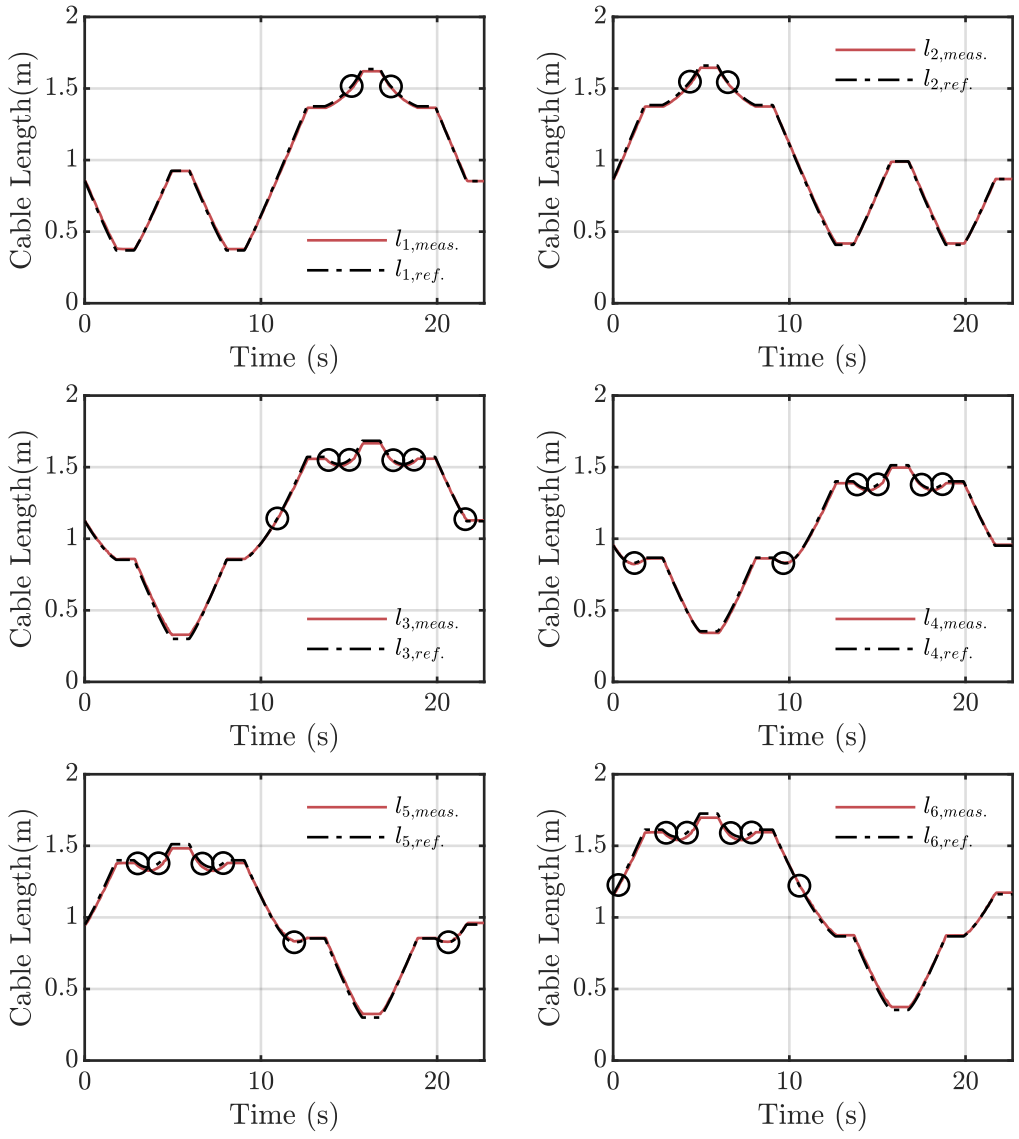

Figure 6.17: Desired and observed cable lengths for the rehabilitation VSCR trajectory. Markers indicate CST node transitions.

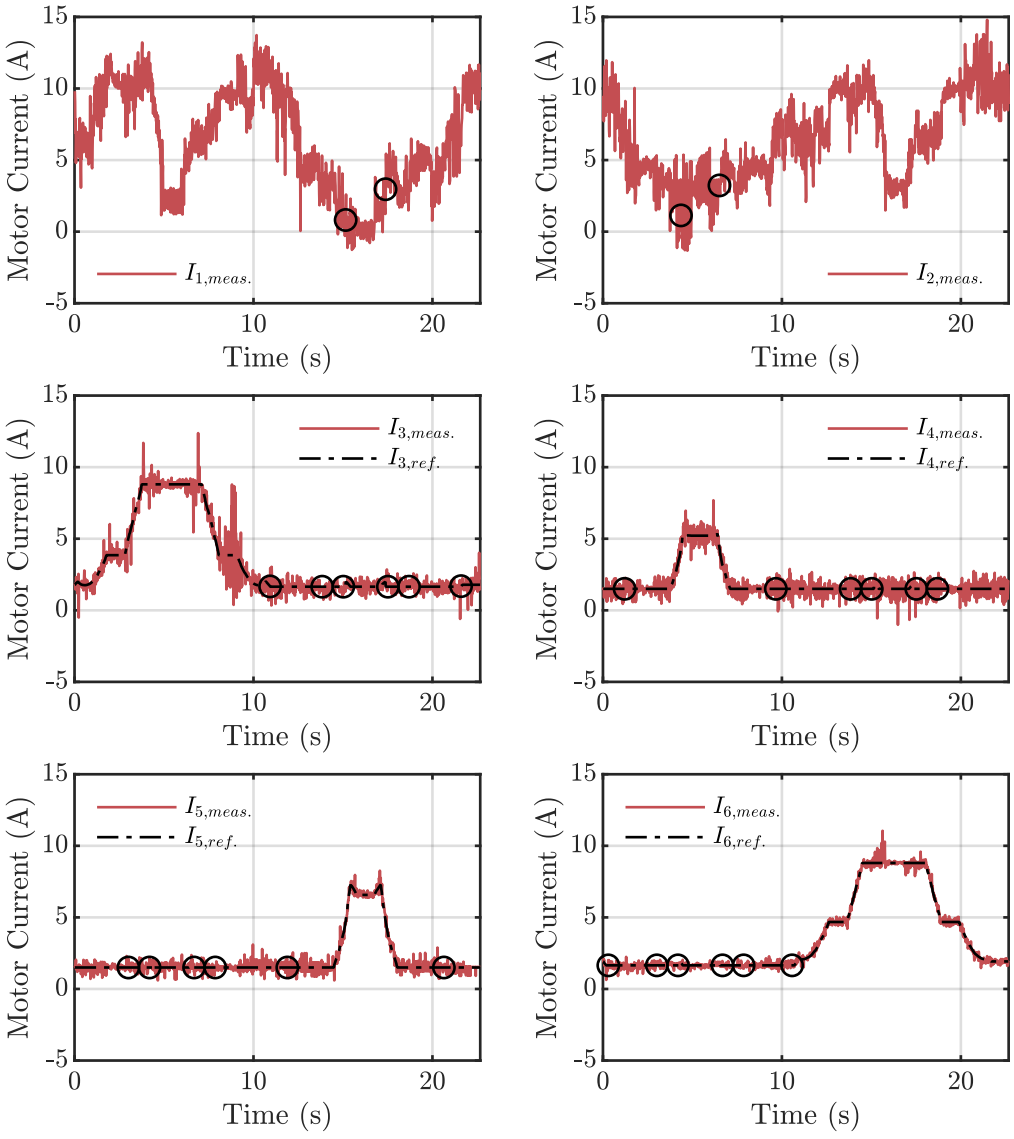

Figure 6.18: Desired and observed winch motor currents for the rehabilitation VSCR trajectory. Markers indicate CST node transitions.

6.2.3 T-Shaped Workspace

This section presents the results obtained from implementing the T-shaped VSCR analyzed in Section 5.3.1, where its SA and WFW were computed (see Fig. 5.9). This VSCR was not designed with any particular application in mind; it is merely meant to serve as a simple demonstration of the ability of VSCRs to cover non-convex installation spaces. The initial configuration of the setup is shown in Fig. 6.19 with the cables (c_{1-6}), idler pulleys (o_{1-2}), and end effector ($\boldsymbol{p}$) highlighted. The specific winch and idler locations are provided in Table 6.5.

The specific sequence of waypoints followed during the experiment are presented in Table 6.6 and shown visually in Fig. 6.20. In order to deal with the control redundancy issue, cables c_1 and c_2 were operated under position control while the remaining cables were operated under torque control. Figure 6.21 shows the robot configuration at various times along the trajectory. A recording of the entire motion can be found using the link provided in the footnotes[3]. Figures 6.22 to 6.25 present the desired and observed end-effector trajectories, end-effector tracking errors, cable lengths, and winch currents, respectively, with black circular markers and vertical bars used to highlight the occurrence of any CST node and chart transitions experienced during the motion.

As the results demonstrate, the end effector was able to follow the desired path with a high degree of accuracy with no appreciable loss of performance observed during structural changes. CST node transitions were not observed to cause any significant spikes or variations in the recorded motor torques. By colliding with idler pulleys o_{1-2}, the cables remained within the allocated T-shaped installation space and did not collide with any of the neighbouring structures.

[3]Section 6.2.3 media extension: https://youtu.be/GkKgq0jaOAo

Table 6.5: Winch and idler pulley locations for the VSCR discussed in Section 6.2.3.

Winch	Center (m,m)	Idler	Center (m,m)
1	(0, 0)	1	(0.6096, −0.4064)
2	(1.6256, 0)	2	(1.0160, −0.4064)
3	(0, −0.4064)		
4	(1.6256, −0.4064)		
5	(0.6096, −1.0160)		
6	(1.0160, −1.0160)		

Table 6.6: Waypoints tracked during the experimental observations discussed in Section 6.2.3.

Waypoint	Location (m,m)
1,3,5,7	(0.8128, -0.2032)
2	(0.1524, -0.2032)
4	(0.8128, -0.8636)
6	(1.4732, -0.2032)

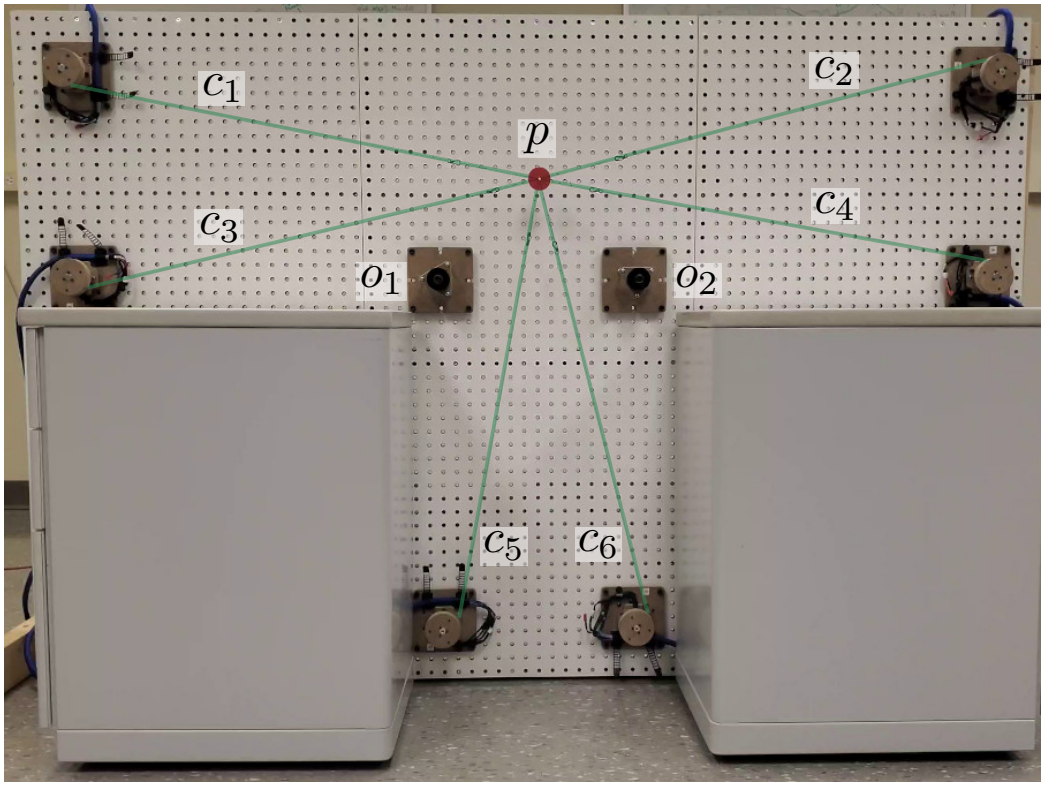

Figure 6.19: Initial configuration of the T-shaped VSCR discussed in Section 6.2.3. Cables are highlighted in green.

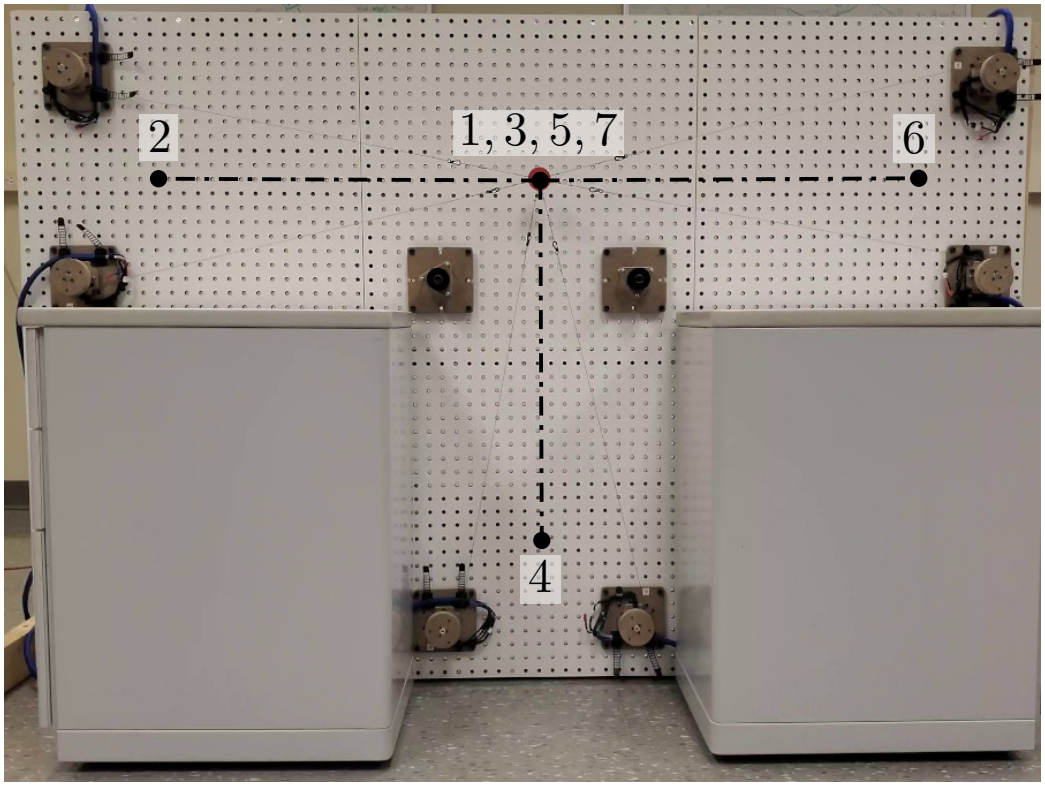

Figure 6.20: Waypoints for the T-shaped VSCR trajectory.

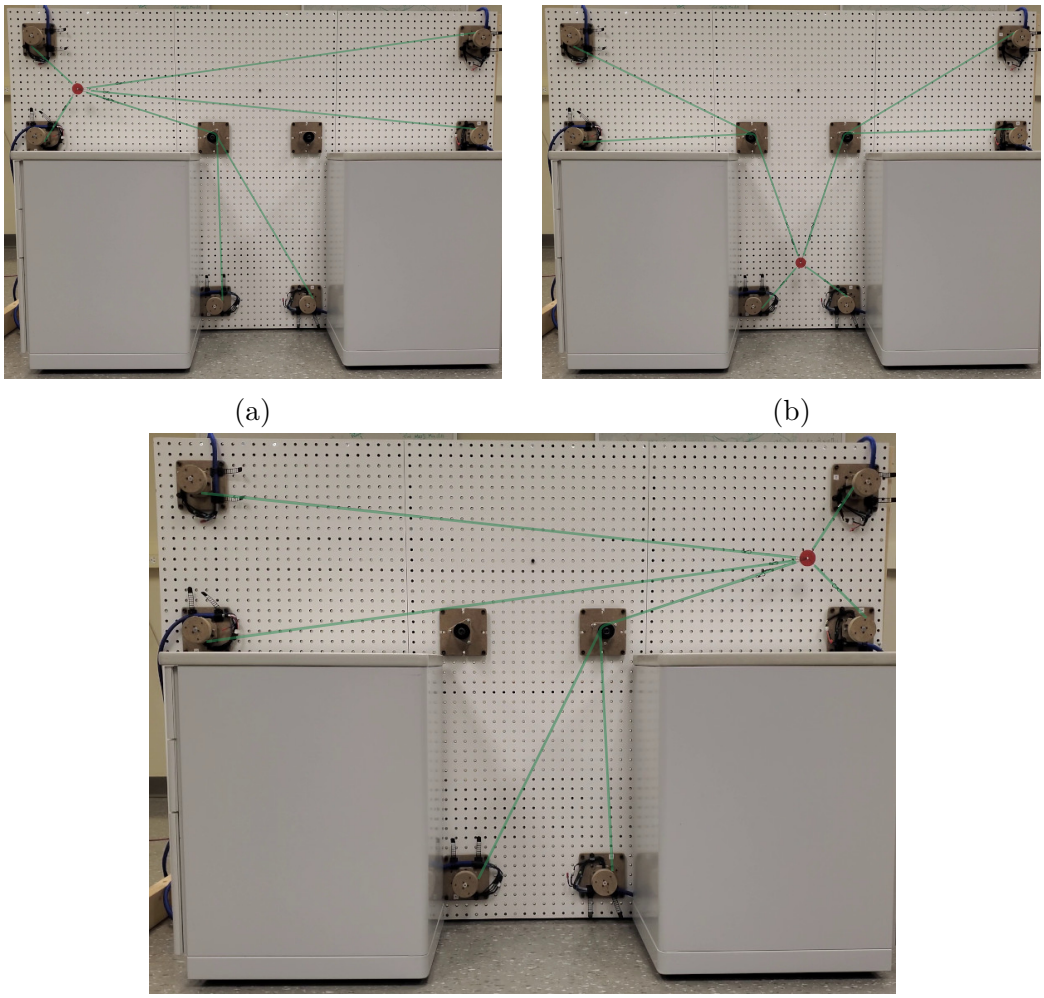

(a) (b)

(c)

Figure 6.21: Various structural configurations observed along the T-shaped VSCR trajectory. Cables are highlighted in green.

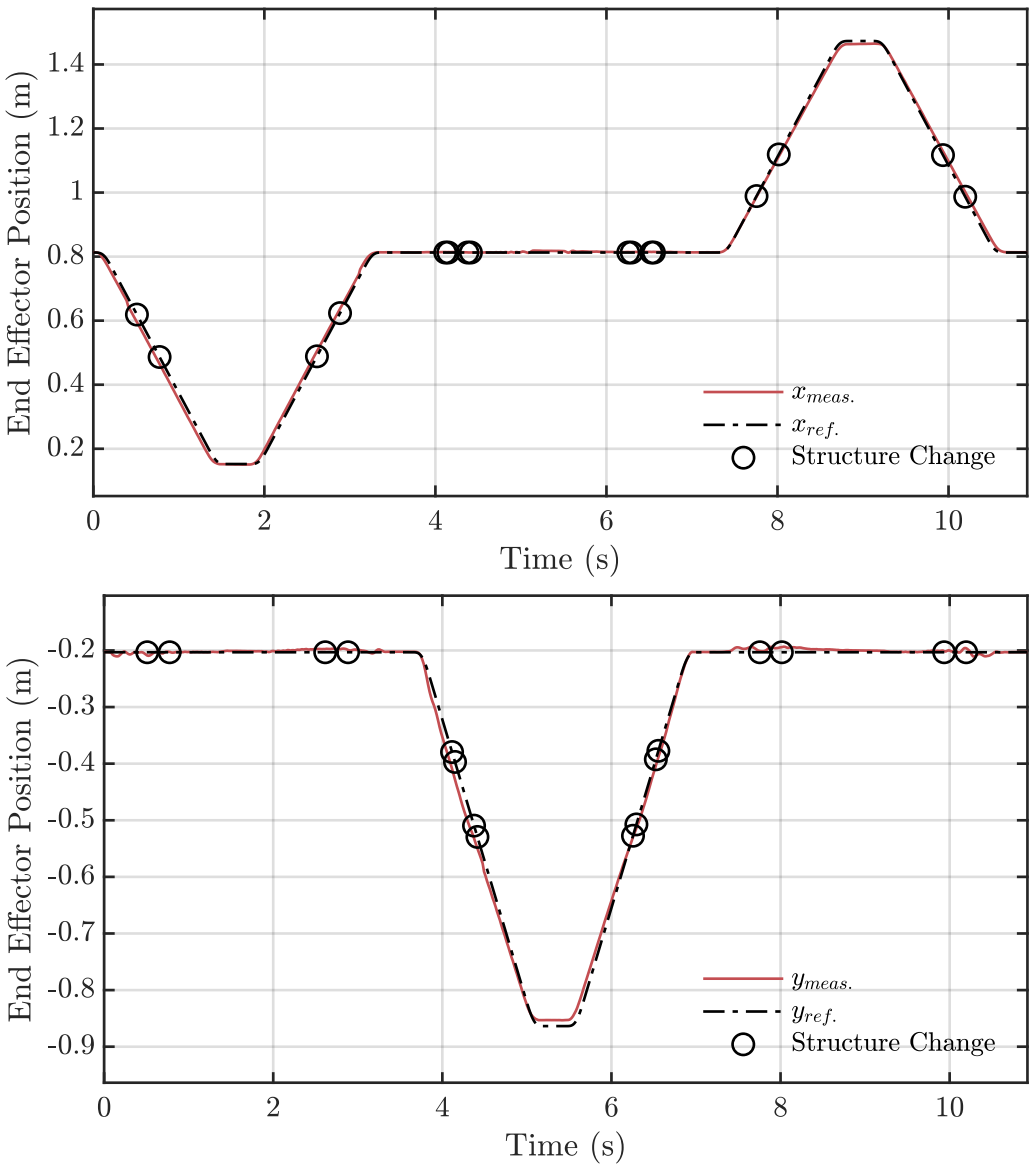

Figure 6.22: Desired and observed end-effector positions for the T-shaped VSCR trajectory discussed in Section 6.2.3. x and y correspond to horizontal and vertical positions respectively.

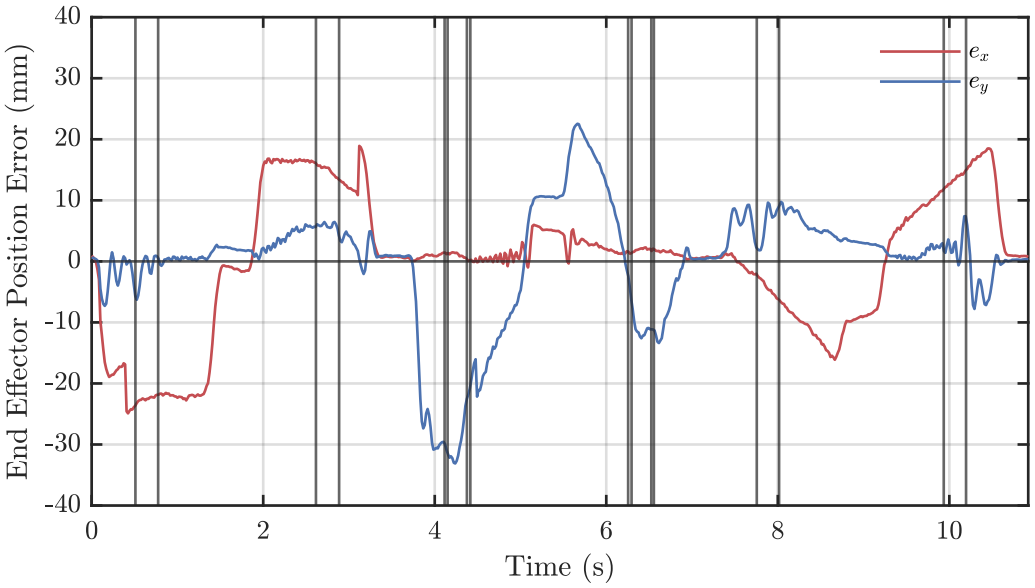

Figure 6.23: End-effector tracking error during the T-shaped VSCR trajectory: black vertical bars highlight times when state transitions occur.

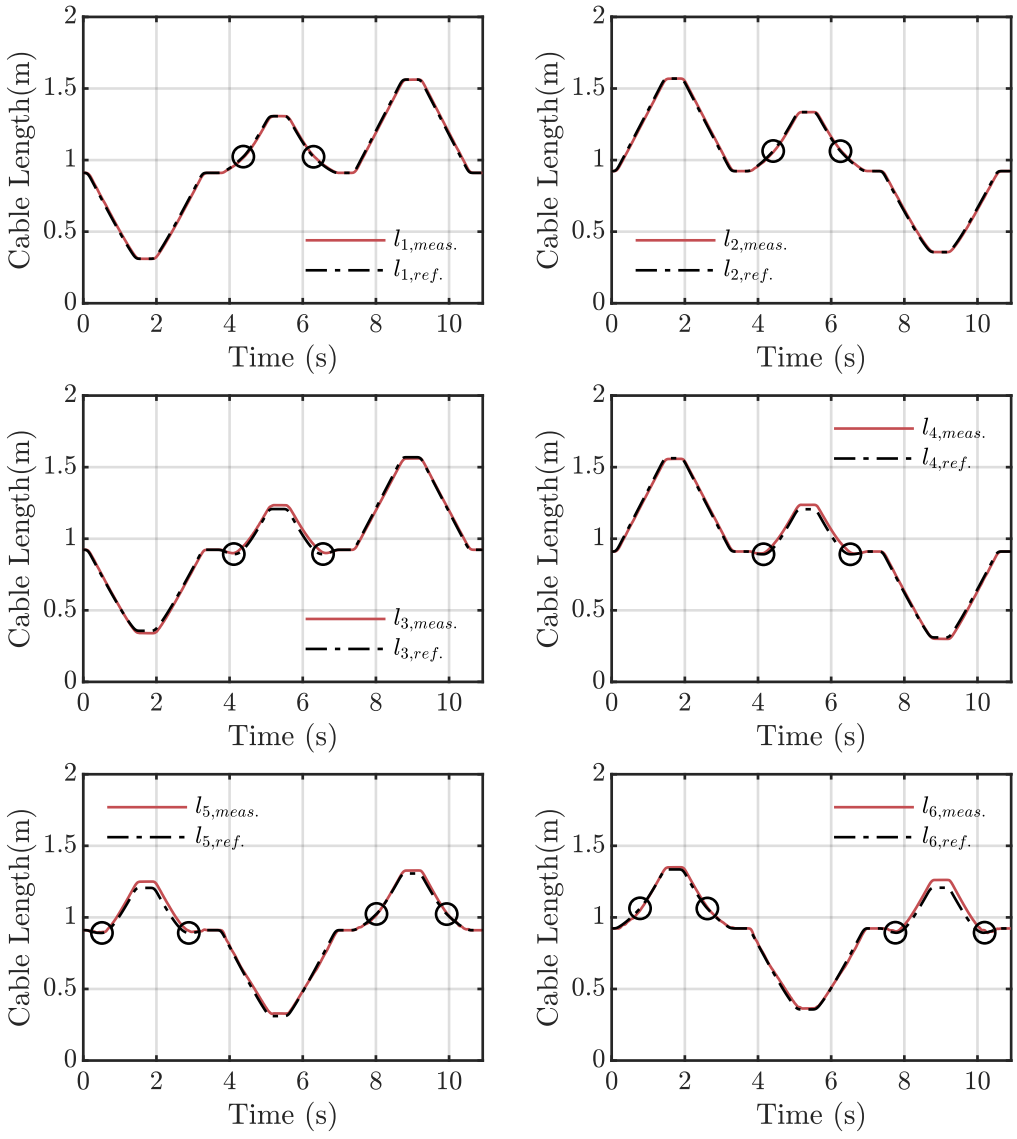

Figure 6.24: Desired and observed cable lengths for the T-shaped VSCR trajectory. Markers indicate CST node transitions.

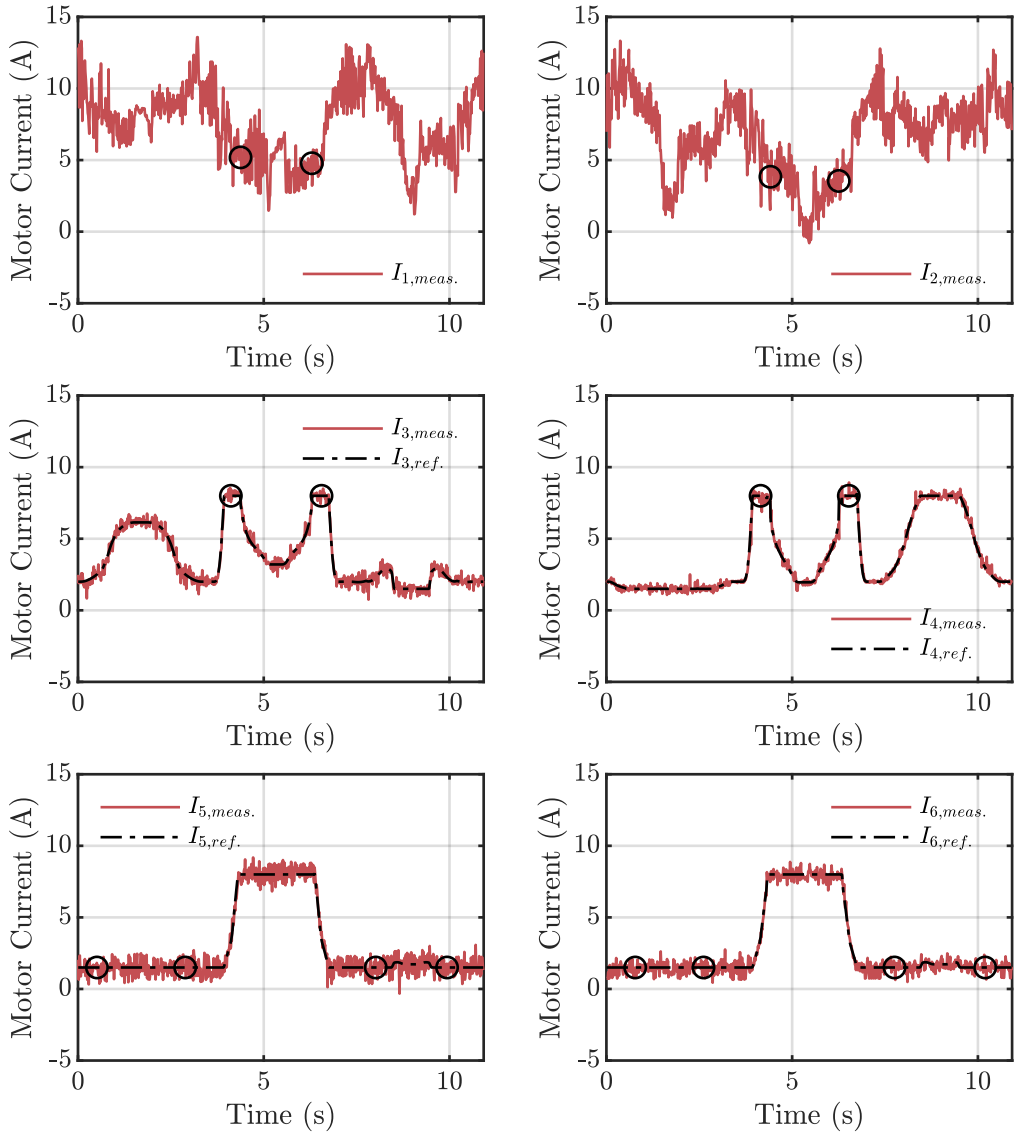

Figure 6.25: Desired and observed winch motor currents for the T-shaped VSCR trajectory. Markers indicate CST node transitions.

6.3 Observations

Overall, the experimental testbed has performed well, and no significant limitations or practical issues have been observed regarding the implementation or control of VSCRs. Occasionally during testing, an idler pulley would fail to capture a cable during a collision approach if the winches and idlers were misaligned such that they were no longer coplanar.

One limitation that was found with the setup is the cable tension sensing strategy: it was assumed that motor currents could be used as an estimate of the cable tensions; however, in using low-cost hobby-grade motors, the high-cogging torque made it difficult to implement accurate tension control based on motor torque feedback alone, especially when operating at low speeds. This issue can potentially be addressed using cogging-torque compensation; however, in the future, it may be necessary to add some form of direct tension measurement (such as load cells) to improve tracking performance.

6.4 Summary

An experimental testbed for investigating planar VSCRs was constructed. The testbed consists of 8 independently controlled direct-drive winches and three collidable idler pulleys, all of which are designed with a common mounting interface to fit in the regularly spaced holes of 1/4 inch pegboard. Several experimental studies were performed to validate the work of the previous chapters. The system performed as predicted, and the experimental results aligned with the model predictions. No significant issues were observed with allowing collisions between cables and the environment.

Chapter 7

Conclusions and Recommendations

7.1 Conclusions

The primary research goal that guided the completion of this thesis was to explore the possibilities created by allowing the cables of a CDPR to collide with and wrap around objects fixed in the environment. Guided by this pursuit, several contributions have been made.

First, a classification system for CDPRs based on the configuration space of the mechanism as a whole relative to its task space was introduced with the existence of each class demonstrated by example. In this classification system, the set of all CDPRs is divided into four distinct classes: constant-structure, reconfigurable, variable-structure (VS), and reconfigurable VS, the latter two being newly identified forms that have not been previously discussed in the literature. VS CDPRs (VSCRs) are distinct in that they are a type of hybrid system, able to instantaneously change their dynamic structure through the use of collisions between cables and objects fixed in the environment. It was shown that VSCRs possess the unique ability to cover non-convex installation spaces: a significant relaxation on the constraints of

traditional CDPRs that has implications for a wide range of applications and a property that can be exploited to dramatically extend the reachability and accessible workspace of CDPRs in cluttered environments. Because of their unique properties and potential for addressing the primary research objective of this thesis, the remainder of the thesis was devoted to developing the theoretical foundations for the study of VSCRs to enable their development and provide a starting point for supporting future research on the subject.

Beginning the study of VSCRs, an extended cable model was developed to represent cables where collisions with and separations from objects fixed in the environment are permitted. An iterative inverse kinematics method was then developed using the extended cable model that keeps track of the cable state over time and detects any new collisions or separations experienced during a motion.

Using the insight gained from the extended cable model (which looks at each cable independently), the nature of the VSCR workspace was studied next. It was found that VSCR workspaces can be represented in their entirety by dividing the workspace into a collection of overlapping charts based on regions of constant structure that collectively cover the entire workspace. This concept has been introduced as the 'structure atlas' (SA) along with a general method for its computation. The SA is shown to be a powerful tool for analyzing VSCRs with specific applications to workspace analysis and inverse kinematics having been demonstrated.

Finally, to validate the previously discussed theoretical results and observe the real-world effects of collisions on control performance, an experimental testbed was designed and built specifically for the study of VSCRs. Several experiments were performed using this testbed, simulating potential application scenarios such as agriculture and rehabilitation. The observed experimental performance aligned closely with the theoretical models, and no major practical concerns or limitations were observed during testing.

It is worth noting that the bulk of the analysis performed in this thesis

has been entirely limited to the scope of planar VSCRs. While the concepts and modelling approaches introduced will likely be a good starting point for future research into spatial VSCRs, the extension is non-trivial and likely to involve a significant increase in modelling complexity. Given the limited time available for completing this thesis, the study of spatial VSCRs has been left as a topic for future research.

7.2 Recommendations for Future Research

As a new class of robotic manipulators with very little published on the subject outside of this thesis, the study of VSCRs is currently a wide-open field. Many fundamental problems remain untouched, such as forward kinematics, calibration, pose estimation, and trajectory planning. While reconfigurable VSCRs have been identified in this thesis, they have not been investigated past the point of definition. Thus, reconfigurable VSCRs mark another avenue for future research.

Regarding the design of VSCRs, there is currently no systematic way of determining where collidable objects should be placed or how many are required for satisfying a given design objective. Additionally, cable tolerance to non-ideal contact conditions and long-term cable wear that may occur from repeated collision, separation, and sliding against an object's surface should be investigated to better understand the practical limitations.

To date, past demonstrations of VSCRs have been limited to planar examples. Extending these results to general spatial systems will likely be a significant modelling challenge. In the planar case, it is safe to assume that slippage occurs only in the tangential direction; however, this cannot be guaranteed for a spatial contact, and surface stability must be considered (for example, the unstable contact between a cable and a sphere). Using cylindrical columns or eyelets which allow cable capture only in certain poses may be a useful starting point.

All existing results have assumed that the exact location and geometry of the collidable objects are known beforehand. This is reasonable to assume for mechanisms in controlled environments; however, it is not hard to imagine that this may not always be the case: for deployable CDPRs or those working in dynamic environments, this information is usually not available. There is still much research that needs to be done in terms of detecting collisions along the length of a cable, estimating an object's geometry, and updating the mechanism's internal kinematic model online in order to maintain a desired platform motion; however, the ability to operate in the presence of unknown objects has an exciting potential and is a problem that if solved could greatly enhance the usability and adaptability of CDPRs in unstructured or unknown environments.

Bibliography

[1] Leonard G. Skycamhd suspended video device. https://commons.wikimedia.org/wiki/File:SkycamHDClipEnhanced0346.jpg, September 2007.

[2] Peng Jiang, YouLing Yue, HengQian Gan, Rui Yao, Hui Li, GaoFeng Pan, JingHai Sun, DongJun Yu, HongFei Liu, NingYu Tang, et al. Commissioning progress of the fast. *SCIENCE CHINA Physics, Mechanics & Astronomy*, 62(5):959502, 2019.

[3] Brian E. Jackson, Taylor A. Howell, Kunal Shah, Mac Schwager, and Zachary Manchester. Scalable Cooperative Transport of Cable-Suspended Loads With UAVs Using Distributed Trajectory Optimization. *IEEE Robotics and Automation Letters*, 5(2):3368–3374, April 2020. Conference Name: IEEE Robotics and Automation Letters.

[4] AEMK Systems. Deltabot cable. https://aemksystems.com, January 2022.

[5] Motek. Rysen. https://www.ikbenstil.nl/media/image/2f/c0/7b/Motek-RYSEN_4.jpg, January 2022.

[6] Michiel Plooij, Urs Keller, Bram Sterke, Salif Komi, Heike Vallery, and Joachim Von Zitzewitz. Design of rysen: an intrinsically safe and low-power three-dimensional overground body weight support. *IEEE Robotics and Automation Letters*, 3(3):2253–2260, 2018.

[7] Saeed Behzadipour and Amir Khajepour. Stiffness of Cable-based Parallel Manipulators With Application to Stability Analysis. *Journal of Mechanical Design*, 128(1):303–310, April 2005.

BIBLIOGRAPHY

[8] Wen Bin Lim, Guilin Yang, Song Huat Yeo, and Shabbir Kurbanhusen Mustafa. A generic force-closure analysis algorithm for cable-driven parallel manipulators. *Mechanism and Machine Theory*, 46(9):1265–1275, 2011.

[9] Saeed Abdolshah, Damiano Zanotto, Giulio Rosati, and Sunil K. Agrawal. Optimizing Stiffness and Dexterity of Planar Adaptive Cable-Driven Parallel Robots. *Journal of Mechanisms and Robotics*, 9(3), June 2017. Publisher: American Society of Mechanical Engineers Digital Collection.

[10] Michael Anson, Aliakbar Alamdari, and Venkat Krovi. Orientation Workspace and Stiffness Optimization of Cable-Driven Parallel Manipulators With Base Mobility. *Journal of Mechanisms and Robotics*, 9(3), June 2017. Publisher: American Society of Mechanical Engineers Digital Collection.

[11] Mitchell Rushton and Amir Khajepour. Transverse vibration control in planar cable-driven robotic manipulators. In Clément Gosselin, Philippe Cardou, Tobias Bruckmann, and Andreas Pott, editors, *Cable-Driven Parallel Robots*, pages 243–253, Cham, 2018. Springer International Publishing.

[12] Mitchell Rushton, Hamed Jamshidifar, and Amir Khajepour. Multi-axis reaction system (mars) for vibration control of planar cable-driven parallel robots. *IEEE Transactions on Robotics*, 35(4):1039–1046, 2019.

[13] Loïc Cuvillon, Xavier Weber, and Jacques Gangloff. Modal Control for Active Vibration Damping of Cable-Driven Parallel Robots. *Journal of Mechanisms and Robotics*, 12(5), 03 2020. 051004.

[14] Simon Perreault, Philippe Cardou, Clément M. Gosselin, and Martin J.-D. Otis. Geometric Determination of the Interference-Free Constant-Orientation Workspace of Parallel Cable-Driven Mechanisms. *Journal of Mechanisms and Robotics*, 2(3), August 2010.

[15] Lorenzo Gagliardini, Stéphane Caro, Marc Gouttefarde, and Alexis Girin. Discrete reconfiguration planning for cable-driven parallel robots. *Mechanism and Machine Theory*, 100:313–337, 2016.

[16] Andreas Pott. Determination of the Cable Span and Cable Deflection of Cable-Driven Parallel Robots. In Clément Gosselin, Philippe Cardou, Tobias Bruckmann, and Andreas Pott, editors, *Cable-Driven Parallel Robots*, volume 53, pages 106–116. Springer International Publishing, Cham, 2018. Series Title: Mechanisms and Machine Science.

[17] Bingyao Wang, Bin Zi, Sen Qian, and Dan Zhang. Collision free force closure workspace determination of reconfigurable planar cable driven parallel robot. In *2016 Asia-Pacific Conference on Intelligent Robot Systems (ACIRS)*, pages 26–30. IEEE, 2016.

[18] Marc Fabritius, Christoph Martin, and Andreas Pott. Calculation of the cable-platform collision-free total orientation workspace of cable-driven parallel robots. In *International Conference on Cable-Driven Parallel Robots*, pages 137–148. Springer, 2019.

[19] Samir Lahouar, Erika Ottaviano, Said Zeghoul, Lotfi Romdhane, and Marco Ceccarelli. Collision free path-planning for cable-driven parallel robots. *Robotics and Autonomous Systems*, 57(11):1083–1093, 2009.

[20] Jeong-Hyeon Bak, Sung Wook Hwang, Jonghyun Yoon, Jong Hyeon Park, and Jong-Oh Park. Collision-free path planning of cable-driven parallel robots in cluttered environments. *Intelligent Service Robotics*, pages 1–11, 2019.

[21] Andreas Pott. *Cable-Driven Parallel Robots: Theory and Application*, volume 120 of *Springer Tracts in Advanced Robotics*. Springer International Publishing, Cham, 2018.

[22] Stephen Boyd, Stephen P Boyd, and Lieven Vandenberghe. *Convex optimization*. Cambridge university press, 2004.

[23] Mahir Hassan and Amir Khajepour. Optimization of actuator forces in cable-based parallel manipulators using convex analysis. *IEEE Transactions on Robotics*, 24(3):736–740, 2008.

[24] Hussein Hussein, João Cavalcanti Santos, Jean-Baptiste Izard, and Marc Gouttefarde. Smallest maximum cable tension determination for cable-driven parallel robots. *IEEE Transactions on Robotics*, 2021.

[25] Hamed Jamshidifar, Amir Khajepour, Baris Fidan, and Mitchell Rushton. Kinematically-constrained redundant cable-driven parallel robots: modeling, redundancy analysis, and stiffness optimization. *IEEE/ASME Transactions on Mechatronics*, 22(2):921–930, 2016.

[26] Etienne Picard, Stéphane Caro, Franck Plestan, and Fabien Claveau. Stiffness oriented tension distribution algorithm for cable-driven parallel robots. In *International Symposium on Advances in Robot Kinematics*, pages 209–217. Springer, 2020.

[27] Andreas Pott, Tobias Bruckmann, and Lars Mikelsons. Closed-form force distribution for parallel wire robots. In *Computational Kinematics*, pages 25–34. Springer, 2009.

[28] Andreas Pott. An improved force distribution algorithm for over-constrained cable-driven parallel robots. In *Computational Kinematics*, pages 139–146. Springer, 2014.

[29] Marc Gouttefarde and Cle´ ment M Gosselin. On the properties and the determination of the wrench-closure workspace of planar parallel cable-driven mechanisms. In *International Design Engineering Technical Conferences and Computers and Information in Engineering Conference*, volume 46954, pages 337–346, 2004.

[30] P. Bosscher, A.T. Riechel, and I. Ebert-Uphoff. Wrench-feasible workspace generation for cable-driven robots. *IEEE Transactions on Robotics*, 22(5):890–902, October 2006.

[31] Javad Bolboli, Mohammad A Khosravi, and Farzaneh Abdollahi. Stiffness feasible workspace of cable-driven parallel robots with application to optimal design of a planar cable robot. *Robotics and Autonomous Systems*, 114:19–28, 2019.

[32] Marc Gouttefarde, David Daney, and Jean-Pierre Merlet. Interval-Analysis-Based Determination of the Wrench-Feasible Workspace of Parallel Cable-Driven Robots. *IEEE Transactions on Robotics*, 27(1):1–13, February 2011. Conference Name: IEEE Transactions on Robotics.

[33] Ghasem Abbasnejad, Jonathan Eden, and Darwin Lau. Generalized Ray-Based Lattice Generation and Graph Representation of Wrench-Closure Workspace for Arbitrary Cable-Driven Robots. *IEEE Transactions on Robotics*, 35(1):147–161, February 2019. Conference Name: IEEE Transactions on Robotics.

[34] M. Gouttefarde and C.M. Gosselin. Analysis of the wrench-closure workspace of planar parallel cable-driven mechanisms. *IEEE Transactions on Robotics*, 22(3):434–445, June 2006.

[35] Ethan Stump and Vijay Kumar. Workspaces of Cable-Actuated Parallel Manipulators. *Journal of Mechanical Design*, 128(1):159–167, July 2005.

[36] So-Ryeok Oh and Sunil Kumar Agrawal. Generation of feasible set points and control of a cable robot. *IEEE Transactions on Robotics*, 22(3):551–558, 2006.

[37] Bin Zi, BY Duan, JL Du, and Hong Bao. Dynamic modeling and active control of a cable-suspended parallel robot. *Mechatronics*, 18(1):1–12, 2008.

[38] Kun Yu, Leng-Feng Lee, Chin Pei Tang, and Venkat N Krovi. Enhanced trajectory tracking control with active lower bounded stiffness control for cable robot. In *2010 IEEE International Conference on Robotics and Automation*, pages 669–674, Anchorage, AK, May 2010. IEEE.

[39] Jérémy Begey, Loïc Cuvillon, Maximilien Lesellier, Marc Gouttefarde, and Jacques Gangloff. Dynamic Control of Parallel Robots Driven by Flexible Cables and Actuated by Position-Controlled Winches. *IEEE Transactions on Robotics*, 35(1):286–293, February 2019. Conference Name: IEEE Transactions on Robotics.

[40] Tobias Bruckmann, Lars Mikelsons, Manfred Hiller, and Dieter Schramm. A new force calculation algorithm for tendon-based parallel manipulators. In *2007 IEEE/ASME international conference on advanced intelligent mechatronics*, pages 1–6, September 2007. ISSN: 2159-6255.

[41] Christoph Martin, Marc Fabritius, Johannes T Stoll, and Andreas Pott. Accuracy improvement for cdprs based on direct cable length measure-

ment sensors. In *International Conference on Cable-Driven Parallel Robots*, pages 348–359. Springer, 2021.

[42] Zane Zake, François Chaumette, Nicolò Pedemonte, and Stéphane Caro. Vision-based control and stability analysis of a cable-driven parallel robot. *IEEE Robotics and Automation Letters*, 4(2):1029–1036, 2019.

[43] Tej Dallej, Marc Gouttefarde, Nicolas Andreff, Pierre-Elie Hervé, and Philippe Martinet. Modeling and vision-based control of large-dimension cable-driven parallel robots using a multiple-camera setup. *Mechatronics*, 61:20–36, 2019.

[44] Werner Kraus, Michael Kessler, and Andreas Pott. Pulley friction compensation for winch-integrated cable force measurement and verification on a cable-driven parallel robot. In *2015 IEEE International Conference on Robotics and Automation (ICRA)*, pages 1627–1632, May 2015. ISSN: 1050-4729.

[45] Jonas Bieber, David Bernstein, Micha Schuster, Konrad Wauer, and Michael Beitelschmidt. Motor Current Based Force Control of Simple Cable-Driven Parallel Robots. In Marc Gouttefarde, Tobias Bruckmann, and Andreas Pott, editors, *Cable-Driven Parallel Robots*, volume 104, pages 271–283. Springer International Publishing, Cham, 2021. Series Title: Mechanisms and Machine Science.

[46] Andreas Pott. Influence of pulley kinematics on cable-driven parallel robots. In *Latest Advances in Robot Kinematics*, pages 197–204. Springer, 2012.

[47] Valentin Schmidt and Andreas Pott. Implementing extended kinematics of a cable-driven parallel robot in real-time. In *Cable-driven parallel robots*, pages 287–298. Springer, 2013.

[48] Mohammad A Khosravi and Hamid D Taghirad. Dynamic analysis and control of cable driven robots with elastic cables. *Transactions of the Canadian Society for Mechanical Engineering*, 35(4):543–557, 2011.

[49] Philipp Miermeister, Werner Kraus, Tian Lan, and Andreas Pott. An Elastic Cable Model for Cable-Driven Parallel Robots Including Hysteresis Effects. In Andreas Pott and Tobias Bruckmann, editors, *Cable-*

Driven Parallel Robots, volume 32, pages 17–28. Springer International Publishing, Cham, 2015. Series Title: Mechanisms and Machine Science.

[50] K. Kozak, Qian Zhou, and Jinsong Wang. Static analysis of cable-driven manipulators with non-negligible cable mass. *IEEE Transactions on Robotics*, 22(3):425–433, June 2006.

[51] Rui Yao, Hui Li, and Xinyu Zhang. A modeling method of the cable driven parallel manipulator for fast. In *Cable-Driven Parallel Robots*, pages 423–436. Springer, 2013.

[52] Marc Gouttefarde, Jean-François Collard, Nicolas Riehl, and Cédric Baradat. Simplified static analysis of large-dimension parallel cable-driven robots. In *2012 IEEE International Conference on Robotics and Automation*, pages 2299–2305. IEEE, 2012.

[53] Tobias Bruckmann, Hannah Mattern, Arnim Spengler, Christopher Reichert, Alexander Malkwitz, and Markus König. Automated construction of masonry buildings using cable-driven parallel robots. In *ISARC. Proceedings of the International Symposium on Automation and Robotics in Construction*, volume 33, page 1. Vilnius Gediminas Technical University, Department of Construction Economics …, 2016.

[54] Yulong Wu, Hung Hon Cheng, Adam Fingrut, Kristof Crolla, Yeung Yam, and Darwin Lau. Cu-brick cable-driven robot for automated construction of complex brick structures: From simulation to hardware realisation. In *2018 IEEE International Conference on Simulation, Modeling, and Programming for Autonomous Robots (SIMPAR)*, pages 166–173. IEEE, 2018.

[55] Lorenzo Gagliardini, Stéphane Caro, Marc Gouttefarde, Philippe Wenger, and Alexis Girin. A reconfigurable cable-driven parallel robot for sandblasting and painting of large structures. In *Cable-Driven Parallel Robots*, pages 275–291. Springer, 2015.

[56] Stefano Masiero, Andrea Celia, Giulio Rosati, and Mario Armani. Robotic-assisted rehabilitation of the upper limb after acute stroke. *Archives of physical medicine and rehabilitation*, 88(2):142–149, 2007.

[57] Jiyeon Kang, Dario Martelli, Vineet Vashista, I Martinez-Hernandez, H Kim, and Sunil K Agrawal. Robot-driven downward pelvic pull to

improve crouch gait in children with cerebral palsy. *Science Robotics*, 2(8):eaan2634, 2017.

[58] Damiano Zanotto, Giulio Rosati, Simone Minto, and Aldo Rossi. Sophia-3: A semiadaptive cable-driven rehabilitation device with a tilting working plane. *IEEE Transactions on Robotics*, 30(4):974–979, 2014.

[59] Hamed Jabbari Asl and Jungwon Yoon. Stable assist-as-needed controller design for a planar cable-driven robotic system. *International Journal of Control, Automation and Systems*, 15(6):2871–2882, oct 2017.

[60] Houssein Lamine, Med Amine Laribi, Sami Bennour, Lotfi Romdhane, and Said Zeghloul. Design study of a cable-based gait training machine. *Journal of Bionic Engineering*, 14(2):232–244, apr 2017.

[61] Frank A Rubino. Gait disorders. *The neurologist*, 8(4):254–262, 2002.

[62] Laurent Blanchet and Jean-Pierre Merlet. Interference detection for cable-driven parallel robots (cdprs). In *2014 IEEE/ASME International Conference on Advanced Intelligent Mechatronics*, pages 1413–1418. IEEE, 2014.

[63] Dinh Quan Nguyen and Marc Gouttefarde. On the improvement of cable collision detection algorithms. In *Cable-Driven Parallel Robots*, pages 29–40. Springer, 2015.

[64] Antoine Martin, Stéphane Caro, and Philippe Cardou. Geometric determination of the cable-cylinder interference regions in the workspace of a cable-driven parallel robot. In *Cable-Driven Parallel Robots*, pages 117–127. Springer, 2018.

[65] M Lesellier and M Gouttefarde. A bounding volume of the cable span for fast collision avoidance verification. In *International Conference on Cable-Driven Parallel Robots*, pages 173–183. Springer, 2019.

[66] Yonatan Wischnitzer, Nir Shvalb, and Moshe Shoham. Wire-driven parallel robot: Permitting collisions between wires. *The International Journal of Robotics Research*, 27(9):1007–1026, 2008.

[67] Martin J-D Otis, Simon Perreault, Thien-Ly Nguyen-Dang, Patrice Lambert, Marc Gouttefarde, Denis Laurendeau, and Clément Gosselin.

Determination and management of cable interferences between two 6-dof foot platforms in a cable-driven locomotion interface. *IEEE Transactions on Systems, Man, and Cybernetics-Part A: Systems and Humans*, 39(3):528–544, 2009.

[68] Lewei Tang, Xiaoqiang Tang, Xiaoling Jiang, and Clément Gosselin. Dynamic trajectory planning study of planar two-dof redundantly actuated cable-suspended parallel robots. *Mechatronics*, 30:187–197, 2015.

[69] Xiaolong Wang and Subhrajit Bhattacharya. A topological approach to workspace and motion planning for a cable-controlled robot in cluttered environments. *IEEE Robotics and Automation Letters*, 3(3):2600–2607, 2018.

[70] Jean-Baptiste Izard, Marc Gouttefarde, Micaël Michelin, Olivier Tempier, and Cedric Baradat. A Reconfigurable Robot for Cable-Driven Parallel Robotic Research and Industrial Scenario Proofing. In Tobias Bruckmann and Andreas Pott, editors, *Cable-Driven Parallel Robots*, volume 12, pages 135–148. Springer Berlin Heidelberg, Berlin, Heidelberg, 2013. Series Title: Mechanisms and Machine Science.

[71] Dinh Quan Nguyen, Marc Gouttefarde, Olivier Company, and Francois Pierrot. On the analysis of large-dimension reconfigurable suspended cable-driven parallel robots. In *2014 IEEE International Conference on Robotics and Automation (ICRA)*, pages 5728–5735, Hong Kong, China, May 2014. IEEE.

[72] Tahir Rasheed, Philip Long, and Stéphane Caro. Wrench-Feasible Workspace of Mobile Cable-Driven Parallel Robots. *Journal of Mechanisms and Robotics*, 12(3), June 2020. Publisher: American Society of Mechanical Engineers Digital Collection.

[73] Arjan J Van Der Schaft and Johannes Maria Schumacher. *An introduction to hybrid dynamical systems*, volume 251. Springer London, 2000.

[74] Bala R Vatti. A generic solution to polygon clipping. *Communications of the ACM*, 35(7):56–63, 1992.

[75] Francisco Martinez, Antonio Jesus Rueda, and Francisco Ramon Feito. A new algorithm for computing boolean operations on polygons. *Computers & Geosciences*, 35(6):1177–1185, 2009.

[76] G Taylor. Point in polygon test. *Survey Review*, 32(254):479–484, 1994.

[77] Tetsuo Asano. An efficient algorithm for finding the visibility polygon for a polygonal region with holes. *IEICE TRANSACTIONS (1976-1990)*, 68(9):557–559, 1985.

[78] Subir Kumar Ghosh. *Visibility algorithms in the plane*. Cambridge university press, 2007.

[79] Pankaj K Agarwal, Eyal Flato, and Dan Halperin. Polygon decomposition for efficient construction of minkowski sums. *Computational Geometry*, 21(1-2):39–61, 2002.

[80] Ron Wein. Exact and efficient construction of planar minkowski sums using the convolution method. In *European symposium on algorithms*, pages 829–840. Springer, 2006.

[81] Edward P Washabaugh, Jane Guo, Chih-Kang Chang, C David Remy, and Chandramouli Krishnan. A portable passive rehabilitation robot for upper-extremity functional resistance training. *IEEE Transactions on Biomedical Engineering*, 66(2):496–508, 2018.

Appendix A

Mathematics Background

A.1 Line Segment-Line Segment Intercept

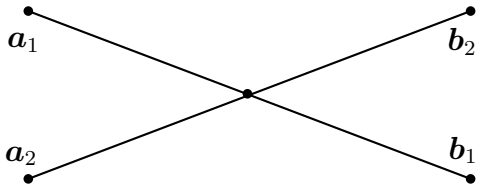

Figure A.1: Line segment-line segment intercept

Consider line segments $\overline{\boldsymbol{a}_1\boldsymbol{b}_1}$ and $\overline{\boldsymbol{a}_2\boldsymbol{b}_2}$, shown in Fig. A.1. A point along each segment can be defined parametrically as

$$\boldsymbol{p}_1 = \boldsymbol{a}_1 + s(\boldsymbol{b}_1 - \boldsymbol{a}_1),$$
$$\boldsymbol{p}_2 = \boldsymbol{a}_2 + u(\boldsymbol{b}_2 - \boldsymbol{a}_2)$$

The point of interception between the two lines can be obtained by equating

$\boldsymbol{p}_1$ and $\boldsymbol{p}_2$ and solving for s:

$$\begin{aligned}
\boldsymbol{a}_1 + s_{\text{int}}(\boldsymbol{b}_1 - \boldsymbol{a}_1) &= \boldsymbol{a}_2 + u_{\text{int}}(\boldsymbol{b}_2 - \boldsymbol{a}_2) \\
(\boldsymbol{a}_1 + s_{\text{int}}(\boldsymbol{b}_1 - \boldsymbol{a}_1)) \times (\boldsymbol{b}_2 - \boldsymbol{a}_2) &= \boldsymbol{a}_2 \times (\boldsymbol{b}_2 - \boldsymbol{a}_2) \\
s_{\text{int}}((\boldsymbol{b}_1 - \boldsymbol{a}_1) \times (\boldsymbol{b}_2 - \boldsymbol{a}_2)) &= (\boldsymbol{a}_2 - \boldsymbol{a}_1) \times (\boldsymbol{b}_2 - \boldsymbol{a}_2) \\
s_{\text{int}} &= \frac{(\boldsymbol{a}_2 - \boldsymbol{a}_1) \times (\boldsymbol{b}_2 - \boldsymbol{a}_2)}{(\boldsymbol{b}_1 - \boldsymbol{a}_1) \times (\boldsymbol{b}_2 - \boldsymbol{a}_2)}
\end{aligned}$$

Following a similar process, one can obtain u_{int} as

$$u_{\text{int}} = \frac{(\boldsymbol{a}_2 - \boldsymbol{a}_1) \times (\boldsymbol{b}_1 - \boldsymbol{a}_1)}{(\boldsymbol{b}_1 - \boldsymbol{a}_1) \times (\boldsymbol{b}_2 - \boldsymbol{a}_2)}$$

If $(\boldsymbol{b}_1 - \boldsymbol{a}_1) \times (\boldsymbol{b}_2 - \boldsymbol{a}_2) \neq 0$, $0 \leq s_{\text{int}} \leq 1$, and $0 \leq u_{\text{int}} \leq 1$, then the two segments intercept at a single point. If $(\boldsymbol{b}_1 - \boldsymbol{a}_1) \times (\boldsymbol{b}_2 - \boldsymbol{a}_2) = 0$ and $(\boldsymbol{a}_2 - \boldsymbol{a}_1) \times (\boldsymbol{b}_2 - \boldsymbol{a}_2) = 0$ then the two segments are colinear and it must be verified that the two segments overlap. If $\min(s_{\boldsymbol{a}_2}, s_{\boldsymbol{b}_2}) \leq 1$ and $\max(s_{\boldsymbol{a}_2}, s_{\boldsymbol{b}_2}) \geq 0$ then there is a nonzero section of overlap between the two co-linear segments. In any other case, the two segments do not intercept.

A.2 Line Segment-Circle Intercept

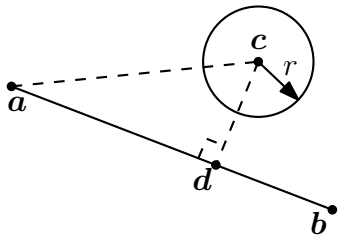

Figure A.2: Line segment-circle intercept

Consider the line segment $\overline{\boldsymbol{ab}}$ and circle $(\boldsymbol{c}, r)$, shown in Fig. A.2. In order to determine if $\overline{\boldsymbol{ab}}$ and the circle intercept, it is first necessary to find the

point on $\overline{\boldsymbol{ab}}$ that is closest to the circle center $\boldsymbol{c}$. The closest point between $\boldsymbol{c}$ and the line defined by $\overline{\boldsymbol{ab}}$ (denoted as $\boldsymbol{d}$) can be determined by projecting segment $\overline{\boldsymbol{ac}}$ onto $\overline{\boldsymbol{ab}}$:

$$s_d = \frac{(\boldsymbol{c} - \boldsymbol{a}) \cdot (\boldsymbol{b} - \boldsymbol{a})}{\|(\boldsymbol{b} - \boldsymbol{a})\|}$$

Point $\boldsymbol{d}$ can then be found by adding an offset of length s_d to the initial point $\boldsymbol{a}$:

$$\boldsymbol{d} = \boldsymbol{a} + s_d \frac{(\boldsymbol{b} - \boldsymbol{a})}{\|(\boldsymbol{b} - \boldsymbol{a})\|}$$

In order to find the closest point to the line segment $\overline{\boldsymbol{ab}}$ from $\boldsymbol{c}$, it must be checked to see if $\boldsymbol{d}$ lies within the segment bounds. If $\boldsymbol{d}$ is outside of segment $\overline{\boldsymbol{ab}}$, then the end point closest to $\boldsymbol{d}$ becomes the point closest to $\boldsymbol{c}$. Thus, the closest point on $\overline{\boldsymbol{ab}}$ to $\boldsymbol{c}$ is obtained as:

$$\boldsymbol{q} = \begin{cases} \boldsymbol{a}, & s_d < 0 \\ \boldsymbol{b}, & s_d > \|(\boldsymbol{b} - \boldsymbol{a})\| \\ \boldsymbol{d}, & \text{otherwise} \end{cases}$$

Iff $\|(\boldsymbol{q} - \boldsymbol{c})\| <= r$, then segment $\overline{\boldsymbol{ab}}$ intercepts circle $(\boldsymbol{c}, r)$.

A.3 Point-Circle Common Tangents

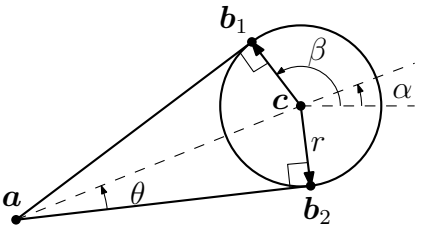

Figure A.3: Point-circle common tangents.

Consider point $\boldsymbol{a}$ and circle $(\boldsymbol{c}, r)$, shown in Fig. A.3. There are always

two possible solutions for a common tangent between point $\boldsymbol{a}$ and circle $(\boldsymbol{c}, r)$. Each tangent can be represented by the line containing point $\boldsymbol{a}$ and a single point on circle $(\boldsymbol{c}, r)$: $\boldsymbol{b}$, as defined in Fig. A.3. The two possible solutions for point $\boldsymbol{b}$ are obtained as

$$\boldsymbol{b}_1 = \boldsymbol{c} + r \begin{bmatrix} \cos(\alpha + \beta) \\ \sin(\alpha + \beta) \end{bmatrix}$$

$$\boldsymbol{b}_2 = \boldsymbol{c} + r \begin{bmatrix} \cos(\alpha - \beta) \\ \sin(\alpha - \beta) \end{bmatrix}$$

where

$$\alpha = \text{atan2}(\boldsymbol{c} - \boldsymbol{a}),$$

$$\beta = \theta + \frac{\pi}{2}\text{rad},$$

and

$$\theta = \sin^{-1}(\frac{r}{\|\boldsymbol{c} - \boldsymbol{a}\|})$$

For a given tangent, the resulting cable wrap direction can be found as

$$\text{dir} = \text{sign}\left((\boldsymbol{b} - \boldsymbol{c}) \times (\boldsymbol{b} - \boldsymbol{a})\right)$$

where a value of 1 corresponds to counter-clockwise wrapping and a value of -1 corresponds to clockwise wrapping.

A.4 Circle-Circle Common Tangents

Consider the two circles $(\boldsymbol{c}_1, r_1)$ and $(\boldsymbol{c}_2, r_2)$ shown in Fig. A.4. There are always four possible solutions for a common tangent between the two circles: two external, and two internal. Each tangent can be represented by a line containing a single point on each circle: $\boldsymbol{a}$ and $\boldsymbol{b}$, as defined in Fig. A.4.

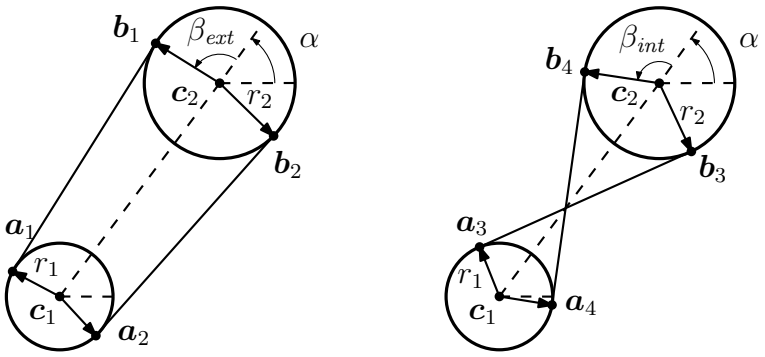

(a) External tangents (b) Internal tangents

Figure A.4: Common tangents between two circles.

Given angle α, calculated as

$$\alpha = \text{atan2}(\boldsymbol{c}_2 - \boldsymbol{c}_1),$$

the two possible solutions for the external common tangents are obtained as

$$\boldsymbol{a} = \boldsymbol{c}_1 + r_1 \begin{bmatrix} \cos(\phi_{\text{ext}}) \\ \sin(\phi_{\text{ext}}) \end{bmatrix}$$

$$\boldsymbol{b} = \boldsymbol{c}_2 + r_2 \begin{bmatrix} \cos(\phi_{\text{ext}}) \\ \sin(\phi_{\text{ext}}) \end{bmatrix}$$

where

$$\phi_{\text{ext}} = \alpha \pm \beta_{\text{ext}}$$

and

$$\beta_{\text{ext}} = \frac{\pi}{2} + \sin^{-1}\left(\frac{r_2 - r_1}{\|\boldsymbol{c}_2 - \boldsymbol{c}_1\|}\right)$$

The two possible solutions for the internal common tangents can be obtained

as

$$\boldsymbol{a} = \boldsymbol{c}_1 + r_1 \begin{bmatrix} \cos(\phi_{\text{int}} + \pi) \\ \sin(\phi_{\text{int}} + \pi) \end{bmatrix}$$
$$\boldsymbol{b} = \boldsymbol{c}_2 + r_2 \begin{bmatrix} \cos(\phi_{\text{int}}) \\ \sin(\phi_{\text{int}}) \end{bmatrix}$$

where

$$\phi_{\text{int}} = \alpha \pm \beta_{\text{int}}$$

and

$$\beta_{\text{int}} = \frac{\pi}{2} + \sin^{-1}\left(\frac{r_2 + r_1}{\|\boldsymbol{c}_2 - \boldsymbol{c}_1\|}\right)$$

For a given tangent, the resulting cable wrap direction about the first circle can be found as

$$\text{dir}_1 = \text{sign}\left((\boldsymbol{c}_1 - \boldsymbol{a}) \times (\boldsymbol{b} - \boldsymbol{a})\right)$$

where a value of 1 corresponds to counter-clockwise wrapping and a value of -1 corresponds to clockwise wrapping. For external tangents, the wrap direction about the second circle $\text{dir}_2 = \text{dir}_1$; for internal tangents, $\text{dir}_2 = -\text{dir}_1$.

Glossary

cable span

The space taken up by a cable over the entire workspace. 4

convex

A set is considered to be convex iff all line segments connecting any two points within the set are also contained within the set. 4

end effector

The end point of a robotic manipulator. Typically the point that is controlled and used for performing tasks. 1

forward kinematics

The process of calculating the end effector pose resulting from a given set of joint configurations. 15

graph

A data structure consisting of a network of nodes (or vertices) connected by edges. Edges can be directed or undirected. 64

installation space

The physical area or volume within which a mechanism is installed. 4

inverse kinematics

The process of calculating the joint configurations required to produce a given end effector pose. 15

linear programming

A standard convex optimization framework consisting of a linear cost function with linear equality and inequality constraints. 12

pose

Combined description of position and orientation for a rigid body. 8

quadratic programming

A standard convex optimization framework consisting of a quadratic cost function with linear equality and inequality constraints. 12

radially convex

A set is considered to be radially convex (or star-shaped) if there exists a point $\boldsymbol{p}$ such that the line segments connecting $\boldsymbol{p}$ to all other points in the set are also contained within the set. 4

tree

A data structure consisting of nodes and edges that visually resembles an upside-down tree. 40

visiblity polygon

Intuitively, it is the set of all points that can be "seen" from a given point. 64

winch

A spool or drum, driven by an electric motor, used for collecting and releasing cable. 1

workspace

The set of end effector poses that can be reached and maintained. May also include additional requirements depending on the specific task needing to be performed. 4

wrench

A combined force and moment vector. The term originates from screw theory and is commonly used in the CDPR literature. 9